Mathematical and numerical analysis of electrospraying electrodynamics

by

Cornelius Louwrens Pieterse

Thesis presented in partial fulfilment of the requirements for the degree of Master in Electronic Engineering in the Faculty of Engineering at Stellenbosch University

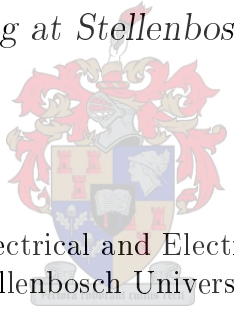

Department of Electrical and Electronic Engineering,
Stellenbosch University,
Private Bag X1, Matieland 7602, South Africa.

Supervisors:

Prof. Willem Jacobus Perold
Electrical and Electronic Engineering
University of Stellenbosch

Prof. Paul Papka
Department of Physics
University of Stellenbosch

December 2014

Declaration

By submitting this thesis electronically, I declare that the entirety of the work contained therein is my own, original work, that I am the sole author thereof (save to the extent explicitly otherwise stated), that reproduction and publication thereof by Stellenbosch University will not infringe any third party rights and that I have not previously in its entirety or in part submitted it for obtaining any qualification.

Abstract

Mathematical and numerical analysis of electrospraying electrodynamics

C.L. Pieterse

Department of Electrical and Electronic Engineering,
Stellenbosch University,
Private Bag X1, Matieland 7602, South Africa.

Thesis: MEng (Electronic)

December 2014

The electrodynamics of arbitrary, point-to-plane electrospraying geometries, were investigated in this research both analytically and numerically. Electrospraying is the process during which particles of sizes in the nanometre range are simultaneously generated and charged by means of an applied electrostatic field. A high electrostatic potential is applied to a conductive capillary needle, which overcomes the force exerted by the liquid surface tension. One of the primary limitations of this process are corona discharges. The effect of corona discharges have not been studied quantitatively, even though it is frequently reported in the electrospraying literature.

The main objective of this research was to understand the corona discharge thresholds associated with electrospraying. Previously, only one theoretical, and two empirical investigations studied this phenomenon, over a time period of approximately forty years. It was clear that by better understanding these thresholds, electrospraying could be applied much more effectively.

A corona discharge threshold model is proposed, using either a numerical or analytical model for the calculation of polarization fields. When compared with the experimental results of other researchers, both these two models have average relative percentage errors of approximately 15%. These are the first models proposed in the literature for the calculation of electrospraying corona thresholds. A new method to determine surface tension using electrospraying is described theoretically. In addition to this method, the calculation of corona discharge thresholds have various applications. For example, the dynamics of electrostatic ion thrusters are much better described, powder production by means of electrospraying can be optimised, and pattern generation using pulsed electrospraying cone-jets can be optimised as well.

Uittreksel

Wiskundige en numeriese analiese van elektrosproei elektrodinamika

("Mathematical and numerical analysis of electrospraying electrodynamics")

C.L. Pieterse

Departement Elektriese en Elektroniese Ingenieurswese,
Universiteit van Stellenbosch,
Privaatsak X1, Matieland 7602, Suid-Afrika.

Tesis: MIng (Elektronies)

Desember 2014

Die elektrodinamika van arbitrêre, punt-tot-vlak elektrosproei geometrieë was beide analities en numeries ondersoek in hierdie tesis. Dit is die proses waartydens nanodeeltjies gelyktydig gegenereer en elektrostaties gelaai word. Deur 'n hoë elektriese potensiaal aan te lê tot 'n geleidende kapillêr, is dit moontlik om die krag van die oppervlakte spanning te oorkom. Een van die primêre beperkings van elektrosproei is corona ontladings. Die effek van corona ontladings was nog nie kwantitatief bestudeer nie, selfs al word dit dikwels rapporteer in die elektrosproei literatuur. Die primêre doel van hierdie navorsing was om die corona ontlading drempels te verstaan wat geassosieer word met elektrosproei. In die verlede was daar nog net een teoretiese, en twee empiriese ondersoeke gewees wat hierdie verskynsel bestuur het, oor 'n tydperk van ongeveer veertig jaar. Dit was duidelik dat deur 'n beter begrip te hê van hierdie elektrosproei drempels, kan hierdie proses baie meer doeltreffend toegepas word.

In hierdie tesis word 'n corona ontlading drempel model voorgestel, wat gebruik maak van 'n analitiese of numeriese model om die polarisasie velde te bereken. Wanneer vergelyk met die resultate van ander navorsers, het beide die modelle 'n gemiddelde relatiewe persentasie fout van ongeveer 15%. Hierdie is die eerste modelle wat voorgestel word vir die berekening van corona ontlading drempels. Deur gebruik te maak van elektrosproei, word 'n nuwe metode ook voorgestel om die oppervlakte spanning te bereken. In byvoeging tot hierdie, het die berekening van corona ontlading drempels vele ander toepassings. As 'n voorbeeld, die dinamika van elektrostatiese ioon stuwers word beter beskryf, en poeier produksie deur middel van elektrosproei kan optimeer word.

Acknowledgements

I would like to express my greatest gratitude to the following people:

My supervisors deserve recognition for their endless support and guidance. I am infinitely indebted to Prof. Paul Papka for years of stimulating discussions, mentorship, and support in my research endeavors. I am further very grateful to Prof. Willie Perold for allowing me to research this given topic.

I am also very grateful to Dr. J.N. Kriel (Department of Physics), Prof. H. Wiegel (Department of Physics), Prof. G.J.F. Smit (Department of Applied Mathematics), and Dr. L. Conradie (iThemba LABS) for fruitful discussions. I need to specifically thank Dr. C.M. Steenkamp (Department of Physics) for always assisting me when I needed assistance, whether it was to improve the structure of presentations, or when I needed advice regarding non-linear optics. I will be forever grateful to these people, as they played a key role in developing my research skills and approach strategies to scientific problems. I also need to thank Prof. T.E. Cloete (Vice-Rector of Research and Innovation) for always supporting and believing in me. Similarly, I need to thank Ms. Anita Nel and her team at InnovUS. From being a freshman, they supported me, and further eliminated a large deal of stress from my life by managing and protecting the intellectual property of my research.

A special thank you must be given to Prof. Heinrich Schwoerer. He allowed me to finalise this thesis while working in his ultrafast laser physics laboratory. His understanding and guidance proved invaluable, both in scientific research and mentorship. I will be forever grateful to him for his wise input.

The most important acknowledgement should go to my parents, Marianna and Lourie Pieterse. They always supported me in my research endeavors from a young age. Even though I grew up on a sheep farm in the desert (technically the Karoo), they have *always* made it possible for me to pursue my dreams. Such selflessness is infinitely appreciated. Similarly, I need to specially thank my friends, which I am not going to list, as I will write many paragraphs about how wonderful each of them are. Family and friends are indeed priceless!

Just as importantly, Maximillian Kaizen. Not only was she one of my best friends, but without her vision, support, motivation and general philosophical discussions, this thesis would have not been in the shape it is currently. This intrinsic friendship of ours extended even beyond this, with her insights and wonderful ideas shaping an integral part of my mind, and method of reasoning. To say I am thankful and appreciate it, would be an understatement.

Dedications

Quantitatively, this is only one flexible sheet of fibres pressed together.
Qualitatively, it represents an infinite amount of gratefulness and appreciation.

This thesis is dedicated to my parents, Marianna and Lourie Pieterse.

Contents

Nomenclature

Constants

$\varepsilon_0 = 8.854\,187\,817 \times 10^{-12}$ F/m

Parameters

V	Applied potential	[V]
R	Capillary-tip radius	[m]
K	Electrical conductivity	[S/m]
ρ	Fluid mass density	[kg/m^3]
a, b	Hyperbolic coefficients	[1]
S_1	Liquid-droplet length	[m]
S_2	Liquid-droplet surface area	[m^2]
S_3	Liquid-droplet volume	[m^3]
ϵ	Relative permittivity	[1]
L	Separation distance	[m]
α	Separation-radius ratio	[1]
γ	Surface tension	[N/m]
Q	Volumetric flow rate	[m^3/s]

Variables

E	Electric field	[V/m]

Subscripts

tip	Capillary tip
C	Corona threshold
τ	Mason
M	Maximum
P	Polarization

Chapter 1 | Introduction

> *At the atomic level, we have new kinds of forces and new kinds of possibilities, new kinds of effects. The problems of manufacture and reproduction of materials will be quite different. I am, as I said, inspired by the biological phenomena in which chemical forces are used in repetitious fashion to produce all kinds of weird effects.*
>
> – Richard Feynman, *There's Plenty of Room at the Bottom* [1].

The above quote by Richard Feynman is absolutely beautiful and something worth pursuing. It was, and very still is, my castle in the air that the research presented in this thesis, will suggest new kinds of possibilities and or effects.

1.1 Background and motivation

Electrospraying (technically electrohydrodynamic atomization) is the process during which particles of sizes in the nanometre range are simultaneously generated and charged by means of an applied electrostatic field. For this process, a high electrostatic potential is applied to a conductive capillary needle, which overcomes the force exerted by the liquid surface tension. Therefore, a slightly conductive liquid can be channelled through a capillary, and when reaching the particular threshold electric field that is required to overcome the surface tension, the rounded tip of the meniscus deforms and expends a jet of particles, which is referred to as an electrospraying cone-jet.

Applications of electrospraying include thin-film depositioning, ultra-fine particle production, electroencapsulating and biotechnology. These processes can be carried out in an ambient atmosphere, without the use of any complex reactors and vacuum chambers, being the case for conventional methods. From literature it is also reported that electrospraying does not significantly alter the physical and or chemical properties of the liquids being sprayed.

One of the primary limitations of this process is corona discharges. The effect of corona discharges have not been studied quantitatively, even though it is frequently reported in literature. The effects thereof on the spray current and spraying modes have not been considered previously, being the motivation of this thesis. Understanding the corona discharges associated with electrospraying, the application of this process could be optimised.

1.2 Objectives and contributions

The primary objective of this research was to understand the corona discharge thresholds associated with electrospraying. Previously, only one theoretical, and two empirical investigations studied this phenomenon, over a time period of approximately forty years. It was clear that by better understanding these thresholds, electrospraying could be applied much more effectively, as corona discharges are considered to be one of its biggest limitations.

Using elementary electrostatic theory, the electrostatics of the electric fields generated by point-to-plane electrospraying geometries were described. The analytical models obtained are simple and agree very well with finite element analysis results, which were obtained with a COMSOL Multiphysics package. These numerical results were further used to derive a polarization model for such geometries. This numerically obtained model also compares very well with the analytically derived models. Dimensional analysis was employed to qualitatively motivate the assumptions made when deriving the analytical model. These dimensional analysis results agreed with those made by Mason and his experimental observations.

A corona discharge threshold field model was proposed, using either the numerically or the analytically derived models for the calculation of polarization fields. When compared with the experimental results of other researchers, both these two models have average relative percentage errors of approximately 15% (assuming the experimental measurements to be correct). These were the first models proposed in the literature for the calculation of electrospraying corona thresholds. A new method to determine surface tension using electrospraying is described theoretically. Unlike most other methods which are restricted to certain liquids, it is possible to use this proposed method with most liquids. The unique feature of this method is its ability to do measurements at arbitrary temperatures. In addition to this new method of measuring surface tension, the calculation of corona discharge thresholds have various applications. For example, the dynamics of electrostatic ion thrusters are much better described, powder production by means of electrospraying can be optimised, and pattern generation using pulsed electrospraying cone-jets can be optimised.[1]

[1] These applications are protected by three provisional patent submissions. For detailed information regarding these, the intellectual property office of the university (InnovUS), can be contacted on `ajnel@sun.ac.za` or `info@sun.ac.za`.

Chapter 2 | Literature review

Nanotechnology is an idea that most people simply didn't believe.
– Ralph Merkle.

This chapter describes the current literature on electrospraying theory and how it is applicable to both basic scientific research and used in industry. Given that electrospraying is fundamental in the field of mass spectrometry, there is a very large amount of literature available on the subject. Conveniently, this chapter is limited to the fundamental and well-established concepts thereof, followed by background to the problem currently being researched. In the last section, an introduction is given to gaseous electronics, more specifically on corona discharges, in order to motivate the research approach of this thesis.

2.1 Electrospraying

This section is based primarily on a group of review articles that focused on the fundamental physics describing electrospraying [2–4], but also how these phenomena can be applied in different industrial situations [5–7]. Looking at the applications of electrospraying (see Figure 2.1 for images of the process), it is possible to understand the limitations thereof and motivate this thesis.

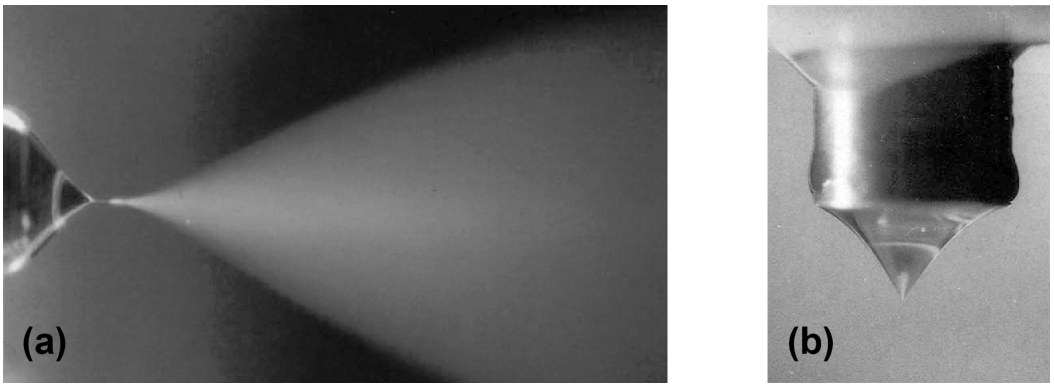

Figure 2.1: The cone-jet spraying mode is shown in (*a*), with the Delft Aerosol Generator shown in frame (*b*). Reprinted with permission from Elsevier [8, 9].

2.1.1 Fundamental electrospraying theory

Electrospraying (technically called electrohydrodynamic atomization) is a process during which particles of sizes in the nanometre range are simultaneously generated and charged by means of an applied electric field. For this process, a high electrostatic potential is applied to a conductive capillary needle, which overcomes the force exerted by the liquid surface tension. Any slightly conductive liquid can therefore be channelled through a capillary, and when reaching the particular threshold electric field that is required to overcome the surface tension, the rounded tip of the meniscus deforms and expends a jet of particles, which is referred to as an electrospraying cone-jet [2].

For this reason, no additional mechanical energy other than the electric field is required to generate these particles, which makes electrospraying a simple physical concept. As this jet travels away from the cone-jet, sometimes being called the Taylor-cone, it becomes unstable and disintegrates into a plume of highly charged droplets, such as shown in Figures 2.1 and 2.2. These droplets generated can have charge magnitudes close to half the Rayleigh limit [4], which is the magnitude of charge required to overcome the surface tension force and promote droplet fission. The droplet charge and diameter can be controlled by adjusting the applied potential and volumetric flow. Electrospraying is used for fine particle production, because when the liquid of the droplet evaporates, any powder suspended in it forms a solid particle cluster [7].

For a review of the electrospraying process, consult papers of Cloupeau and Prunet-Foch [2], Smith [10], Jaworek and Krupa [11]. Smith experimentally determined the range of liquid parameters which determines the atomizability thereof, with his main result being a limit of 50 mN/m for surface tension.

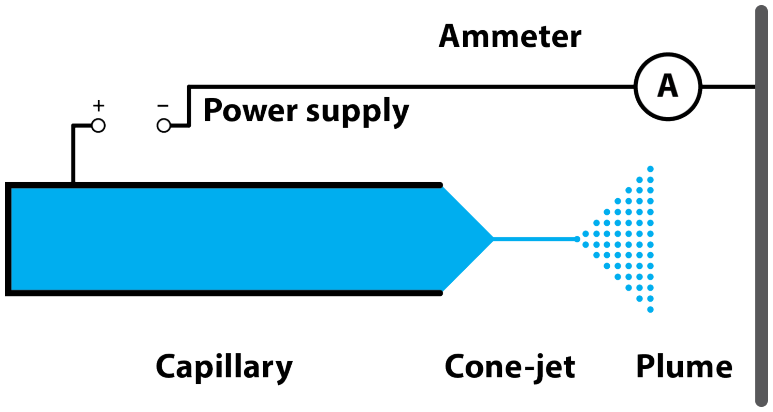

Figure 2.2: The schematic of a simple experimental electrospraying configuration. Applying a high electrostatic potential to a capillary filled with a slightly conductive liquid, the electric field at the tip opening overcomes the liquid surface tension force. The rounded tip of the liquid deforms and expends a jet of particles (called cone-jet), which becomes unstable and disintegrates into a plume of charged droplets.

Previously, it was mentioned that after the liquid-tip deforms this leads to spraying from a cone-jet (the most desired and well-described spraying mode). For this cone-jet mode, the liquid meniscus assumes the structure of a regular, axisymmetric cone together with a narrow jet at the apex thereof, stretching along the axis of the capillary. There are, however, other modes as well, each of which being different in the meniscus formation and the jet that emerges from it. These different type of modes are affected by the physical properties of the liquid, but also by the experimental parameters, such as the volumetric flow rate and applied potential. The different modes are also not predictable from the properties and or parameters, with only a few scaling laws known for the cone-jets. For a thorough review of these modes, see [2].

Determining the size of the generated droplets theoretically is a challenging task, but many authors published results on this topic in the past few decades. One of these theoretical results is that of de la Mora and Loscertales [12],

$$D(R) = \lambda(\epsilon)\left(\frac{Q(R)\epsilon_0\epsilon}{K}\right)^{1/3}, \tag{2.1.1}$$

where $\lambda(\epsilon)$ is a constant depending on the relative permittivity ϵ. For all of the proposed theoretical equations, the droplet diameter scales with the volumetric flow rate $Q(R)$, while being inversely proportional to electrical conductivity K. These theoretical models agree with experimental results and are widely used in the literature. The critical potential V_{ct} and electric field E_{ct} that are required to be applied, which initiates the liquid surface instability, are [13, 14]

$$V_{ct} = \sqrt{\frac{\gamma R}{\varepsilon_0}}\ln\left(\frac{4L}{R}\right) \quad \text{and} \tag{2.1.2}$$

$$E_{ct} = 2\sqrt{\frac{\gamma}{\varepsilon_0 R}}. \tag{2.1.3}$$

After the cone-jet formed, an ion current is detectable (assuming zero current contribution due to corona discharges or ion emissions), from charged particles being collected on the counter-electrode [12–15]. This current is given by

$$I = \frac{f(\varepsilon)}{\sqrt{\varepsilon}}\sqrt{\gamma K Q}, \tag{2.1.4}$$

where the empirical function $f(\varepsilon) = \varepsilon/2$ is defined for $\varepsilon < 40$, and constant $f(\varepsilon) = 20$ for when $\varepsilon \geq 40$ [12, 15]. From this equation, the principle role of the flow rate is clear, because since the system current can be measured, it is possible to quantise the performance and production rate of such processes.

As noted by Smith already in 1986, although there is considerable interest in electrospraying, the steady-state cone-jet mode has not been satisfactorily described, especially not the basic mechanisms thereof [10]. The conductivity is one of the most important parameters, but as it has been shown previously in (2.1.2) and (2.1.3), it does not affect the threshold fields. For a review of the purely ionic regime, which is important for propulsion systems, see [16, 17].

2.1.2 Electrospraying applications

Using a single capillary is not practical in industry, because it is a low-volume throughput process and finds it difficult to compete with conventional methods of particle production. The use of an array of capillaries solves this hurdle [18]. Electrospraying offers multiple advantages over conventional spraying systems, which are based on charging by means of induction [7]:

1. Electrospray generated droplets are smaller in size (< 1 μm diameter).
2. Droplet size distribution is usually narrow (small standard deviation).
3. There are no droplet agglomeration or coagulation, as the droplets are self-dispersed into space from the cone-jet.
4. Electric fields can be used to easily deflect or focus the droplets.
5. High degree of droplet charging suggests a high depositioning efficiency.

One successful application of electropsraying is the nebulisation technique for use as drug atomization. For nebulisers it is important to be capable of creating monodispersible particles of a specific diameter range, without changing the chemical and physical properties of the drug itself. Zimlich *et al.* developed a prototype nebuliser based on the principles of electrospraying, generating particles with diameters between 1 and 6 μm [19]. Clinical tests using this device showed that 78% of the particles were deposited in the respiratory tract, which is approximately four times greater than that obtained using conventional methods. This method also showed to be depositing the drugs more uniformly within the lungs. For the majority of the other research conducted, it was, however, required to produce the particles in an artificial CO_2, N_2 or SF_6 atmosphere in order to avoid electrical discharges [20–22].

A new research topic is the use of electrospraying as a direct writing tool, which are capable of producing structures of widths of less than 50 μm, which is achievable by dispersing metal powders in a solution [23]. For conventional ink-jet printing, the generated drops are approximately twice the size of the nozzle, compared to drops being an order of magnitude smaller than the nozzle for electrospraying. This enables the use of larger nozzles, which are less prone to clogging and offer longer lifetimes. This will be particularly useful for printing electrically conducting ink, not only because the electrospraying is cheaper and more adaptable, but in current methods the unwanted ink are being dissolved from the depositioning surface.

Other applications of electrospraying include thin-film depositioning, fine particle production, electroencapsulating and biotechnology. These processes can be carried out in an ambient atmosphere, without the use of any complex reactors and vacuum chambers, being the case for conventional methods. From literature it is also reported that electrospraying does not significantly alter the physical and or chemical properties of the liquids being sprayed [6].

2.1.3 Electrospray corona discharges

The effect of electrical discharges, especially corona discharges, have not been studied quantitatively, although reported frequently in the literature [9, 10, 24–31]. The effects thereof on the spray current and spraying modes have not been considered often, and is therefore the research motivator of this thesis.

The work of Smith focussed on characterising the electrospraying process in terms of the fluid system and properties, with particular interest in liquid conductivities at approximately zero hydrostatic pressure [10]. When studying the effect of surface tension, Smith noted that it is not possible to electrospray liquids having surface tensions higher than approximately 50 mN/m in air. The conclusion was that, as previously reported by Buraev and Vereshchagin [24], the corona threshold of air was reached before obtaining the minimum electric field required for electrospraying [32]. From this he then argued that the threshold field for even low surface tension liquids are above that of the corona threshold of air ($\sim 3\times10^6$ V/m) and suggested this to be a discrepancy.

Joffre and Cloupeau studied the charge emission due to corona discharges both theoretically and experimentally [25]. Their model agrees with their experimental results, being based on conical profiles similar to those employed in this research. It is also noted by them that the corona threshold fields are difficult to determine for these kinds of geometries and uses the general law of Peek, as described in the next section on gaseous electronics [33].

Similar to the research of Smith, Hayati *et al.* studied various liquid parameters, but primarily focussed on liquid conductivities [26]. When considering corona discharges, their main conclusions are that the droplet profile does not change for using artificial atmospheres and that liquid conductivities do influence discharges. They suggest that the highly conductive liquids, such as water and glycerol, allow discharges to occur from the liquid surface, but that for low conductivity liquids, discharges occur from the capillary tip.

Recently, in 1997 [28], Jaworek and Krupa published research specifically on electrospraying corona discharges. Their conclusions are that the corona onset threshold is lower for a water filled capillary than for a similar dry capillary, although the current-voltage characteristics of both cases are similar. They emphasise that the mechanisms of discharge are different for the two situations. Similarly to Hayati *et al.*, they noted that for water the discharge occurs at the surface of the liquid, and not from the capillary tip.

Park *et al.* focussed on the effects of introducing a capillary guard plate, but also mentions the effects of corona discharges [29]. They suggest the use of a model introduced by Rousse to calculate the corona thresholds [34], and then to use an external electric field controller to limit the field to these thresholds. This same model is introduced in the next section on gaseous electronics. Various authors solved this problem by increasing the air pressure, or by using gasses such as CO_2, N_2 or SF_6, which have higher corona thresholds than air.

Already in 1972, Buraev and Vereshchagin published fundamental research on those effects of electrospraying high surface tension liquids and the associated corona discharges [24]. It seems, however, that this work went unnoticed by other authors, mainly when looking at the low number of citations and lack of references to some of the analytical concepts introduced by them.

The objective of their work was to clarify how corona discharges interfere with electrospraying of liquids with sufficient conductivity. They approached this problem by describing the liquid droplet at the capillary tip with a semiellipsoid of revolution. Then, by defining the electrospray geometry to be that of a conducting ellipsoid at the surface of a parallel plate capacitor, they derived an analytical expression for the electric field at the tip of the semiellipsoid, to be used for calculating these thresholds using known literature [35].

Using this model, they showed that for any given capillary tip radius, the primary parameter determining whether a liquid can be electrosprayed is the surface tension. Knowing the corona thresholds analytically, it is then possible to calculate the maximum surface tensions of liquids to be electrosprayed. For their experimental geometry ($R = 450$ μm and $L = 39$ mm) the maximum surface tension was calculated to be 49 mN/m, which ended up being quoted in subsequent papers to be the maximum for all geometries [10].

Their results showed that it is possible to accurately describe the geometry using the revolving ellipsoid model when compared with experimental results. However, the applied potential at which the cone-jet mode is reached and two of the three ellipsoidal parameters are required to be known. Having all of this information, it is now possible to calculate the corona thresholds for each of the liquids. This method produces invaluable results, but it is cumbersome, as it is required to know the geometrical shape of the liquid droplet from observation at the threshold field required for initiating the cone-jet mode.

Only again in 1994, the next quantitative study on corona discharges was published by Cloupeau [27]. The most crucial fact he noted was that the corona onset thresholds are gap distance dependent, which are inversely proportional to the separation distance, not being constant as previously assumed by Smith. Cloupeau also importantly pointed out, Peek's law is defined for relatively large diameter wires, and that more recent laws of Rousse [34] should rather be used. Having the same argument as Buraev and Vereshchagin, he argued that when the critical threshold field for liquids are below that of the corona threshold, they should be electrosprayable. He further experimentally verified these laws to radii as small as $R = 2.5$ μm for thin wires. Another important point he made was that even the corona thresholds for cylinders and wires are debated, meaning that for electrospraying geometries exact results cannot be expected. This is an indicator of the complexity involved with corona discharges. Lòpez-Herrera *et al.* applied this suggested approach of calculating corona thresholds for the electrospraying of water in air at atmospheric pressure [36]. Hoburg and Melcher applied a similar approach in 1975 already when studying the corona discharges developing from water droplets on electrical lines [37].

There is also the scenario of Borra *et al.* (2004) who purposefully induced corona discharges when electrospraying water [30]. Their objective was to study the influence of corona discharges on the cone-jet mode, and then to stabilise it with a continuous corona glow-discharge in order to generate unimodal sized water droplets. Similar to the other researchers, they noted that the discharges develop from the liquid surfaces, and also from the capillary tips for increased potentials. This was attributed to increased conductivities, causing an increase in outward electrostatic pressures, resulting in an increased inward capillary pressure to balance the force. The cone volume reduces due to this process, thus enabling discharges to develop from the capillary tip (shown in Figure 2.3). For similar research in a CO_2 environment, see [38].

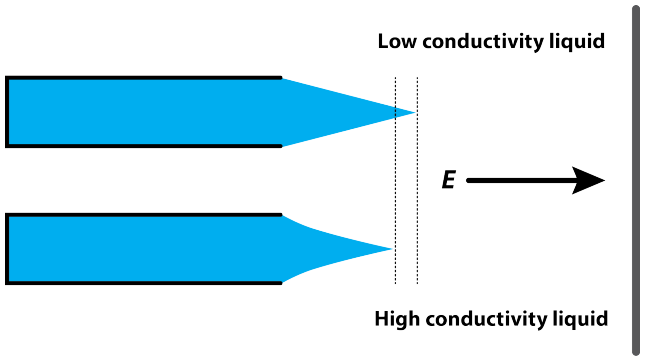

Figure 2.3: A schematic of the effect of conductivity on the electrospraying process. Increased conductivities cause an increase in the outward electrostatic pressures, thus resulting in an increased inward capillary pressure to balance this force. The cone volume reduces due to these processes. Diagram based on the argument of Borra *et al.* for the corona stabilised glow-discharge electrospraying of water [30].

Jaworek *et al.* noted in the most recent study (2005) on corona discharges that this phenomenon was still not studied sufficiently, and that it is generally not considered in electrospraying models found in literature [31]. In this paper, they presented results on the emission spectra of electrical discharges observed while electrospraying, concluding that both the emission lines of the gaseous environment and the elements present in the liquid are identifiable. Previously, similar work was done by Meesters *et al.* in 1991, although they argued that only the molecular emission lines of N_2 are detectable [39].

Apart from Buraev and Vereshchagin [24], only Borra *et al.* [40] published quantitative results on electrospraying corona discharges. The main objective of this research was to study various liquids at atmospheric conditions under the influence of corona discharges. A capillary-to-plane geometry was used, which is similar to that of the point-to-plane geometries defined in corona discharge literature [41, Chapter 4]. Borra *et al.* [40] defined the electric dripping mode, which is an electrospraying mode characterised by discharges. Also, it was found that smaller capillary radii enables more stable electrospraying.

2.2 Gaseous electronics

The review presented in this chapter is solely based on the text of the same title by Hirsh and Oskam [41, Chapter 4]. As corona discharges are not quantitatively investigated, this review will be the only description thereof.

The corona discharge, which is considered to be a glow discharge in terms of its physical mechanisms, is the ensemble of discharges that occur due to divergent electric fields of a high intensity. Electric fields of such characteristics are generated by conductors of small radii of curvature, such as along high-voltage electrical transmission lines and material irregularities on flat surfaces. These discharges are self-sustained, which means that no external ionization source is required for them to be initiated. For a detailed review of the development of the understanding of such discharges, see the text by Loeb [42]. The large amount of present research in the field of corona discharges is a manifestation of the complexity involved in these phenomena [43].

The threshold voltages (where the discharge initiates) of corona discharges are characterised by a current increase between these electrodes from about 0.01 fA to 1 μA, together with the appearance of a faint glow at the stressed electrode (smallest radius of curvature electrode) [44]. The background current is due to natural ionization processes, due to, for example, cosmic rays and ionizing radiation from naturally occurring radioactive decays.

2.2.1 Threshold criteria

An electron avalanche is required to initiate a corona discharge, for which the electron can arise from the cathode, or should be detached from an anion when such electrons and positive ions are not initially present. This is the reason for different discharge mechanisms, depending on the polarity of the stressed electrode. These avalanches develop in the regions where the electric field is the most intense, which is at the point of the smallest radius of curvature for inhomogeneous fields. The ratio of the field at the stressed E_r and unstressed E_R electrodes, E_r/E_R, should be of adequate intensity for such a process to be initiated. The magnitude of this required ratio is geometry and stressed electrode polarity dependant. Given that for electrospraying the stressed electrode is mostly of positive polarity, except however when considering the purely ionic regime, only the scenario of positive stressed electrodes will be considered here (especially since the physical mechanics describing negative coronas are much less thoroughly understood). For a review of the purely ionic regime, which is important for propulsion and lithographic applications, see [16, 17].

Positive corona avalanches develop toward the anode, initiating in a region between the electrodes which are dependant on the initial seed electrons. According to the Raether criterion, on the order of $\sim 5 \times 10^8$ avalanche electrons are required to reach the critical point where the avalanche-to-streamer transi-

tion occurs [45]. Peek calculated the threshold electric field required for such a transition, for the case of a coaxial cylindrical geometry at an inner electrode,

$$E_{rs} = E_0 m\delta(1 + k/\sqrt{\delta r}), \tag{2.2.1}$$

where E_{rs} is in terms of kV/cm, $E_0 = 31$ kV/cm for air, m is the empirical constant describing the surface of the conductor ($0.6 < m < 1$, with $m = 1$ representing a perfectly smooth surface), $\delta = 0.932p/(273 + T)$ ($\delta = 1$ for STP conditions, p being the pressure, and T in Kelvin), $k = 0.308$ cm$^{1/2}$ is another empirical constant, and r being the radius of the conductor [33]. This law in its general form has been shown to be valid for other gasses, and from pressures in the range of a few millibars to several atmospheres, for conductor radii between 100 μm to several centimetres, and both direct and alternating applied potentials.

Gary *et al.* showed semi-analytically that the Peek expression is obtained for electrodes of a single curvature, such as coaxial cylinders and parallel wires, and for electrodes of a double curvature, such as for example the point-to-plane and concentric sphere geometries. Their result only differed from the original Peek's law by a factor of 1/2 to the radius of the conductor [46], e.g.

$$E_{rs} = E_0(1 + k/\sqrt{r/2}). \tag{2.2.2}$$

They showed experimentally that this equation applies to both stressed anodes and cathodes, with the critical electric fields being almost identical for the different polarities. It is also possible to rewrite these equations in terms of the corresponding threshold voltage, when expressing the electric field in terms of this potential V along an axis in the separation gap d. For the paraboloidal point-to-plane geometry, this electric field is given along the x-axis by

$$E_x = \frac{2V}{(r + 2x)\log\left((r + 2d)/r\right)} \simeq \frac{2V}{(r + 2x)\log\left(4d/r\right)}. \tag{2.2.3}$$

Llewellyn-Jones and Williams showed that the effect of pressure has variations on these threshold electric fields and voltages as described by Paschen-type curves, when they studied a coaxial wire-cylindrical geometry [47]. Cloupeau proposed an adaption of Peek's law for micron distances (formulated by Rousse), to be used for electrospraying geometries [27, 34]:

$$E_{rs} = 30 + 9R^{-0.5} \qquad R \geq 100\ \mu\text{m} \tag{2.2.4}$$

$$= 62.7 + 1.74R^{-0.75} \qquad 15\ \mu\text{m} < R < 100\ \mu\text{m} \tag{2.2.5}$$

where R is the radius of curvature in centimetres. Similarly to the equation by Peek, this equation return results in a kV/cm unit. It was verified by Cloupeau that these equations hold for the defined, and radii as small as 2.5 μm [27].

2.2.2 Transient coronas

The finite amount of time between the potential application to the electrodes, and the initiation of corona discharges is called the time lag, generally being on the order of several microseconds. When working sufficiently below this corona threshold for a given geometry, the complete knowledge of these times is not of such importance. As for all discharges, the corona discharge is unstable at its threshold [48], which are due to two reasons. Firstly, the electron avalanches generated during the auto-stabilization stage of the discharge, are statistical phenomena, and not all of them lead to full streamers. Further, the ionization coefficients vary exponentially with the applied electric field, suggesting that they are sensitive to small fluctuations. However, adding a large resistor to the circuit, it is possible to stabilise the discharge to a certain degree, with further stabilization possible with the addition of an external parallel capacitor (see Figure 2.4 for an example). The behaviour of corona discharges are different for alternating potentials, as the conditions will be different for the ions in the gap for each of their half-cycles. As the current research is about preventing coronas, even when using alternating voltages, this topic is not discussed here.

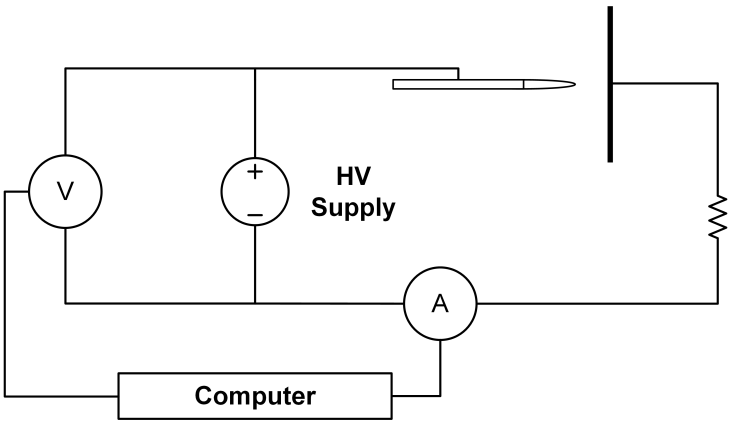

Figure 2.4: An experimental electrospraying configuration circuit. A series resistor acts as a ballast to stabilise the spraying process, which also decreases the likelihood of corona discharges. This circuit will be discussed in detail in Section 3.5, where it is being used to measure the surface tension of liquids using electrospraying.

2.3 Chapter summary

In addition to containing the fundamental descriptions of electrospraying, this chapter is a summary of the literature on how discharges affect electrospraying. The motivation is to formulate analytical theories to describe this phenomena. From the research of Buraev and Vereshchagin, it was observed that the electric fields at which corona discharges occur for electrospraying, is not constant for all liquids. For this reason, the effect of polarization was researched.

Chapter 3 | Theoretical work

> *For the success of any physical investigation depends on the judicious selection of what is observed as of primary importance, combined with a voluntary abstraction of the mind from those features which, however attractive they may appear, we are not sufficiently advanced in science to investigate with profit.*
>
> – James Clerk Maxwell

This chapter describes the theoretical background and models used throughout this thesis. The first section gives a formal and thorough description of the electrical and associated polarization fields, explaining what quantities need to be calculated numerically and how these theoretical results can supplement those results. The second last section explains the Taylor-cone formation time theory and how it can be described analytically. In the final section, the other subsections are combined to propose a new method of determining the surface tension of general liquids using the models derived in this research. The effect of polarization on electrospraying geometries will be one of the primary themes investigated. From literature review, it is known this affects corona discharges.

3.1 Electrostatic theory

The electric fields generated amid electrospraying are of a divergent nature and is described by needle-to-point, sometimes called point-to-plane, geometries. Figure 3.1 indicates the nature of these fields when solving them numerically. Previously, such geometries have been studied intensively to understand the breakdown of dielectrics (such as polythene and polyisobutylene) by internal discharges, with J.H. Mason being a pioneer in the field [49–51].

The electrostatics theory used for this thesis is therefore largely based on the research of Mason, with this section primarily using the results published in his 1955 manuscript on the breakdown of dielectrics in divergent fields [51]. These results from his research will be summarised in the next section. These results are well established and frequently used by the electrostatics community [52–54], but they do not include the effects of polarization due to the liquid at the capillary-tip. The section hereafter introduces the fundamental concepts of dielectric theory and derives results relevant to the current research.

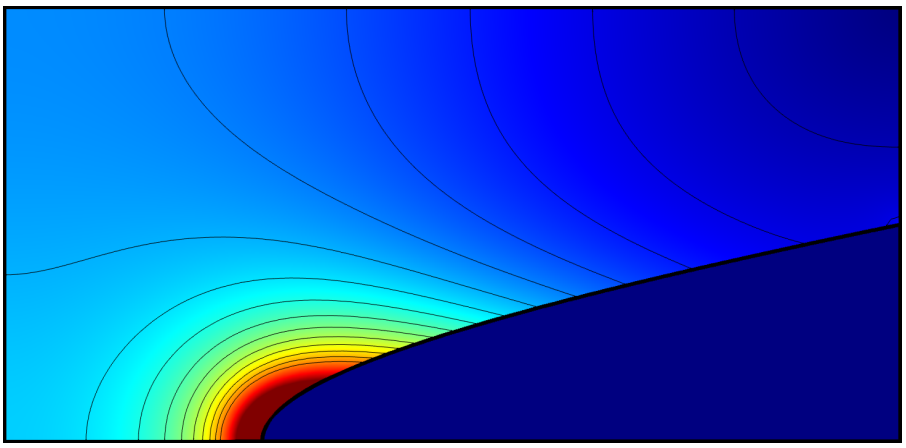

Figure 3.1: A numerical solution of the electric field for a needle-to-plane geometry. The contours are of equal change in field magnitude, with the maximum strength of the field being limited for visual purposes, hence the uniform red surface at the tip. This figure was generated using COMSOL Multiphysics for a radius and separation distances of 100 and 1000 μm respectively.

The capillaries used for electrospraying are mostly of a design such as shown in Figure 3.2, especially when smaller needle tips (≤ 20 μm) are required. Even for geometries as these, the Mason formulation can still be used, as it is defined for long needles in terms of the tip radius of curvature. A comparison of these two geometries is given in Figure 3.3 when solved numerically, where the field at the capillary tip of Figure 3.2, is compared to that of the Mason equation.

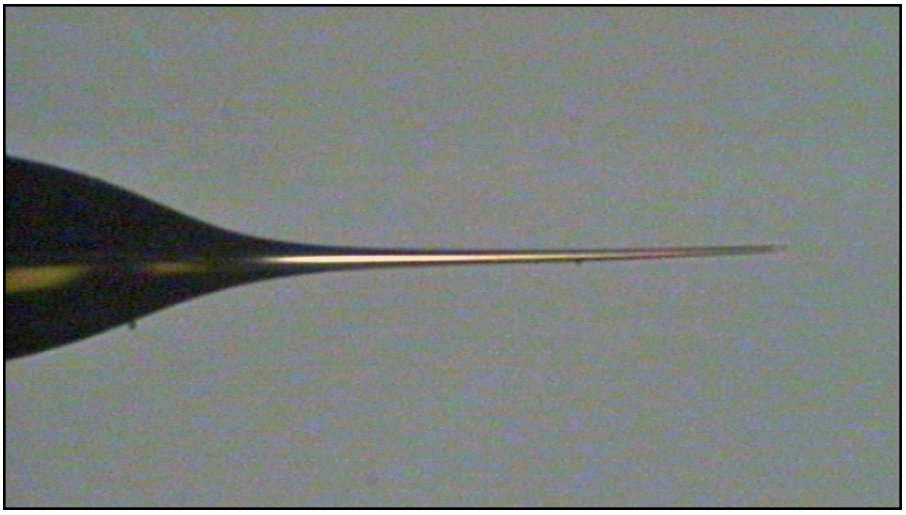

Figure 3.2: A photograph of a needle design frequently used for electrospraying. This specific needle was manufactured by Waters, with a capillary tip radius of 5 μm, being made from borosilicate glass coated with gold [55]. Note the dust particles.

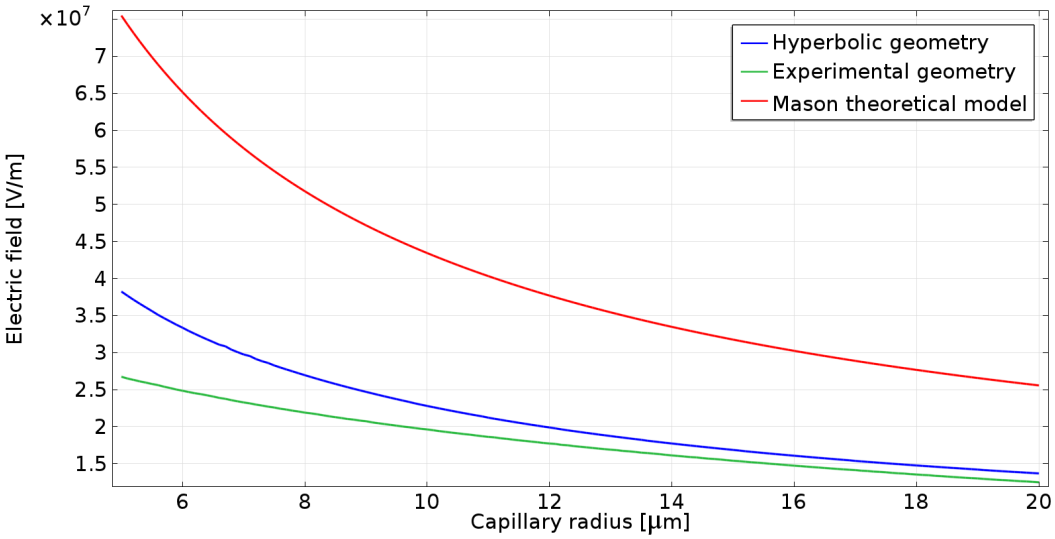

Figure 3.3: A comparison of the numerical electric fields for an experimental setup, such as in Figure 3.2, the hyperbolic geometry used during the majority of simulations, and the Mason field as described by (3.1.4). The parameters used were an applied voltage of 1000 V, with a separation distance of 500 μm relative to the tip.

3.1.1 Mason electrostatic theory

Mason assumed that the capillaries can be treated as conductive hyperboloids, which enabled the calculation of the electric field at the tip thereof as [51]

$$\frac{Z^2}{c_2^2\xi_0^2} - \frac{\rho^2}{c_2^2(1-\xi_0^2)} = 1, \tag{3.1.1}$$

where Z, ρ, c and ξ are the hyperboloid coordinates. Applying a potential V_0 to this hyperboloid when separated a distance t from the counter-electrode, as indicated in Figure 3.4, the electric field on the Z-axis is given by [49]

$$E = 2V_0/c_2(1-\xi)^2\log(1+\xi_0)/(1-\xi_0). \tag{3.1.2}$$

The radius of curvatures at the tip is given by $R = t(1-\xi_0^2)/\xi_0^2$, which enables the calculation of the electric field at this capillary tip as

$$E_{max} = \frac{2V_0 p_1}{\log(q)}, \tag{3.1.3}$$

where $p_1 = R^{-1}\sqrt{R/t+1}$ and $q = R^{-1}\left(2t+R+2\sqrt{t(t+R)}\right)$. Further, for large separation-radius ratios $t > 10R$, the electric fields at this tip-point are approximated (known as the Mason equation in literature) to be [51]

$$E_{max} \simeq \frac{2V_0}{R\log(1+4t/R)} \simeq \frac{2V_0}{R\log(4t/R)}. \tag{3.1.4}$$

For an additional method to calculate these electric fields at the capillary tip, that is independent of the counter-electrode separation distance t, see the original text. Mason, however, argued that as these methods give similar results, it is easier to make use of (3.1.4) than this more complicated method. The experimental results from his work are summarised for the scenarios of breakdown tests in the dielectrics polyisobutylene and polythene [51]:

1. For all geometrical configurations, the AC corona initiation field strength is lower than that of a DC electric field for the same geometry.
2. The average electric field, also sometimes called the effective electric field $E_{av} = V_0/t$, is not affected by the radius of curvature.
3. Breakdown only occurs when the electric field at the needle tip exceeds that of the dielectric field strength of the given material.
4. The average effective electric and dielectric field strengths have similar temperature dependencies, being indirectly proportional to temperature.
5. The average electric field decreases with larger separation distances.
6. At room temperature, the breakdown threshold is approximately 25% higher when applying a negative voltage to the needle.

This subsection described the electrostatics of electrospraying geometries as formulated by Mason. This theory, however, does not account for polarization. The next subsection will introduce the fundamental concepts of polarization, where after derivations are done which are relevant to the geometry of interest.

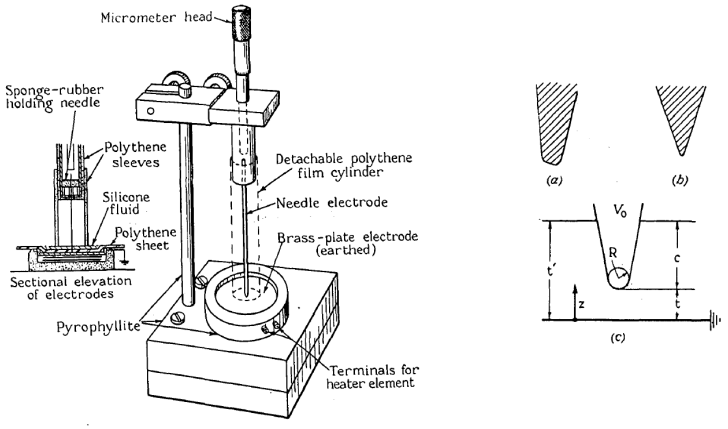

Figure 3.4: The experimental setup as employed by Mason (left) and the geometry used for the theoretical derivations (right), as it appeared in the original publication. Nickel-plated-steel needles with tip radii of between 2 and 32 μm were investigated. For most tests, tips had radii of 2 or 5 μm. Reprinted with IEEE permission [51].

3.1.2 Electrostatic dielectric theory

This subsection introduces the fundamental concepts of electrostatic dielectric theory, based on the texts of Purcell[56, Chapter 10] and Kittel[57, Chapter 16] for the case of homogeneous electric fields. In the sections following, theories are derived to describe the given inhomogeneous problem at hand.

The most basic capacitor consists of two parallel conductor plates, each of area A, separated by a distance S, such as shown in Figure 3.5. Any capacitor is described by its capacitance $C_0 = Q/V = A\epsilon_0/S$, which is a relation of the charge Q on each of these plates to the potential difference V between them.

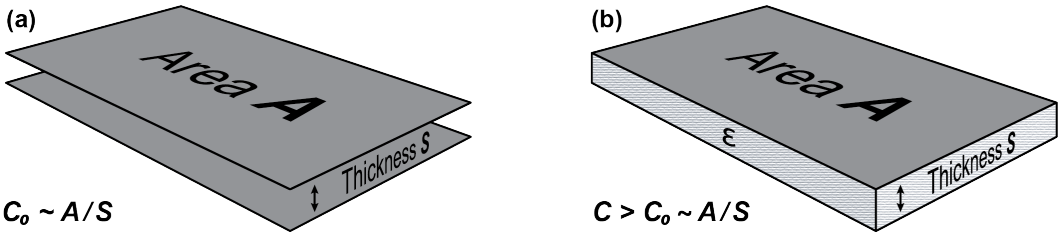

Figure 3.5: Vacuum capacitor, frame (a), compared to a capacitor using a dielectric with dielectric constant $\epsilon = Q/Q_0$ (frame b), which relates the increase in the amount of charge stored on the plates compared to the vacuum capacitor. The capacitance of such capacitors will always be greater than that of an equivalent vacuum capacitor.

Capacitors employing vacuum as a separation medium are used in electrical circuits where extremely high and rapidly changing potentials are involved, but it is generally much more favourable to include an insulator, or rather called a dielectric, between the plates. For such a configuration, the capacitance C will be higher than that of a vacuum capacitor, suggesting more charge being present on each of the plates for the same geometry and potential difference. As the dielectric consists of molecules, the electric field due to the charges on the plates, acts on these molecules. The effect within the material is that the negative and positive charge distributions as a whole are slightly displaced relative to each other. The material as a whole remains neutral, but layers of charge are induced at the surfaces, such as shown in Figure 3.6.

Due to these induced layers of charge on the dielectric surfaces, the charge on the capacitor plates also increases until the total charge at both ends equals that of an equivalent vacuum capacitor. This additional charge is supplied by the voltage source V, and this same amount of charge will pass through the resistor R on closing the circuit switch. Doing so, and therefore removing the electric field between the plates, these induced charges will be evacuated and the molecules rearrange themselves. The factor describing this additional capacitance is called the dielectric constant $\epsilon = Q/Q_0$.

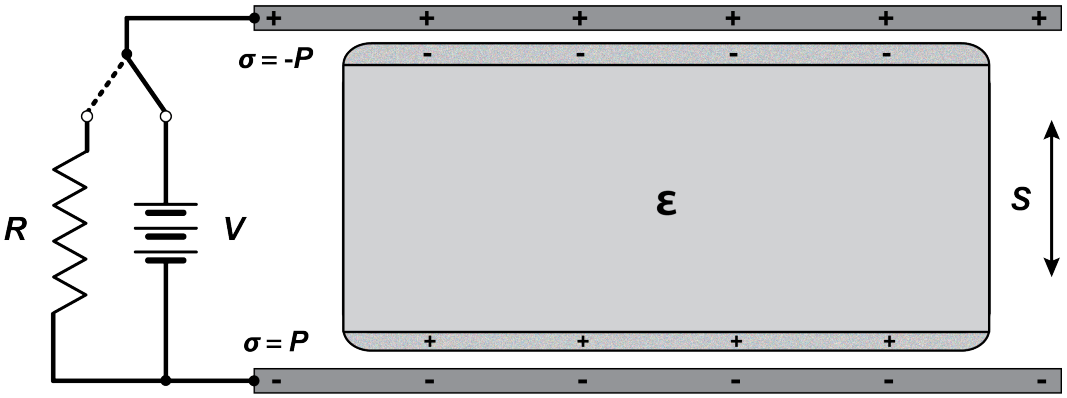

Figure 3.6: This diagram explains qualitatively what happens on the macroscopic scale when placing a dielectric in a uniform electric field E, created by two parallel conducting plates. Note the accumulation of charge on the dielectric surfaces.

To understand these concepts properly, as it was explained for the macroscopic dielectric in Figure 3.6, it is required to investigate them microscopically. When picturing the hydrogen atom according to the Bohr model, this system has a dipole moment $\mathbf{p}$ at all time instances, because this vector $\mathbf{p}$ constantly changes as the electron orbits the proton. From modern quantum mechanics it is known that this is not true, as even although the time averaged dipole moment is zero, radiation is expected due to the fast changing electric fields. In order to understand dielectrics better, it is better suited to treat this problem quantum mechanically, by assuming the system to be in its lowest energy state of a characteristic charge distribution. This approach allows an electric field to be regarded as a stationary charge distribution from the electron, combined with that of the protons in the nucleus. It is also possible to extend this picture to all other atoms and even molecules.

The dipole moment of such stationary configurations are always zero, as it will be for any atom or molecule in their lowest energy states. These electron distributions always have spherical symmetries, independent of the number of electrons present. As soon as this hydrogen atom is placed in an external electric field, the situation changes, as this field alters the charge distribution in such a manner that the electric dipole moment thereof is not zero any more. The question now remains how much such an external field distorts this atom. Purcell[56, Chapter 10] relates the amount of relative charge displacement Δz, which induces this dipole moment $\mathbf{p}$, as

$$\mathbf{p} = e\Delta z \approx a^3\mathbf{E} = \alpha\mathbf{E}, \tag{3.1.5}$$

where e is the electronic charge, a the atomic dimension, and $\mathbf{E}$ the external electric field. The dipole moment vector will be in the direction of the applied electric field, with the factor α being called the atomic polarizability.

It is also of interest to describe the electric field induced by molecules which have dipole moments due to this externally applied field. The nature of these molecules is not important, all that is currently required, is that there is a macroscopic number of N molecules, each of which have dipole moment $\mathbf{p}$, which are fully described. The total dipole strength per unit volume is $\mathbf{p}N\,dv$, which can be treated as a single dipole of equivalent strength, when being an observer a large distance away. The quantity $\mathbf{P} = \mathbf{p}N$ is called the density of polarization, with dimensions of charge per volume, and is frequently used to describe dielectrics. As previously, it is assumed that the material consists of neutral molecules, with only the dipole moments contributing to the field.

Using these concepts, it can be shown that the electric potential outside of a uniformly polarized dielectric, is equivalent to that of two surfaces with a charge density $\sigma = \mathbf{P} \cdot \hat{\mathbf{n}} = P\cos\theta$ at the surfaces thereof. See Figure 3.6 for example, being the case of a slab in a uniform field $\theta = 0$. It is important to define the boundary of this surface, such that the near fields of the individual molecules do not contribute to an electric field measurable here. Generally, a distance of between 1 and 2 nm will be sufficient for this to be true. Further, it can be shown that the average field within the dielectric, which is caused by all of the charges within this volume V, is given by [56, Chapter 10]

$$\langle \mathbf{E} \rangle = \frac{1}{V} \int_V \mathbf{E}\, dv = \frac{\mathbf{P}}{\epsilon_0}. \tag{3.1.6}$$

All of the concepts presented so far assumed that the external electric field is uniform, which is key to making the calculations of quantities such as the macroscopic internal field and the polarization density analytically possible. To show the flexibility of these relations, the effect of placing a dielectric sphere into a uniform field is analysed. A similar procedure will later be extended to the scenario of the electrospraying problem at hand.

Firstly, assume a uniform electric field $\mathbf{E_0}$ to be generated by two parallel conducting plates. The dielectric sphere is to be inserted into this field, with the requirement that it is placed far from the plates, and therefore not affecting the original field. At a large distance away from the sphere, the original field $\mathbf{E_0}$ will appear unaltered, being the definition of a uniform electric field. Inside the sphere, the effective field $\mathbf{E}$ is due to both the original field $\mathbf{E_0}$, and also the field $\mathbf{E_1}$ generated by the polarized material itself

$$\mathbf{E} = \mathbf{E_0} + \mathbf{E_1}, \tag{3.1.7}$$

with $\mathbf{E_1}$ being determined by the polarization density $\mathbf{P}$, which itself depends on the total effective field inside the dielectric, and given by

$$\mathbf{P} = \epsilon_0 \chi \mathbf{E} = \epsilon_0 \left(\epsilon - 1\right) \mathbf{E}. \tag{3.1.8}$$

In (3.1.8) the relative susceptibility $\chi = \epsilon - 1$ was introduced. The field $\mathbf{E_1}$ due to the uniformly applied field is sometimes also called the depolarization field, which are given for a general ellipsoid of revolution by [57, Chapter 16]

$$\mathbf{E_1} = -\frac{N_p \mathbf{P}}{\epsilon_0} \quad \Rightarrow \quad \mathbf{E_1} = -\frac{\mathbf{P}}{3\epsilon_0} \quad \text{(sphere)}, \tag{3.1.9}$$

where N_p is the depolarization factor for any given ellipsoid. For the case of a sphere $N_p = 1/3$, also see the work of Osborn for a general solution [58]. After substitution and trivial algebraic manipulations, it can be shown that, for the dielectric sphere in a uniform electric field,

$$\mathbf{P} = 3\epsilon_0 \left(\frac{\epsilon - 1}{\epsilon + 2}\right) \mathbf{E_0} \quad \Rightarrow \quad \mathbf{E} = \left(\frac{3}{\epsilon + 2}\right) \mathbf{E_0}. \tag{3.1.10}$$

The electric potential with potential field lines, and electric field magnitude arrows are given in Figure 3.7. The general solution of the polarization density and effective electric field in terms of the depolarization factor is given by

$$\mathbf{P} = \left(\frac{\chi \epsilon_0}{1 + N_p \chi}\right) \mathbf{E_0} \quad \Rightarrow \quad \mathbf{E} = \left(\frac{1}{1 + N_p \chi}\right) \mathbf{E_0}. \tag{3.1.11}$$

Using these equations to calculate the fields within the dielectric, the fields outside can be calculated using the dielectric boundary conditions [59]:

$$(\mathbf{E_{above}} - \mathbf{E_{below}}) \cdot \hat{\mathbf{n}} = \frac{\sigma}{\epsilon_0} \quad \text{and} \quad (\mathbf{E_{above}} - \mathbf{E_{below}}) \times \hat{\mathbf{n}} = 0. \tag{3.1.12}$$

Note however, ellipsoids are unique in having a constant depolarization field inside their boundaries, when placed in a uniform external field. Other bodies do not have this property, even inside uniform fields. In the next subsection, hyperbolic bodies are studied, due to their relevance to electrospraying.

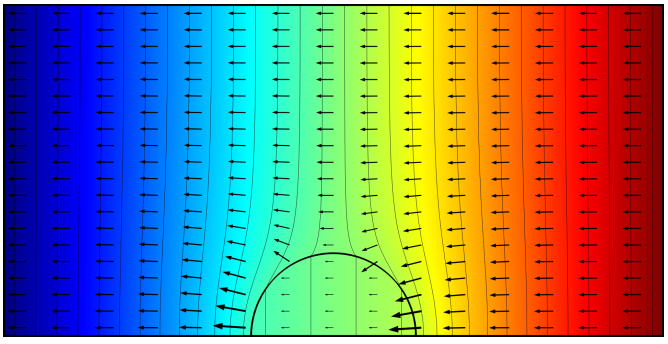

Figure 3.7: A numerical solution of the electric potential for a sphere in a uniform electric field, with the potential field lines and electric field magnitude arrows. This figure was obtained using finite element analysis with COMSOL Multiphysics [60].

3.1.3 Liquid droplet description

As explained in the numerical chapter, the capillaries used for electrospraying is described mathematically using a high eccentricity revolving hyperbola. For that reason, it is modelled using a hyperbola with parameterisation t as

$$x(t) = a\cosh(t) \quad \text{and} \quad y(t) = b\sinh(t), \tag{3.1.13}$$

where a, b are the hyperbolic coefficients. Equation (3.1.13) therefore produces the right branch of a parametric hyperbola, with the semi-major axis a parallel to the x-axis, and the semi-minor axis b parallel to the y-axis. The hyperbolic eccentricity e is then defined as $e = \sqrt{1 + b^2/a^2}$ (satisfying $e > 1$). To include the liquid, a second hyperbola with scaling factors $C_x = 1.025$ and $C_y = 1.75$ was introduced, resulting in

$$x_l(t) = aC_x\cosh(t) \quad \text{and} \quad y_l(t) = bC_y\sinh(t). \tag{3.1.14}$$

The values of the scaling factors were arbitrarily chosen, the only goal being to make the tip comparable to a liquid droplet. This combination of hyperbolas was also implemented numerically, being another advantage for using this given approach. See Figure 3.8 given below for an example of such a geometry. It is important to note that for this modification, the radius of curvature of the bottom hyperboloid should be employed, as that is the needle that generates the field being experienced by the liquid volume, inducing polarization.

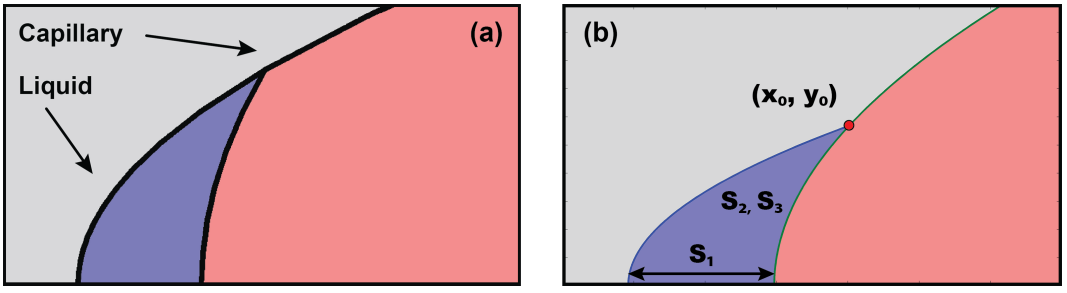

Figure 3.8: The geometry used numerically to introduce the dielectric liquid (blue surface) was accomplished using a second revolving hyperbola, with the scaling factors $C_x = 1.025$ and $C_y = 1.75$ to produce frame (a). This was achieved by deleting the additional area, such as shown in frame (b), and then revolving this secondary hyperbola. Further note, the radius of curvature of the bottom hyperboloid is being employed, as that is the needle that generates the electric field being experienced by the liquid. Also, by knowing this interception point (x_0, y_0), the liquid volume can be calculated. See Figure 3.9 for volume versus radius curves using different hyperbolic coefficients. The parameters S_1, S_2, S_3 refers to the liquid droplet length, surface area, and volume respectively. These parameters are employed in section 4.2 for the purpose of doing dimensional analysis on the numerical results.

The volume of the droplet is calculated for the parameter value t_0 for which the two curves intersect. Knowing this value, a solid of revolution integration can be done on the liquid curve, being bounded from zero to this intersection point. To find this intersection point, each of the curves (3.1.13) and (3.1.14) are converted to single equations and equated, giving

$$x_0 = \frac{aC_x\sqrt{C_y^2 - 1}}{\sqrt{C_y^2 - C_x^2}}. \tag{3.1.15}$$

Solving (3.1.13) for the parametric variable and substituting the above

$$t_0 = \operatorname{arcosh}(x_0/a) = \operatorname{arcosh}\left(\frac{C_x\sqrt{C_y^2 - 1}}{\sqrt{C_y^2 - C_x^2}}\right). \tag{3.1.16}$$

Using these bounds, the volume of the liquid can be calculated using

$$V = \pi \int_0^{t_0} y^2 \frac{dx}{dt}\, dt \tag{3.1.17}$$

$$= \pi ab^2 \int_0^{t_0} \sinh^3(t)\, dt \tag{3.1.18}$$

$$= \frac{4\pi ab^2}{3}\left[\sinh^4(t_0/2)\,(2 + \cosh(t_0))\right]. \tag{3.1.19}$$

Being able to calculate the liquid volume using a closed-form expression enables the calculation of the amount of molecules per droplet, which can be used at a later stage to calculate the approximate polarization density. Equation (3.1.19) was compared with the results obtained of doing numerical volume integration.

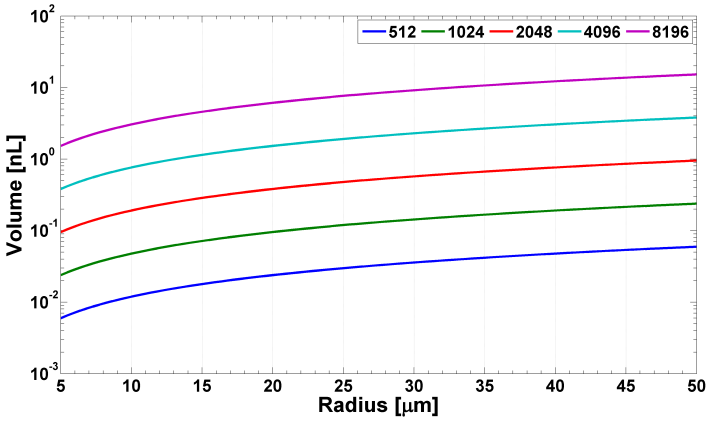

Figure 3.9: Liquid volume versus capillary radius curves when plotting (3.1.19) for different parametric a-coefficients. As previously, the scaling factors $C_x = 1.025$ and $C_y = 1.75$ were used to produce these curves.

3.2 Conformal mappings

Frequently a complex number $z = x+iy$ is visualised as a vector in the complex plane, used for example as a phasor to describe Kirchhoff's circuit laws. Using this concept, the complex function $w = f(z)$ is defined as the mapping of a point in the complex domain (z-plane), to the related complex w-plane point. For that reason, these complex functions $w = f(z) = u(x, y) + iv(x, y)$ can be considered as planar transformations, with w as the image of z under f:

$$u = u(x, y) \quad \text{and} \quad v = v(x, y). \tag{3.2.1}$$

Mappings of such nature are called conformal, requiring the transformation to be analytic and the first derivative thereof non-zero at the points of interest, and for the angle between any two intersecting curves to be preserved. See Figure 3.10 for an example of such a transformation.

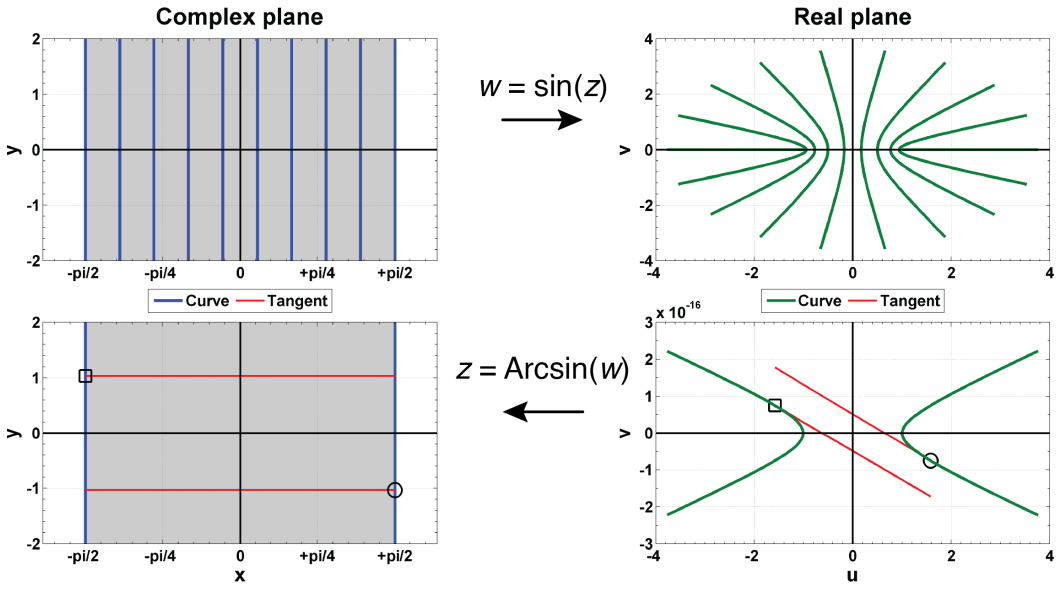

Figure 3.10: The top row shows how it is possible to transform from vertical lines in the complex plane to hyperbolas in the real plane. Similarly, in the bottom row it is shown how the inverse transformation reproduces the original configuration. The red tangent lines indicate the angle preservation at two arbitrary points.

Such a mapping of interest is given by $f(z) = \sin(z)$, with $-\pi/2 \leq x \leq \pi/2$ being the fundamental region of the sine function. Vertical lines $x = \alpha$ within this region are described by $z(t) = \alpha + it, -\infty < t < \infty$, leading to

$$\frac{u^2}{\sin^2(\alpha)} - \frac{v^2}{\cos^2(\alpha)} = 1, \tag{3.2.2}$$

with the image of such a line being a hyperbola with $\pm\sin(\alpha)$ as the u-intersect. Given $f'(z) = \cos(z)$, this mapping is conformal at all points except $z = \pm\pi/2$.

Any bounded harmonic function $u = u(x, y)$ which is defined on the entire boundary of a region R, is a solution to a Dirichlet problem of the same region. Given both real and imaginary parts of any analytical function are harmonic, a Dirichlet problem of region R is solvable by solving it in a simpler region R'. This is achieved by transforming the original problem from the region R to R' using a conformal mapping defined for that geometry. The key steps for this procedure (see Figure 3.11 for details) are given [61, Chapter 20.2]:

First Find a conformal mapping that transforms the original region R to R'.

Second Transfer the boundary conditions of R to the boundaries of R' and solve the problem in this new region, obtaining a solution U.

Third The solution to the original problem is $u(x, y) = U(f(z))$.

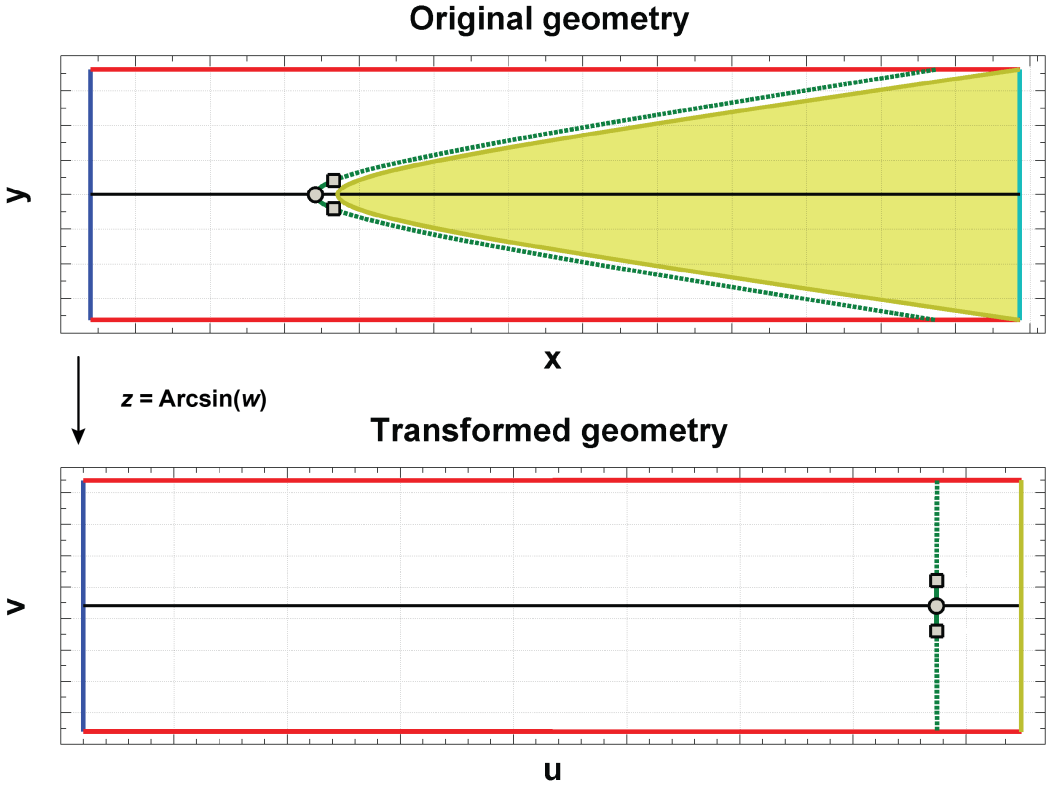

Figure 3.11: The transformation from a hyperbolic to a simplified linear geometry. When solving the problem, the boundary conditions should be transferred as shown. Note, the two dimensional capillary (yellow surface) is being reduced to a line, laying on the original back boundary (vertical turquoise line). The partial parabola (green line) is used to describe the liquid, with the parameters thereof being defined solely within the transformed geometry. See Section 3.3 for details regarding this definition.

3.2.1 Domain uniformisation

From Section 3.1.2 it is given that it is possible to calculate the electric fields at the dielectric boundary analytically when the external field is uniform. Note, for the geometries used during electrospraying, these fields are not uniform. By transforming the current hyperbolic geometry to a linear geometry, it should be possible to obtain a uniform external electric field, enabling the calculation of an analytical solution. An analytically favourable transformation is that of $w = z^2$, being defined for $z \neq 0$ conformally. Complex vertical lines $x = \alpha$ are described by $z(t) = \alpha + it, -\infty < t < \infty$, giving

$$v = \pm 2\alpha\sqrt{\alpha^2 - u}. \tag{3.2.3}$$

Note, only these vertical z-plane lines are considered, as they produce positive radii transformed curves. The image of such a line is a parabolic-like curve with $\pm\alpha^2$ as the u-intersect, thus requiring $u \leq \pm\alpha^2$ to constrain real values. Calculating the tip ($v = 0$) radius of curvature R, the above equation can be rewritten by substituting $\alpha = \sqrt{R/2}$ to introduce the radius

$$v = \pm 2\sqrt{\frac{R}{2}\left(\frac{R}{2} - u\right)}. \tag{3.2.4}$$

Using this definition, it is thus possible to map these parabolic curves into straight lines (such as shown in Figure 3.12). This uniformisation is achieved by mapping each curve in the original electrospraying geometry to the transformed geometry. The parabolic curves are mapped into lines, while linear curves are also mapped into lines. This is ideal for analytical derivations, as the geometry is reduced to a two dimensional problem (although not a hyperbolic geometry).

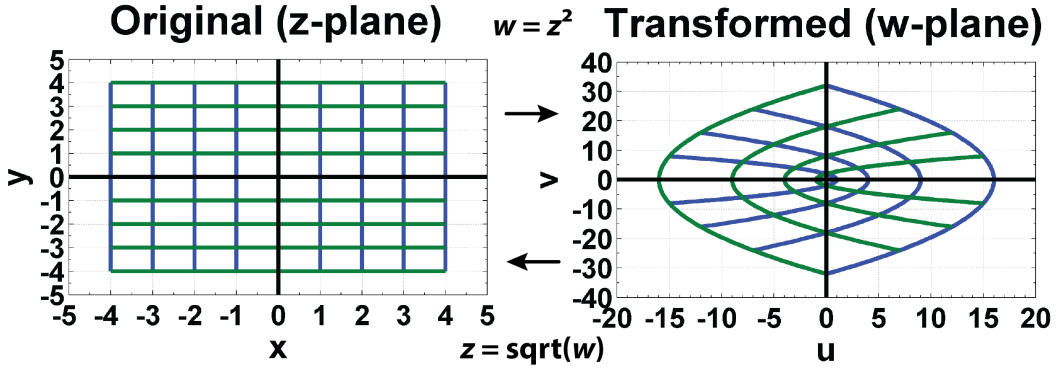

Figure 3.12: The transformation from the original parabolic to a linear geometry. This mapping is the inverse of $f(z)$, therefore being $w = \sqrt{z} = \sqrt{\alpha + it}$. Note, only these vertical z-plane lines are considered, as they produce positive radii curves.

These mappings are impaired, as they do not always transform into uniform domains. To visualise the effect of translating a point in the original geometry on the transformed geometry, see Figure 3.13 for the current mapping. This figure indicates the change in point position in the transformed geometry, by translating it only horizontally or vertically in the original geometry, and also along the line $v = u$, to show the different effects that appear depending on the nature of translation. These transformed curves qualitatively explain why changing the length of a vertical plane in the original geometry also results in it then being translated horizontally. The reason why there is this interest in understanding these dependencies will become clear soon. Previously, it was mentioned that a uniform domain is desired. However, when transforming the original geometry, it results in a skewed geometry, as shown in Figure 3.14(a). In order to obtain a uniform domain, the length h of the bottom and grounded planes in the original geometry, are increased until the grounded plane has the same transformed length H_y as the capillary h_0 (see Figure 3.14(b)).

However, it was earlier showed with a point in Figure 3.13 that this also results in a horizontal translation. To correct this problem, the following steps were followed (see Figures 3.14 and 3.15 for the individual visual steps):

1. The bottom and grounded planes length h, planes perpendicular to the capillary, is increased such that the transformed plane length H_y will be the same as for a uniform geometry. This suggests that the plane length H_y, is equal to that of the transformed capillary length h_0, thus $H_y = h_0$.

2. This approach though introduces side-bands observed in the transformed geometry, which themselves cause non-uniformities. By removing these bands and translating the grounded plane to H_x, where it would have been without this length controlled bottom plane h, a uniform geometry is obtained. See Figure 3.15(b) for these side-bands (dashed red curves).

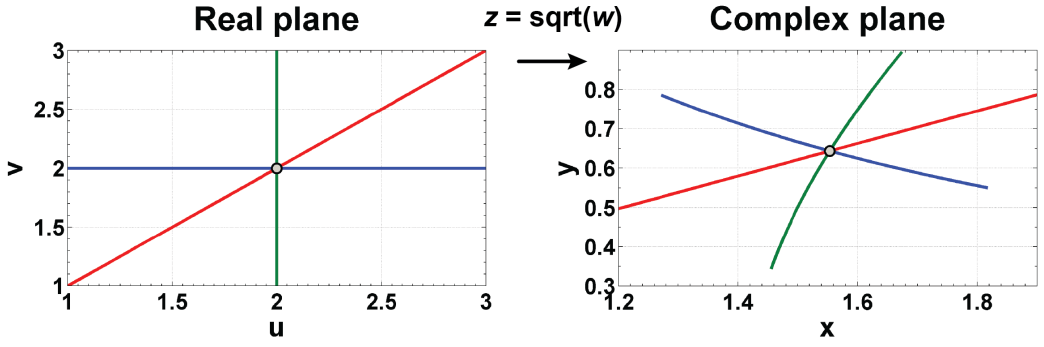

Figure 3.13: The change in the position of a point in the transformed geometry by translating it only horizontally or vertically in the original geometry, and also along the line $v = u$, shows the different effects that appear, depending on the translation.

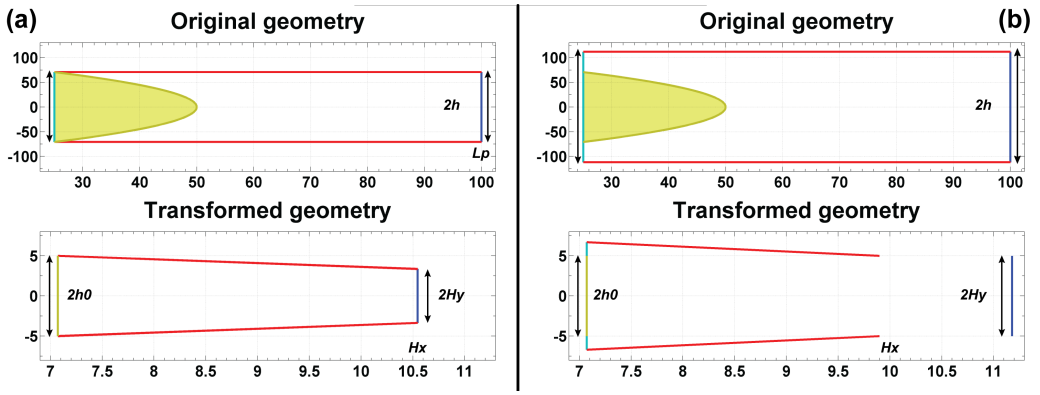

Figure 3.14: The transformation $w = \sqrt{z}$ from a parabolic-like to a simplified linear geometry, dissected into the individual steps. When transforming this geometry, the boundary conditions are also transferred as shown. Frame (a) shows the original and transformed geometries, from which it is noted that the lengths of the transformed backplane h_0 and the grounded-plane H_y differ. By changing the backplane length h in the original geometry, it is possible to set these two lengths equal, such as shown in frame (b). The source codes of these transformations are given in the Appendix A.2. See Figure 3.15 for the additional steps necessary to obtain a uniform geometry.

A partial parabola is employed to describe the liquid (also see Section 3.1.3 for the description of how this was obtained for hyperbolic curves), with these parameters being defined solely within the transformed geometry. The liquid boundary is shown in Figure 3.15(d), in the original geometry, but the details of how it was obtain is not of importance. This liquid boundary is defined in the transformed geometry, as it is analytically solvable in such a configuration.

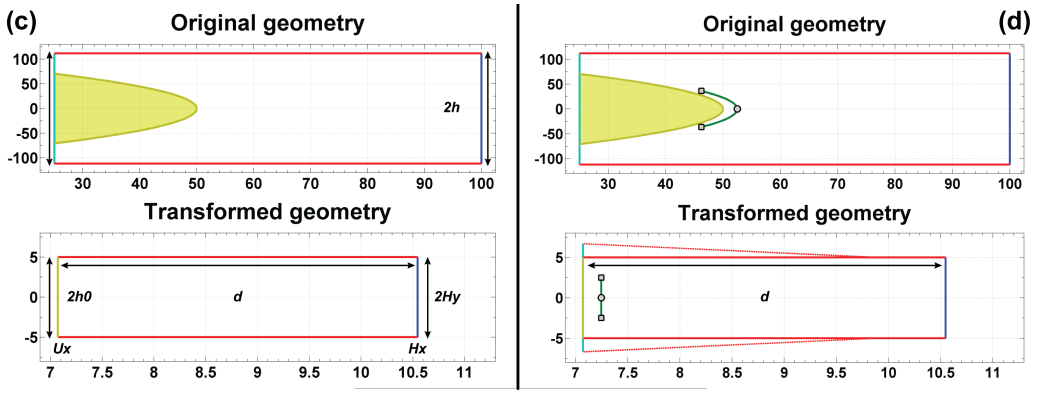

Figure 3.15: As shown in both frames (c) and (d), by translating the transformed grounded plane to H_x, where it would have been without employing such a length controlled bottom plane h, a uniform geometry is obtained. The side-bands (dashed red lines) are discarded to enforce uniform geometry (already discarded in frame (c)). See Figure 3.11 for a different approach to such a liquid droplet description.

The final step is to calculate the value of the bottom and grounded planes length h, the planes perpendicular to the capillary, such that the transformed plane length H_y, is equal to that of the transformed capillary length h_0, thus giving $H_y = h_0$. Now, for the horizontal ground-plane position L_p, and vertical bottom plane length h (original geometry), this function is given by $z = L_p + ih$. Since now employing the inverse $w = \sqrt{z}$, the vertical length in the transformed geometry is given by $H_y = \mathrm{Im}\left(\sqrt{L_p + ih}\right)$. It is therefore required to solve for h, because it is favoured to have the transformed length H_y, equal to that of the unchanged bottom plane length h_0, to enforce a uniformity. This requires finding the complex root, by using De Moivre's theorem as

$$w^{1/2} = \sqrt{r}\left[\cos\left(\frac{\theta + 2k\pi}{2}\right) + i\sin\left(\frac{\theta + 2k\pi}{2}\right)\right], \quad k = 0, 1 \tag{3.2.5}$$

where $r = \sqrt{L_p^2 + h^2}$, which can be rewritten to give the real component as

$$H_x = \pm\sqrt{r}\cos\left[\frac{\arccos\left(L_p/r\right)}{2}\right]. \tag{3.2.6}$$

These equations are not solvable analytically, which requires them to be solved numerically. Further, the transformed separation $d = H_x - U_x$ is the unchanged grounded plane position H_x, minus the backplane position U_x. To find the position of the transformed backplane U_x, the original parametric functions are transformed using $z_u = (\alpha^2 - t^2) + i(2\alpha t)$. Now, taking the real component of this, using again De Moivre's theorem with $r_u = \sqrt{(\alpha^2 - t^2)^2 + (2\alpha t)^2}$, gives

$$U_x = \pm\sqrt{r_u}\cos\left[\frac{\arccos\left((\alpha^2 - t^2)/r_u\right)}{2}\right]. \tag{3.2.7}$$

These two equations are approximated using Taylor expansions. The first expansion assumes that L_p is large relative to h, obtaining to first order that

$$H_x \approx \sqrt{L_p} + \mathcal{O}(1/L)^{3/2}. \tag{3.2.8}$$

For the second Taylor expansion, the parametric coefficient α is assumed to be large compared to the bound t (see (3.2.3)), obtaining to first order that

$$U_x \approx \alpha + \mathcal{O}(1/\alpha)^2. \tag{3.2.9}$$

Using these approximations, the transformed separation d is approximated

$$d = \sqrt{L_p} - \alpha = \frac{1}{\sqrt{2}}\left(\sqrt{2L + R} - \sqrt{R}\right). \tag{3.2.10}$$

where the ground-plane position L_p is determined by the separation distance between the capillary tip and this plane L, plus the tip position relative to the origin, as there is always this α-dependant offset (thus $L_p = L + \alpha^2$). This approximation of (3.2.10) is compared to numerical solutions in Figure 3.16.

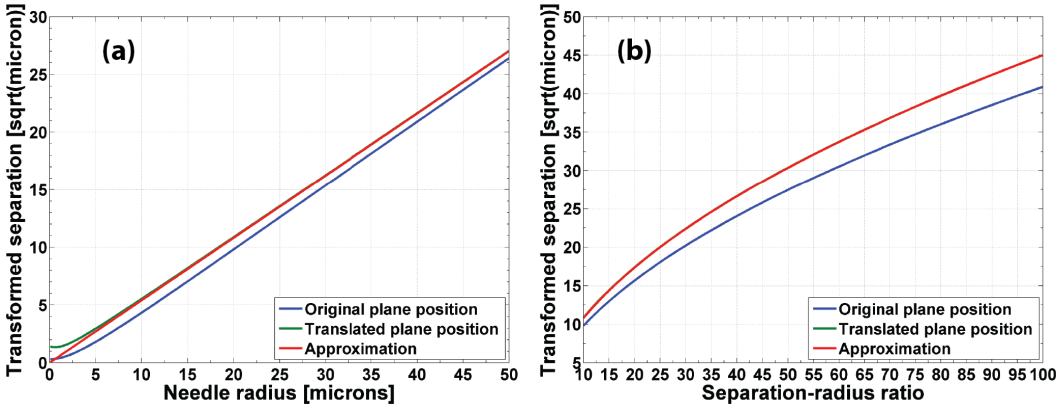

Figure 3.16: Effects of changing the parabolic radius on the transformed separation d are shown in frame (a), with the effect of changing the separation in the original geometry on the transformed geometry, shown in frame (b). Both these trends agree with what is expected from the known electrostatics theory, shown together with the approximation function. Note that in frame (b) the approximation and the numerical solution coincide. The radius and separation changes have unique trends. Also, for the MATLAB code used to generate these solutions, see Appendixes A.3 and A.4.

3.2.2 Domain uniformisation validation

To review the validity of using the domain uniformisation approach, the electric field is calculated by means of this transformed geometry, and is compared to that of the known Mason equation. Thus, using the transformed separation d, between the applied potential and the grounded plane, the field is given by

$$E_u = V/d^2 = 2V\left(\sqrt{2L+R}-\sqrt{R}\right)^{-2}. \tag{3.2.11}$$

Note, even though we assume a uniform field, the transformed separation is squared, as it is required to transform to the original geometry. The intent is to show that even though the symmetries are different, both these configurations behave similarly when being polarized. For that reason, the ratio of the current approach E_u, is taken with respect to the Mason equation E_τ

$$\phi = \frac{E_\tau}{E_u} = \frac{2d^2}{R\log(4L/R)} = \frac{2d^2}{R\log(4\beta)}, \tag{3.2.12}$$

where $\beta = L/R$ is the separation-radius ratio. Finally, expanding for R small relative to β, this ratio is approximated to be

$$\phi \approx \frac{2+2\beta-2\sqrt{1+2\beta}}{\log(4\beta)}. \tag{3.2.13}$$

The electric fields calculated by means of the transformed geometry E_u, is compared to that of the known Mason equation E_τ in Figure 3.17. The curves in frame (a) indicate that the characteristics of these two geometries are the same. The constant factor by which these curves differ is given by (3.2.13). The fact that these characteristics are the same is invaluable, as the transformed geometry can be studied analytically, and then later applying these results to the original geometry. See section 5.1.3 for an extensive discussion on this.

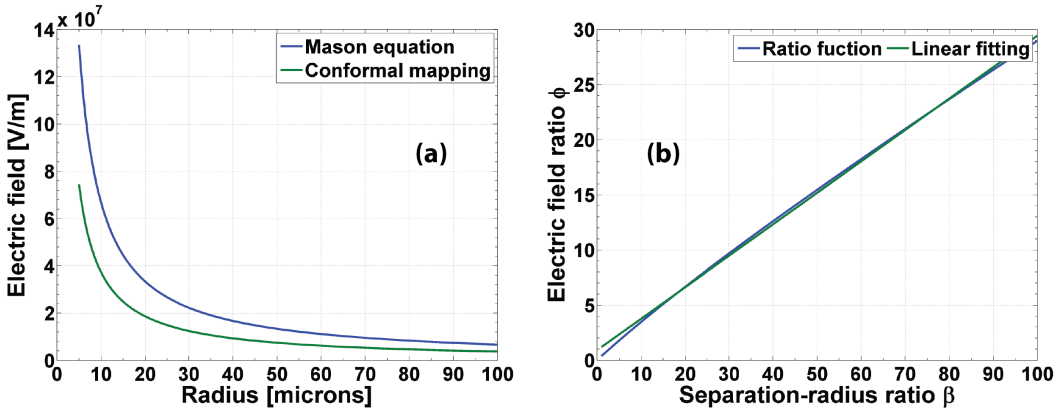

Figure 3.17: The field E_u obtained from the transformed geometry, is compared to the Mason equation E_τ in frame (a), for the case of a separation-radius ratio $\beta = 5R$. These curves indicate that the characteristics of these two geometries are the same. The constant factor by which they differ (given by (3.2.13)) is shown in frame (b).

3.3 Droplet dielectric theory

Using the transformation as described in the previous section, it is possible to obtain a uniform domain, which was shown to be solvable for these problems. The main parameter required for this is the transformed separation d between the applied potential and the grounded plane. Previously, it was shown that the effective electric field is given in terms of the depolarization factor N_p and the initial uniform electric field as

$$\mathbf{E} = \left(\frac{1}{1 + N_p\chi}\right)\mathbf{E_0}. \tag{3.3.1}$$

The geometry of the current problem is cylindrical around the horizontal axis, for which Osborn was consulted to obtain the depolarization factor [58]

$$N_p = \frac{b}{b+c}, \tag{3.3.2}$$

for $a = \infty, b \geq c$ when $a \geq b \geq c \geq 0$ are the ellipsoidal semi-axes. For the case of a uniform initial electric field $\mathbf{E_0} = V/d^2$, it gives the effective field

$$\mathbf{E} = \left(\frac{b+c}{b\epsilon + c}\right)\mathbf{E_0}. \tag{3.3.3}$$

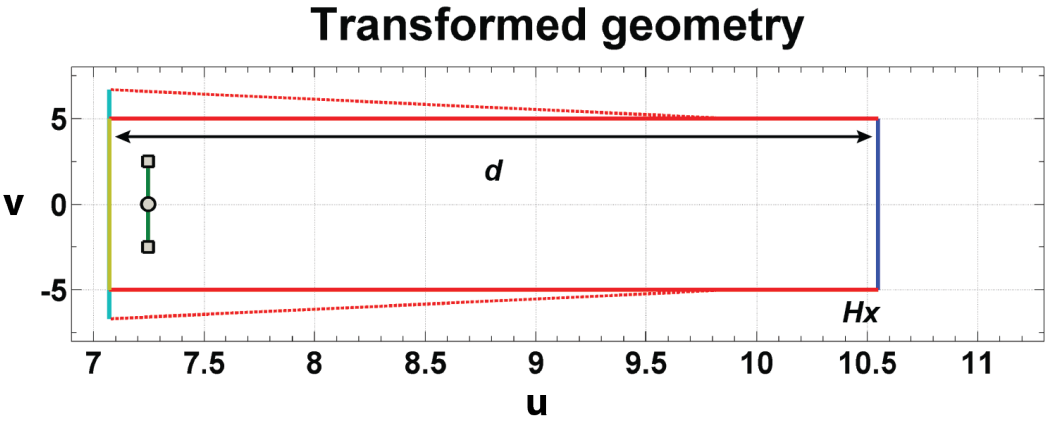

Figure 3.18: Transformed geometry of Figure 3.14 with the following assumptions: discarding of the side bands, leading to a uniform geometry. Using the transformed separation d between the potential planes, this problem is analytically solvable. Also, the green line due to the partial parabola only serves as a qualitative motivator. By using the depolarization factor N_p per (3.3.2), the droplets are defined, because by setting $b = 2c$, they are described in the simplest manner (parameters cancel out).

As taking the limit $b \to \infty$ showed to be an unreasonable approximation, a reasonable approximation is to set the cylindrical lengths $b = 2c$ in the previous equations. Assuming, the electric field will be affected minimally by setting the width of the dielectric equal to its thickness, giving

$$\mathbf{E} = \frac{3V}{d^2(2\epsilon + 1)}. \tag{3.3.4}$$

As the electric field within the dielectric is known from the above equation, by using the boundary conditions, the electric field at the boundary is given by

$$\mathbf{E}^{\perp}_{\mathbf{above}} = \mathbf{E}^{\perp}_{\mathbf{below}} + \frac{\sigma}{\epsilon_0} = \mathbf{E} + \frac{P}{\epsilon_0} \tag{3.3.5}$$

$$= \mathbf{E} + \frac{\epsilon_0 \chi \mathbf{E}}{\epsilon_0} \tag{3.3.6}$$

$$= \epsilon \mathbf{E}. \tag{3.3.7}$$

The above assumes only linear polarization $\mathbf{P} = \epsilon_0 \chi \mathbf{E}$ and is only used to calculate the field at a point on the boundary. Using this equation, the electric field at the grey circular marker in Figure 3.18 will be analytically calculated. Equations (3.3.4) and (3.3.7) show that the field is independent of all, but the plane separation distance d parameter. Only the perpendicular fields are of interest, as parallel fields are not polarization influenced (see Figure 3.19).

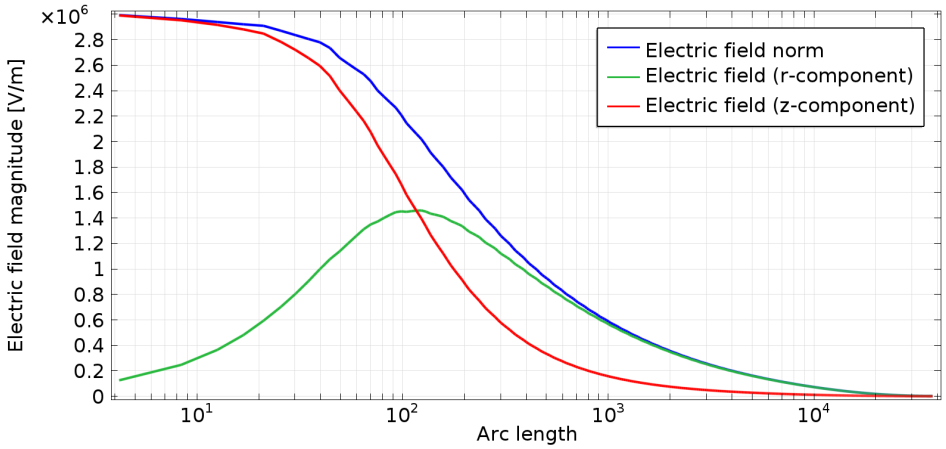

Figure 3.19: Only the perpendicular electric fields (z-component) are of interest, as the parallel fields (r-component) are zero at the capillary tip. From the boundary conditions (3.1.12) it is also known that the parallel fields are not influenced by polarization. The perpendicular electric fields will be referred to as the *maximum electric fields* at the capillary tip from this point onward. The geometry of Figures 3.1 and 3.8 was used to calculate these fields numerically (no liquid volume included), where these fields are calculated along the hyperbolic arc that starts at the tip.

3.4 Taylor-cone formation time

Kim *et al.* [62] described the use of pulsed cone-jet electrospraying to generate a series of patterned droplets. Their work showed that it is possible to generate such a series of droplets using an alternating current at certain frequencies (see Figure 3.21). We wrote a discussion in response to this paper that showed it is possible to quantise the fulcrum frequency f_c, defined as the maximum cone-formation frequency, at which the generated drops are not of a uniform nature any more [63]. Kim *et al.* did mention in their original paper that instabilities of such nature were observed when the applied voltage frequency f_v was higher than this maximum cone-formation frequency f_c, but they never proposed an equation to calculate this fulcrum frequency f_c explicitly.

Only the results from [63] are given in this section and are discussed, as that paper explains the derivation and correctness of it thoroughly. The fundamental component to calculating this frequency, is the characteristic time required for the Taylor-cone to form. This was calculated in the past by Suvorov and Zubarev for liquid metals as [64]

$$T = 3^{\frac{3}{2}} \sqrt{\frac{\rho}{\varepsilon_0^3}} \left(\frac{\pi\gamma}{E^3} \right). \tag{3.4.1}$$

They showed that the Taylor-cone formation times are given by (3.4.1) for liquid metals in a uniform external field E. This equation assumes that $E \gg E_{min}$, where E_{min} is the minimum electric field required to initiate this surface instability. The method we proposed previously assumes that the liquid droplet uniformly experiences the field generated by such a point-to-plane geometry, as described by the Mason equation [51, 63].

From electrospraying electrohydrodynamics, it is known that the rounded meniscus of the liquid droplet at the tip of a capillary, deforms into a conical shape when the applied potential is of sufficient magnitude. The fundamental assumption made here is that the drop is static in this conical shape, as that is the curvature of both maximum field divergence, and of what is experimentally observed just before the formation of the cone-jet.

Several authors, including Suvorov and Zubarev, studied the electrohydrodynamics of the droplet curvature during the cone formation [64–66]. For this work, we are however only interested in the steady-state hereof. We therefore study the meniscus after a stable cone is formed, and uses the cone-formation time as a given physical result. This characteristic cone-formation time is also affected by the charge-relaxation time τ of the liquid,

$$\tau = \frac{\epsilon}{\sigma}, \tag{3.4.2}$$

where σ is the conductivity, but generally this is several orders of magnitude smaller than that of the Taylor-cone formation time. These charge-relaxation times are generally in the range of between 10^{-10} and 10^{-5} seconds [65].

Equation (3.4.1) can be simplified by taking the following constant, resulting in the final equation for the characteristic formation time, as

$$\eta = \pi \left(3^{\frac{3}{2}}\right) \left(\sqrt{\varepsilon_0^{-3}}\right), \quad \text{suggesting} \quad T = \eta \left(\frac{\gamma\sqrt{\rho}}{E^3}\right). \tag{3.4.3}$$

The electric field E at the tip of the capillary was previously determined using the Mason equation. This is also the approach generally employed in practice, where it is assumed that the liquid behaves such as an ideal conductor, with a zero internal field. When using solvents with large dielectric constants, as the case being for common solvents, this assumption is acceptable. Note however, this equation neglects the contribution of polarization and the effect thereof on the effective electric fields. To account for the non-zero fields inside dielectrics, the correct cone-formation times can be calculated by using (3.3.7) as derived in Section 3.3, rather than using the Mason equation (3.1.4).

Using the definition of square-pulses and the relationship between time and frequency, the fulcrum frequency relation can be shown to be $f_v \leq f_c = (2T)^{-1}$ for the given assumptions. It should be noted that $2T$ is the full period of these applied voltage pulses, as Kim *et al.* defined T to be the half-period, therefore being the formation time. They employed a capillary-to-plane configuration with both stainless steel capillaries and substrates. The capillaries had inner and outer diameters of 200 and 500 μm respectively, positioned 1 mm above the moving substrate. The substrate was translated using a moving stage at a speed of 2 mm/s. See Figure 3.20 for a schematic of their setup. Positive pulsed square-waves were applied to the capillary with a peak of 1.0 kV, with the duration of the pulses set to half of a period. The substrate was connected to a DC voltage source which supplied a negative biased voltage of 2.0 kV.

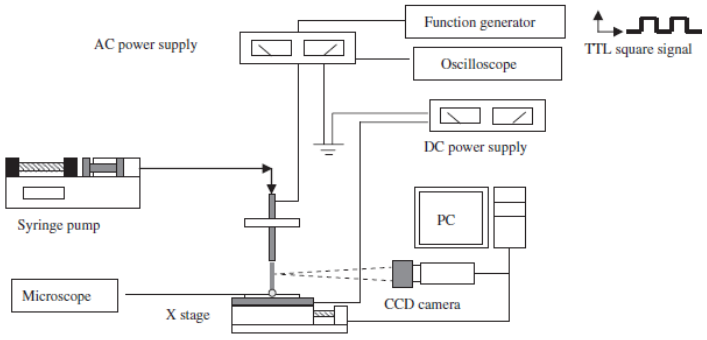

Figure 3.20: Schematic diagram of the experimental configuration as employed by Kim *et al.* They employed a capillary-to-plane configuration with both stainless steel capillaries and substrates. The substrate was translated using a moving stage at a speed of 2 mm/s. Positive pulsed square-waves were applied to the capillary with a peak of 1.0 kV. The substrate was connected to a DC voltage source which supplied a negative biased voltage of 2.0 kV. Reprinted with permission from Elsevier [62, 63].

For their experimental configuration, the formation time is calculated to be $T = 43$ ms, when using (3.3.7) as derived in Section 3.3, rather than using the Mason equation (3.1.4). However, when using the Mason equation, a formation time of $T = 41$ ms is obtained, as we have previously reported [63]. Using these times, the new fulcrum frequency is calculated to be $f_c = 11.6$ Hz, compared to the previous value of $f_c = 12.2$ Hz.

As for the previous method, the new method agrees with the experimental observations of Kim *et al* [62, 63], such as shown in Figure 3.21. Frames (c) and (d) are clear indicators of $f_v \geq f_c$. It should be noted that ethylene glycol, which was used during these experiments, has a large relative permittivity of $\epsilon = 37$. This makes it difficult to distinguish between these two results.

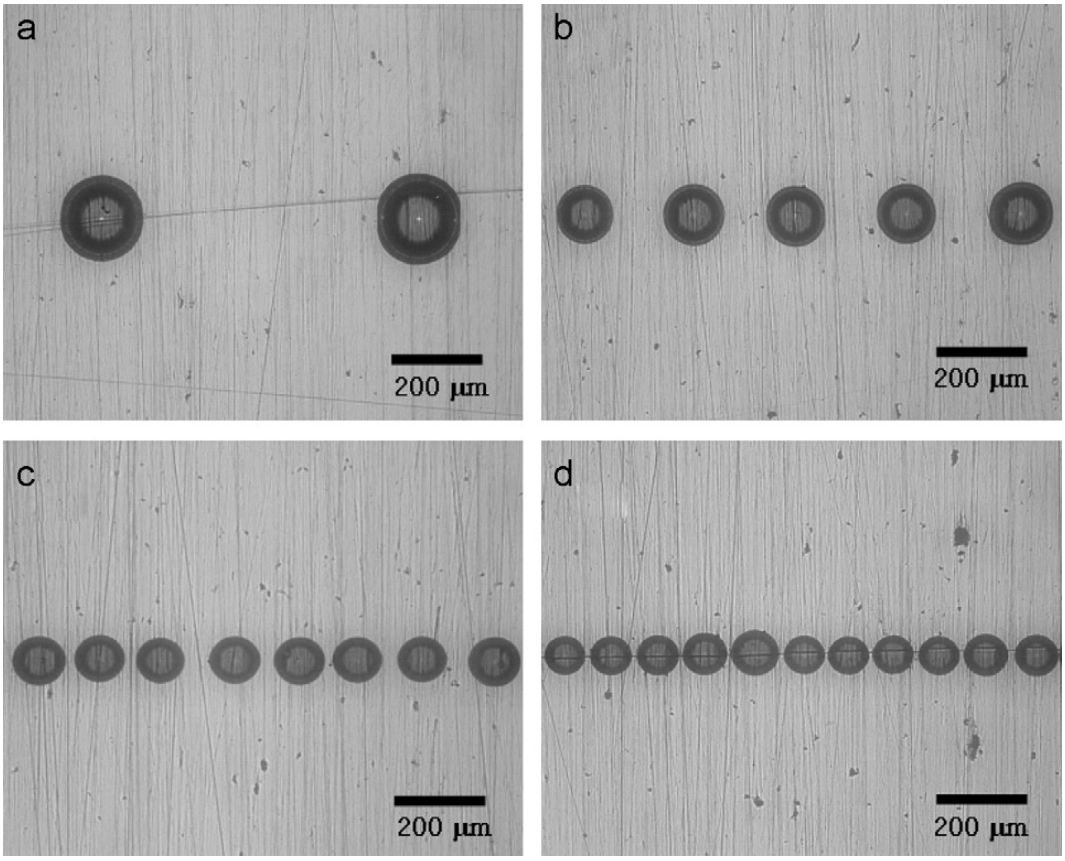

Figure 3.21: Patterns of a series of deposited drops at pulsating frequencies f_v of (a) 2.5, (b) 7.5, (c) 15, and (d) 25 Hz, for a fulcrum frequency f_c of 12 Hz per the above equations. From the last two frames, the non-uniformity of droplet spacing and size is an indicator of $f_v \geq f_c$. Note, ethylene glycol, containing methylene blue, was used as spraying fluid, which was supplied to the capillary with a syringe pump at a fixed flow rate of 3 nl/s. The only physical properties required for the specific calculations are the surface tension, which is 48.0 mN/m, and the liquid mass density which is 1113 kg/m^3. Reprinted with permission from Elsevier [62, 63].

3.5 Surface tension measurement

Surface tension is the property of the liquid free surface that allows it to resist an external force. Because surface tension showcases in many effects, there are a number of paths to measuring it. Some of these include the capillary rise, Du Noüy ring, drop weight, and the bubble pressure methods [67, 68]. The best method to be used depends on the nature of the liquid investigated and the conditions under which the measurement takes place. However, most of these methods require a relatively large amount of liquid, generally varying between 10 and 30 mL [69], to determine the surface tensions accurately. Recently, there have been developments regarding a minimized version of the Du Noüy ring method, which only requires about 50 μL. Most of these systems operate in the range of 1 to 2000 mN/m with a standard resolution of 1 μN/m. Advanced Du Noüy ring method systems have resolutions up to 0.1 μN/m.

3.5.1 Proposed method

From theory introduced in the literature review, the surface tension is obtained by rewriting (2.1.2) as

$$\gamma = \frac{\varepsilon_0}{R}\left(\frac{V}{\ln\left(\frac{4L}{R}\right)}\right)^2, \tag{3.5.1}$$

which is simplified by taking the following geometrical constants:

$$\alpha = \frac{\varepsilon_0}{R} \quad \text{and} \quad \beta = \left(\ln\left(\frac{4L}{R}\right)\right)^{-1}, \quad \text{suggesting} \quad \gamma = \alpha\left(\beta V\right)^2. \tag{3.5.2}$$

The proposed method is to recognise at which applied potential the liquid is being electrosprayed, as the potential at which this process occurs is directly proportional to the liquid surface tension. Therefore, using (3.5.1), it is possible to determine the surface tension from the voltage measurement at which spraying initiates. Electrospraying is detected through current measurement. There is no net stable currents in the system until a stabilised cone-jet forms, as then current is created because of the physical flow of charged particles from the capillary to the collecting counter-electrode.

Using software it is possible to program a direct current voltage source in such a manner that it iterates from zero voltage in increments until a net stable current is detected in the system. When such a current is detected, the specific applied voltage value can be used to determine the surface tension of the liquid under investigation. The entries in Table 3.1 were calculated using (2.1.2) and (2.1.4), using a radius of $R = 5$ μm and separation distance $L = 50$ μm. These parameters are proposed to build a proof of concept system, which should be optimized according to the experimentally obtained results.

3.5.2 Electric field limitations

The main effects that limit the capabilities of the proposed system are corona and electrical discharges, which have already been introduced and discussed in previous sections. Previous research detailed in [70] proposed a model for calculating corona thresholds (E_C) in terms of the specific geometry, and the relative permittivities of the liquids to be electrosprayed. For this method, an average relative permittivity $\epsilon = 10$ is used to determine the maximum surface tensions measurable under atmospheric conditions before discharge onsets,

$$\gamma_C = \frac{R\varepsilon_0}{4} E_C^2, \quad \text{suggesting} \quad \gamma_C \sim R^{-0.5}. \tag{3.5.3}$$

Minimizing the separation distance L ($L = 10R$, $R \ll L$), it can be shown from the above that the surface tension constraint is primarily influenced by the radius. Applying these assumptions, and using the corona threshold,

$$E_C = \left(\frac{2\epsilon + 1}{2\epsilon}\right) E_O = \left(\frac{2\epsilon + 1}{2\epsilon}\right) \left(62.7 + 1.74R^{-0.75}\right), \tag{3.5.4}$$

the maximum surface tension functions are plotted in Figure. 3.22. The Rousse model E_O (which does not account for this polarization), is compared with the previously proposed model of the authors. For the minimum radius simulated ($R = 5$ μm) an upper limit of ~ 80 mN/m is obtained.

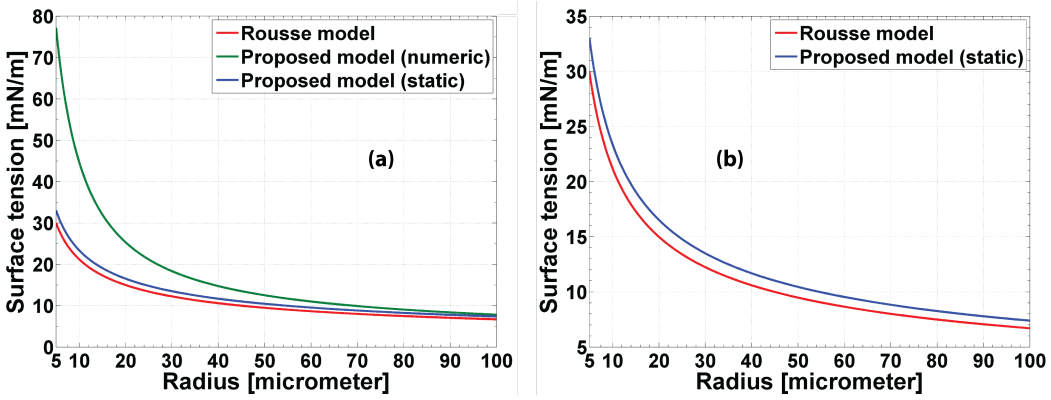

Figure 3.22: Maximum surface tensions versus capillary radii, for the Rousse and proposed models, compared for the parameters given previously. For this system, an average relative permittivity of $\epsilon = 10$ is used. For the proposed model, the adaptive coefficient was used, as described in Section 5.1.1 (labelled as *numeric* in frame (a)). Frame (b) compares the Rousse and proposed models, for the case of using the static coefficient, as described here by (3.5.4), in which $b = 2$ from the numeric coefficient. The numeric model accounts for the radius dependence of the depolarization factor, hence the significant difference between the numeric and static curves in frame (a).

3.5.3 Measurement accuracy

The accuracy of the proposed method mainly depends on the synchronization quality between the ammeter and voltage source. When a change in current is detected, the surface tension can be calculated from the voltage. Due to the quadratic form of (3.5.2), measurements will be more accurate for lower surface tension liquids. These measurement accuracies primarily depend on the voltage source resolution. Although voltage resolutions of 2 mV are obtainable [71], a resolution of 10 mV is assumed for these discussions and Figure 3.23.

3.5.4 Separation distance

The separation distance was chosen to be 50 μm, because it is 10 times that of the capillary radius. Such a separation-radius ratio α will result in the highest corona thresholds, enabling measurement of the higher surface tension liquids. Such distances can be accomplished accurately using nanosteppers [72]. Using such a distance, the majority of pure liquid compounds could be measured by applying less than $\sim$ 800 V (neglecting cone length relative to separation) [73].

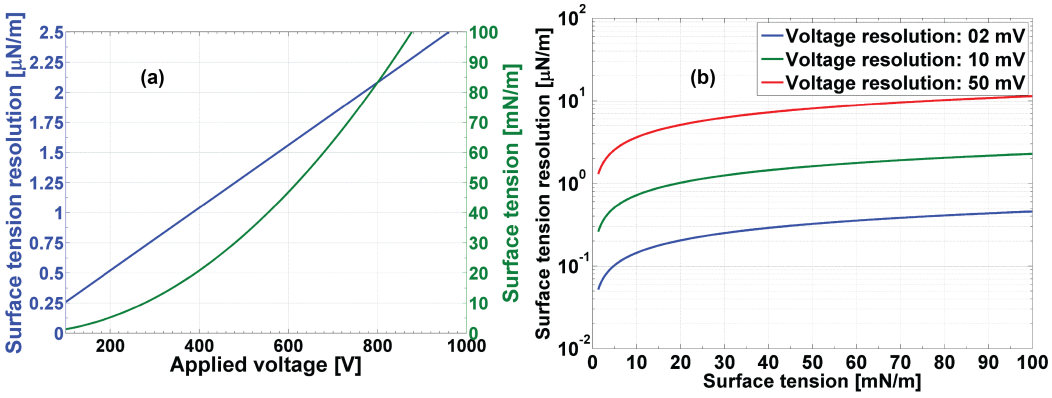

Figure 3.23: The surface tension, and the respective resolutions, versus the applied voltage. The resolution curve is for a 10 mV voltage resolution, with an average of 2 μN/m over the given surface tension range, are shown in frame (a). Frame (b) shows the surface tension resolutions versus the surface tension. Each of these three voltage resolutions are obtainable with current high-end voltages sources [71].

3.5.5 Liquid temperature

For most surface tension measuring methods, measurements are performed at room temperature. Using the proposed method, it will be possible to heat or cool the capillary with the liquid sample inside. This would make it possible to do measurements at most temperatures. Even if the liquid expands thermally,

it will not affect the measurements acutely, as only when the electrospraying process initiates, a current will be detected. Borosilicate glass is known for its low thermal expansion coefficient and high thermal softening point of $\sim 820\,^{\circ}\mathrm{C}$, suggesting that a broad temperature range will be available for measurements.

Further, it is assumed that these measurements are conducted at an approximately zero applied hydrostatic pressure. Non-zero pressures from increased flow rates will increase the measurable ion currents. As this will influence the starting voltages, it is not desired for this method of measurement.

3.5.6 Measurement time

The amount of time required for the Taylor-cones to form is of importance, because that will determine the total time required to analyse a sample. Equation (3.4.3) contains two unknowns, the surface tension and liquid mass density, while there is no physical relationship between these two properties. The known relationship between the voltage, and the surface tension, and electric field simplifies this equation further, with only the mass density remaining as an unknown. Due to the lack of a physical relationship between the surface tension and mass density, it is required to assume that the liquid has a density as large as possibly 2000 $\mathrm{kg/m^3}$. Using this approach, the maximum time required per voltage interval is calculated, enabling allocation of sufficient time to each interval. The voltage range can be optimised to detect lower surface tensions, while the maximum is determined by the corona discharge thresholds. See Figure 3.24 for the voltage dependence of these formation times. The total measurement time is ~ 500 ms for the proposed parameters.

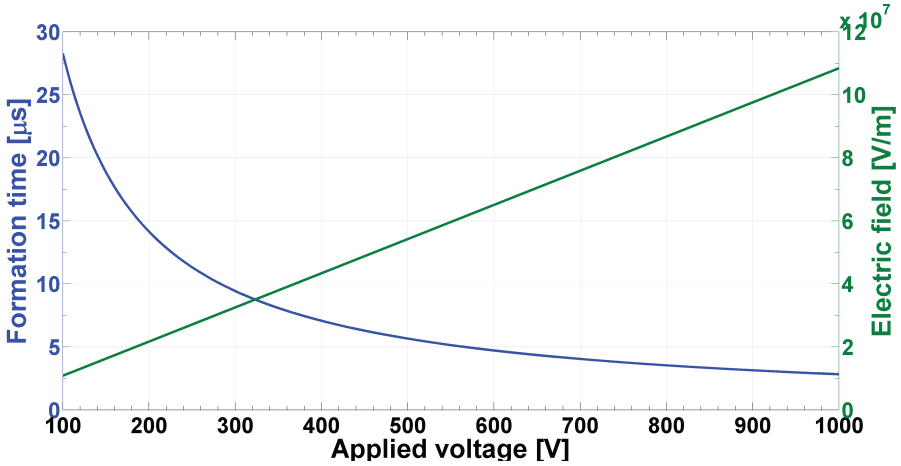

Figure 3.24: Taylor-cone formation times versus the applied voltage. Also shown, are the electric fields corresponding to these applied voltages. Even though the field linearly increases relative to the applied voltage, the formation time decreases much faster due to the cubic nature of (3.4.1) as discussed in Section 3.4.

3.5.7 Comparison with other methods

The proposed method promises numerous benefits over current methods of measuring surface tension. Unlike other methods, which are restricted to certain liquids, it is possible to use this method with various liquids. Due to the low flow rates a sample volume of less than 5 μL would be required, which is a fraction of that used by current methods. Should it for example be required to do measurements at various temperatures, hundreds of measurements could be made using one sample. The measurement time of 500 ms per sample, is relatively fast in comparison with current methods. Other than in conventional methods, a faster operation time does not affect the measurement accuracy. Comparing the method to current methods, it is comparable in accuracy, having a standard resolution of 2 μN/m for a voltage resolution of 10 mV. Using the high-end voltage sources currently available, the surface tension resolution can be improved up to 0.2 μN/m, comparable with high-end tensiometers.

Table 3.1: Physical properties and experimental parameters of common liquids at STP conditions [74–77]. The symbols used for the columns are; surface tension γ, relative permittivity ϵ, conductivity K, applied potential V, and the measurable ion currents I in SI-units (except for the surface tension which is in mN/m).

Liquid	γ	ϵ	K	V	I
Acetic acid	27.10	6.20	1.12×10^{-6}	456	21.7×10^{-9}
Acetone	22.72	21.0	0.18×10^{-6}	418	14.7×10^{-9}
Ethanol	21.97	25.3	0.50×10^{-3}	411	0.82×10^{-6}
Ethylene glycol	47.70	37.0	1.07×10^{-4}	605	0.68×10^{-6}
Nitromethane	37.48	39.4	0.50×10^{-6}	537	43.0×10^{-9}
Toluene	28.40	2.40	0.40×10^{-9}	467	0.30×10^{-9}
Water (deionised)	71.99	80.1	5.50×10^{-6}	744	0.14×10^{-6}

3.6 Chapter contributions and summary

The fundamental contribution of this chapter is the derivation of a new model to describe the polarization fields of point-to-plane electrospraying geometries analytically. This model is compared later with both a numerical simulation, and the results of a different polarization model. In addition, it was also shown how to more accurately determine the characteristic Taylor-cone formation times when considering polarization. These results were combined to propose a new method to theoretically measure liquid surface tensions.

Chapter 4 | Numerical analysis

> *The limitations of the human mind are such that it cannot grasp the behaviour of its complex surroundings and creations in one operation. Thus the process of subdividing all systems into their individual components or "elements", whose behaviour is readily understood, and then rebuilding the original system from such components to study its behaviour is a natural way in which the engineer, the scientist, or even the economist proceeds.*
> – O.C. Zienkiewicz & R.L. Taylor, *The Finite Element Method [78].*

The majority of research presented in this thesis is founded on numerical work, which was realised primarily with COMSOL Multiphysics, a popular commercial finite element analysis (FEA) package [60]. Other numerical work, including data and dimensional analysis, were realised with MATLAB. This chapter starts off with a short and concise introduction of the fundamental concepts of finite element analysis, but as it is a well-known and long established package used, the more detailed and technical aspects are not fully discussed. For that matter, the texts by Akin, Zienkiewicz and Taylor, and Rao can be consulted, which were also the main references for that subsection [78–80]. Introductions to the concepts of dimensional analysis are also given.

4.1 Finite element analysis

The practical application of finite element analysis (FEA) to modern engineering problems has been employed and improved over the last half-century. The application of FEA to fully describe the three-dimensional electrostatic field distributions in 1967 being a revolutionary application thereof [81]. The most important advantage of FEA is the ability to model arbitrary geometries with general boundary conditions. Especially for the scenario of elliptical boundary conditions, FEA can solve such problems with both high computational and storage efficiencies, including problems such as heat conduction, electric and magnetic field distributions, and idealised fluid flow. Each of these problems are described using quasi-harmonic equations, which are the class of equations which include the Laplace and Poisson equations [78, Chapter 7].

For the majority of practical problems, it is required to find a field variable as a function of its spatial coordinates. When the problem is in the unsteady state, it is also required to describe the field in terms of a temporal coordinate, though in this work only static problems are studied. The fundamental concept of FEA is to discretize the domain (generally arbitrarily) of the problem into smaller and regular subdomains, referred to as the finite elements. This is the process of changing a problem of an infinite amount of degrees of freedom, to a problem of a finite number of degrees of freedom. There are a large variety of methods to be used in these discretization processes. COMSOL is supplied with an automatic mesh generation feature. For a detailed review of different discretization methods, see the text of Rao [80, Chapter 2].

The configuration of a capillary needle perpendicular to an infinite plane, a three-dimensional problem, can be described using two independent spatial coordinates. These idealizations are possible due to the axisymmetric nature of this configuration. Other examples of such symmetries include storage tanks and rockets nozzles. By taking advantage of these symmetries simplifies both defining the problem numerically and the computation time required to solve it accurately. The convergence of the solution is directly dependant on the reference element size h, suggesting thorough investigation into optimal element sizes. The most accurate solutions are generally obtained using smaller elements. A general rule is to set the element size inversely proportional to the gradient of the field at the specific coordinates. See Figure 4.1 for the case of a circular aperture in a rectangular two-dimensional plate.

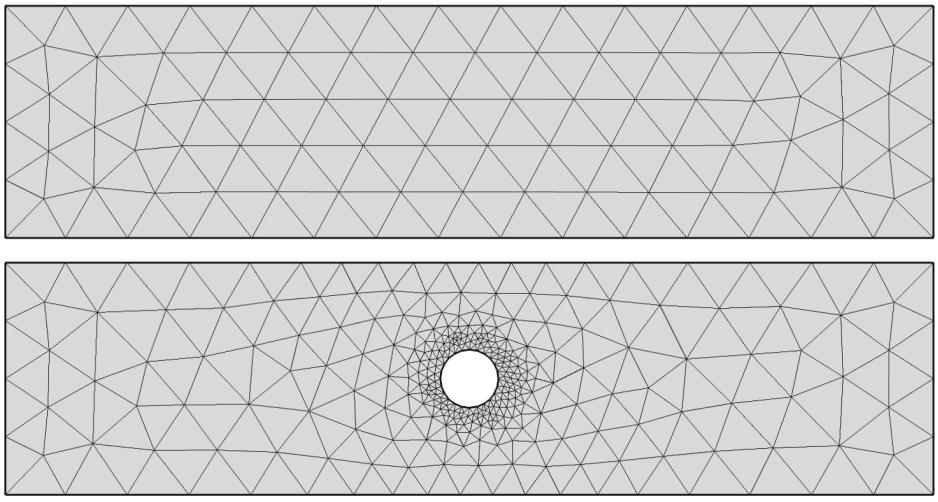

Figure 4.1: The primary element used in two-dimensions is the triangle, which is used to produce quadrilateral elements. The element sizes are much smaller near the aperture, as more elements are needed to find accurate solutions for higher gradients. The aperture is given to indicate the effect of higher gradients on the meshing.

Even though an increase in the number of discretization elements results in more accurate field solutions, there are a certain number of elements beyond which the accuracy cannot be improved for any given problem. Further, there is also a computational limit on the minimum size of these elements.

4.1.1 Mathematical background

Mathematically speaking, FEA is an integral formulation, which is generally obtained using either the weighted residual or variational formulations. The basic concepts of the weighted residual will now be discussed. See the text of Akin for more information [79, Chapter 1]. For the weighted residual method, the governing differential equation L of the unknown ϕ should be satisfied on the domain Ω for the source term Q, thus

$$L(\phi) = Q. \tag{4.1.1}$$

The unknown is now approximated for the spatial distributions $h_i(x)$ of it, which have the associated weighted coefficients Φ_i^*, such that

$$\phi(x) \approx \phi(x)^* = \sum_i^n h_i(x)\, \Phi_i^*. \tag{4.1.2}$$

Substituting this approximation into the differential equation introduces a residual error R, which we include in a weighted integral set to zero,

$$I_i = \int_\Omega w_i\, R\, d\Omega = 0, \tag{4.1.3}$$

resulting in the same number of n equations as the amount of unknown Φ_i^* coefficients. By substituting an assumed spatial solution for the approximate solution and the weighting function, the resultant set of equations are solvable for the elements in this approximation. Importantly, before solving this set of equations, the boundary conditions should be incorporated. See Figure 4.2 for a solution to the geometry of Figure 4.1 using COMSOL Multiphysics [60].

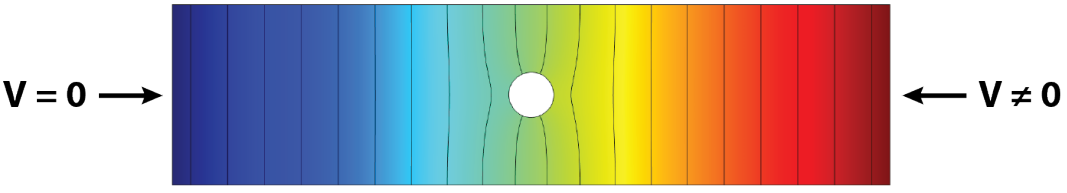

Figure 4.2: The electric potential of a rectangular metal plate with an aperture, obtained using finite element analysis using COMSOL Multiphysics. The left-hand side of the plate is at zero potential, while the right-hand is at a positive potential.

4.1.2 Electrospraying geometry

The capillary needles are described mathematically, and in the literature using a high eccentricity hyperbola. For that reason, it is modelled numerically using a revolving hyperbola with the parameterisation variable t as

$$x(t) = a\cosh(t) \quad \text{and} \quad y(t) = b\sinh(t). \tag{4.1.4}$$

The tip radius of curvature is calculated to be $R = b^2/a$ with the parameters $a = 4096$ m set to be constant and $b = \sqrt{aR}$, in order to obtain an eccentricity close to one, as required by the analytical definition. The radius parameter R is used to specify the tip radius implicitly during simulation. The hyperbola dimensions are determined by using the maximum bound parameter $t = Q$. This axisymmetric geometry is shown in Figure 4.3 for arbitrary parameters.

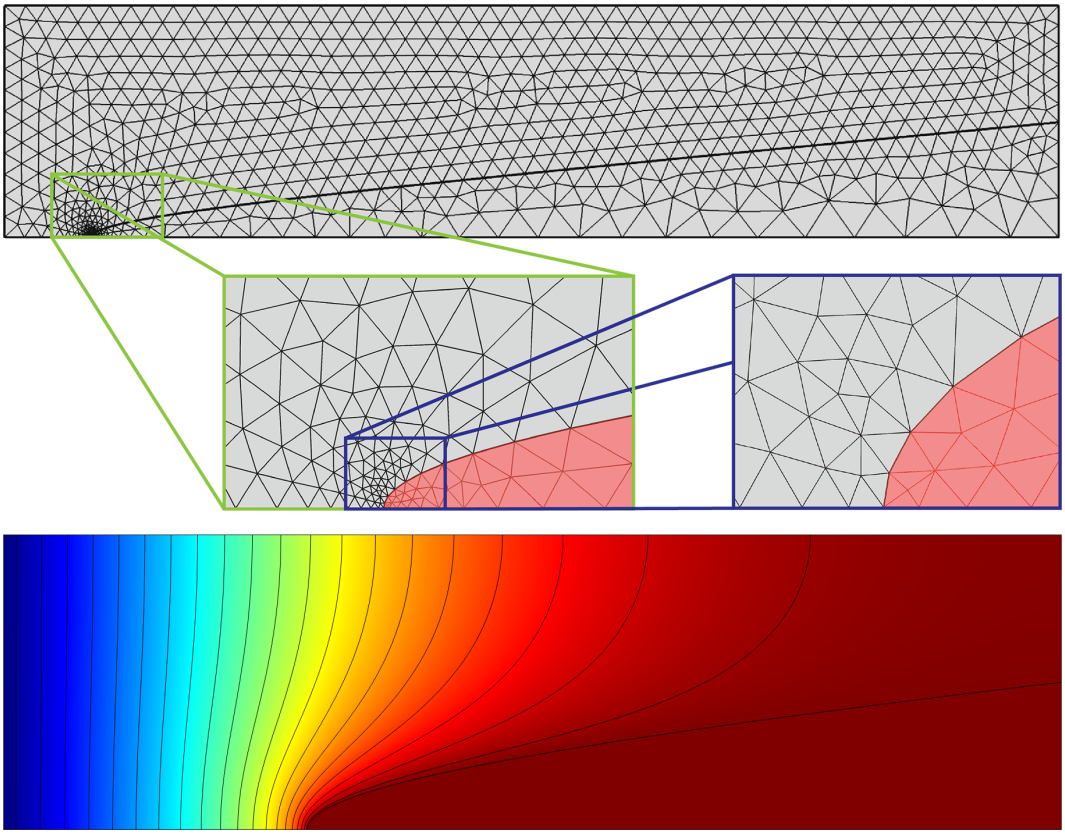

Figure 4.3: The automatically meshed capillary needle which is modelled using hyperbolic functions. Two enlargements are included to indicate the element shapes, especially when focussing on the needle tip, compared to the overall geometry. In the enlargements, the capillary surface is emphasized using the pink filling. The electric potential field associated with the given capillary needle is also shown. Generating this result, a considerably finer mesh than in the above figure was used.

4.1.3 Error analysis

An important concept when using and studying finite element analysis (FEA) is that of error analysis. For this discussion, it will be assumed that integral forms, as described in the previous section, are used with the highest derivative thereof given by the integer m. For ease of discussion, it is assumed that all elements have the same shape and interpolation function, with specific element sizes h and complete interpolation polynomial of integer degree p. For a smooth solution, the local finite element error is proportional to [79, Chapter 1]

$$e(x) \propto h^p \frac{\partial^m u(\mathbf{x})}{\partial \mathbf{x}^m}, \tag{4.1.5}$$

which suggests that, when there are larger gradients, it is required to make the elements smaller. Similarly, when the gradients are small, larger elements could be used to obtain the same desired error. COMSOL has an automatic meshing feature, which takes this into consideration. As can be see in both Figures 4.1 and 4.3 where there are regions of high gradients.

For the capillary-plane (also called point-plane) geometry used in this work, this error proportionality indicates a problem. From the analytical definition, the capillary is required to be infinitely long relative to the plane, requiring the use of a large parametric bound $t = Q$ (4.1.4) to approach this definition. As the capillary length increases, the total domain area also increases, leading to either larger average elements, or a mesh impossible to solve with standard computing capabilities. See Figure 4.4 for the exponential nature of this effect.

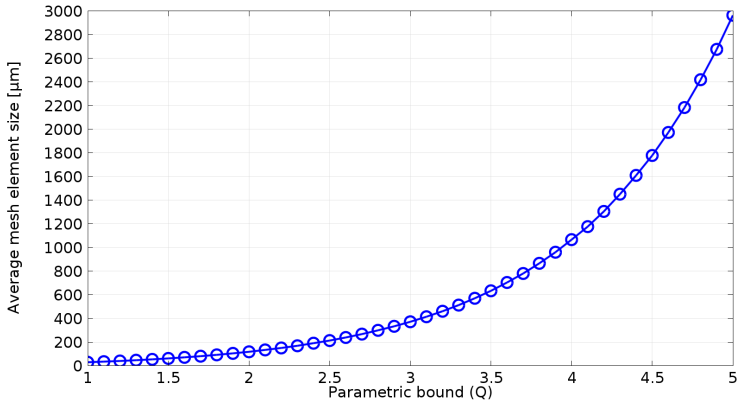

Figure 4.4: The average mesh element size associated with the capillary needle for different parametric bound $t = Q$ values. Note the exponential nature thereof. This meshing technique, called physics-controlled meshing, uses predefined meshing element sizes appropiate for given physical scenarios. This is different from what is known as element refinement meshing, which adapts the element size according to an error analysis done on an iterative basis [60].

This effect becomes even more pronounced when reducing the radius of the capillary, and therefore increasing the gradient around the tip. Another error estimator is the mesh quality factor, which is the ratio between the largest enclosed and smallest circumscribed sphere of each element. Values closer to unity indicate higher mesh quality, the minimum element quality generally being the weakest link in the simulation. See Figure 4.5 for the dependence of this indicator on the radius. Qualities above 0.7 are considered adequate [82].

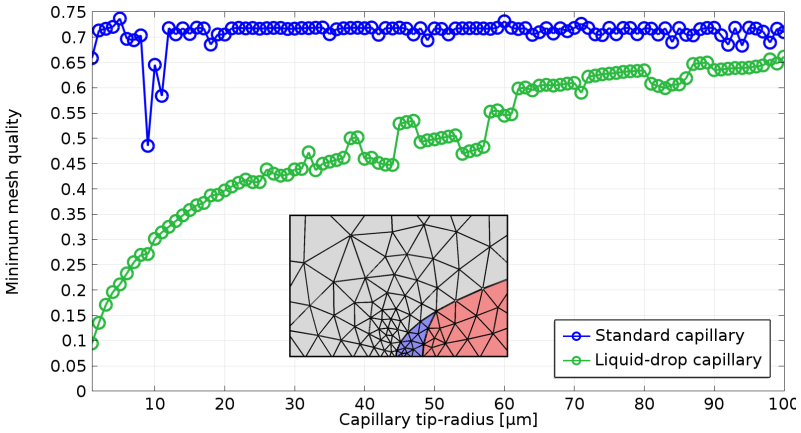

Figure 4.5: The minimum mesh element quality associated with the capillary needle for different tip radii. Mesh quality factors are given for the standard (blue) and the liquid-drop (green) configurations. Note drastic quality decrease for the liquid model, for which an example of such a liquid-drop geometry (blue filling) is imposed. Here the standard capillary is the standalone orange body, ignoring the blue liquid filling.

From Figure 4.5, it can be seen that for the scenario of a standard capillary, the mesh quality is generally the same for all radii. This is primarily due to the intelligent automatic mesh optimization by COMSOL. However, when the liquid is included in the simulation (see inset of Figure 4.5), the mesh quality decreases with capillary radii. As the geometry is modelled using hyperbolic functions, the intersection of these functions at the liquid-capillary interface leads to complicated (and also low quality) mesh elements.

4.2 Dimensional analysis

The use of dimensional analysis is extensive, mainly being used for problems having no known solvable theory. Generally the results obtained serve as a hint to the solution or as a more useful method of understanding large datasets. The brief introduction given in this section is of such a nature to understand the use of dimensional analysis for the electrostatic problems at hand. For more detailed information, see Price, van Groesen and Molenaar [83][84, Chapter 1].

For interest sake it should be mentioned that one of the most famous cases of using these methods were when Taylor very accurately predicted the estimate strength of the first atomic bomb of 1945 [85]. He also happened to be one of the pioneers in the field of electrospraying, as he described the cone (hence today the Taylor-cone) observed in electrospraying theoretically in 1964 [86].

A mathematical model is considered solved when there is an usable solution between the dependant and independent variables thereof, examples being the position and time as the dependant and independent variables respectively. As the problem at hand is electrostatic, there is no such a time dependence, but it is preferable to find the electric fields in terms of the relative permittivities of the system. All the system variables and parameters have physical dimensions, which can be expressed in terms of the fundamental dimensions. This property is the basis of dimensional analysis, as according to the rule that all the terms in any particular equation must have the same dimensionality. This results in the condition that an equation should be independent of the system of units used, although the dimensionality of coefficients are not restricted. Finally, the existence of dimensionless numbers allows drawing conclusions without solving the ruling mathematical equation of the system. The key steps for this procedure (see the article by Price for detailed information) are [83]

First Define a preliminary model F with one dependant variable. This entails tabulating all of the variables and parameters that are initially believed to govern the physical system (therefore the dependant variable). Often the physical model contains more variables than the mathematical model.

Second Find the nondimensional forms that these these variables can take.

Third Reassemble the initial nondimensional basis variables optimally.

The nondimensionalization of a mathematical model is the removal of all physical units from an equation using a suitable substitution of variables. This results in shedding light on the scaling properties of the system without solving the ruling model completely. The step used of finding a basis of nondimensional variables follows that of Price, and not the Buckingham Pi theorem as generally used. The method of Price delivers the same result, though it rather makes use of the nullspace basis, which is considered much simpler than other methods. The arbitrary change of variables for a dimensional variable X_i is

$$X_i' = \alpha_1^{D_{1i}} \alpha_2^{D_{2i}} \cdots \alpha_M^{D_{ji}} X_i, \tag{4.2.1}$$

where each α represents a dimensional variable up and until the J fundamental units of the system, with D_{ji} the dimensional matrix, which is the dimension of the i-th dimensional variable with respect to the j-th fundamental unit. A physical model of I dimensional variables can be written as

$$F(X_1, \cdots, X_I) = F(\alpha_1^{D_{11}} \cdots \alpha_M^{D_{j1}} X_1, \cdots, \alpha_1^{D_{1I}} \cdots \alpha_M^{D_{jI}} X_I), \tag{4.2.2}$$

which leads to the matrix form,

$$D_{ji}S_i = 0, \tag{4.2.3}$$

where $\mathbf{S}$ is an unknown $I \times 1$ vector of the logarithmic derivatives of F. It is found that the dimensional variables X_i must satisfy the condition

$$\Pi_k = X_1^{S_{1k}} X_2^{S_{2k}} \cdots X_I^{S_{Ik}} = \mathbf{X}^{\mathbf{S_k}}, \tag{4.2.4}$$

where $\mathbf{X} = [X_1, X_2, \cdots X_I]$ are the dimensional variables in a vector format, corresponding to the order of the dimensional matrix $\mathbb{D}$, with Π_k being the Pi-variables, similar to those obtained from the above mentioned Buckingham Pi theorem. The relationship among these variables are given as

$$\Pi_1 = F(\Pi_2, \Pi_3, \cdots, \Pi_K). \tag{4.2.5}$$

The nondimensional variables can therefore be obtained by determining the nullspace of (4.2.3), which is usually an underdetermined system. It is very important to note that there are many different vectors that are contained within the nullspace of the dimensional matrix $\mathbb{D}$, meaning that the obtained solutions are generally not unique, but rather depends on the order in which variables are listed in the dimensional matrix.

The inclusion of an unnecessary variable will not tarnish the results, it will only add an additional nondimensional variable. Sometimes the omission of a relevant variable is noticeable when it is not possible to nondimensionalize the dependant variable, although it is possible under certain conditions to still perform nondimensionalization with the other variables at hand. Ample judgement should therefore be used when deciding which variables to include in the physical model initially, required for the dimensional matrix.

4.2.1 Electrospraying electrostatics

For the problem at hand, determination of the total electrical field E due to both the applied electric potential V and the liquid polarization effects (from ϵ), a dimensional matrix $\mathbb{D}$ is defined as

$$\mathbb{D} = \begin{array}{c} \\ m \\ l \\ t \\ i \end{array} \begin{array}{c} \begin{array}{cccccccccc} E & \epsilon & V & L & R & S_1 & S_2 & S_3 & E_0 & E_F \end{array} \\ \begin{pmatrix} 1 & 0 & 1 & 0 & 0 & 0 & 0 & 0 & 1 & 1 \\ 1 & 0 & 2 & 1 & 1 & 1 & 2 & 3 & 1 & 1 \\ -3 & 0 & -3 & 0 & 0 & 0 & 0 & 0 & -3 & -3 \\ -1 & 0 & -1 & 0 & 0 & 0 & 0 & 0 & -1 & -1 \end{pmatrix} \end{array},$$

where the dependent E and independent variables ϵ are given in the first and second columns respectively, followed by the parameters and the boundary conditions (E_0, E_F) of the dependent variable (see the nomenclature section).

This is the general ordering convention used when solving this nullspace, resulting in the solution vector

$$\mathbb{S} = \begin{array}{c} \begin{matrix} \Pi_1 & \Pi_2 & \Pi_3 & \Pi_4 & \Pi_5 & \Pi_6 & \Pi_7 & \Pi_8 \end{matrix} \\ \begin{pmatrix} 0 & 1 & 1 & 1 & 2 & 3 & -1 & -1 \\ 1 & 0 & 0 & 0 & 0 & 0 & 0 & 0 \\ 0 & -1 & -1 & -1 & -2 & -3 & 0 & 0 \\ 0 & 1 & 0 & 0 & 0 & 0 & 0 & 0 \\ 0 & 0 & 1 & 0 & 0 & 0 & 0 & 0 \\ 0 & 0 & 0 & 1 & 0 & 0 & 0 & 0 \\ 0 & 0 & 0 & 0 & 1 & 0 & 0 & 0 \\ 0 & 0 & 0 & 0 & 0 & 1 & 0 & 0 \\ 0 & 0 & 0 & 0 & 0 & 0 & 1 & 0 \\ 0 & 0 & 0 & 0 & 0 & 0 & 0 & 1 \end{pmatrix} \end{array}.$$

Using the above, the following nondimensional variable basis is found:

$$\begin{aligned} \Pi_1 &= \epsilon & \Pi_5 &= E^2 S_2/V^2 \\ \Pi_2 &= EL/V & \Pi_6 &= E^3 S_3/V^3 \\ \Pi_3 &= ER/V & \Pi_7 &= E_0/E \\ \Pi_4 &= ES_1/V & \Pi_8 &= E_F/E. \end{aligned}$$

These basis variables indicate that the mathematical model is dependent on all of the defined physical variables. See Figure 3.8 for details regarding the liquid-droplet length S_1, surface area S_2 and volume S_3 for the given hyperbolic geometry. The interpretation of the above is done in the results section.

4.3 Chapter contributions and summary

The primary purpose of this chapter was to explain the finite element analysis theory, as employed by COMSOL Multiphysics. A special focus was placed on the error analysis of these results, as this package was solely used to generate the numerical results of this thesis. Another important subsection described the geometry used during these simulations and how it relates to general point-to-plane electrospraying geometries.

The chapter is concluded with a subsection on dimensional analysis. Techniques described here were also used to derive the initial polarization model. Dimensional analysis was most importantly employed to obtain qualitative results regarding the electrostatics of electrospraying geometries, that are later compared with the experimental results of Mason. These results agree with those experimental results, which are further in agreement with assumptions made in the theoretical chapter. The fact that the results obtained numerically and theoretically agree with those observed, both theoretically and experimentally, by another researcher, is a good validation method of this work.

Chapter 5 | Results & discussion

When you study natural science and the miracles of creation, if you don't turn into a mystic you are not a natural scientist.
– Albert Hofmann, *LSD: The Geek's Wonder Drug?*

This chapter comprises three subsections, with the same order and naming as the prior three chapters. It starts with the theoretical approach of solving the problem of determining the polarization electric fields quantitatively. The numerical section introduces results similar to those in the theoretical section and compares them, while also introducing dimensional analysis results, motivating the given theoretical approach. Finally, this chapter is concluded with experimental results, serving a qualitative research motivator.

5.1 Theoretical work

This section comprises of multiple subsections, quickly summarised here. The first subsection discusses the droplet dielectric theory by using the normalised electric fields from the analytical model and the numerical results. Also, given that normalisation was done, the conformal transformation separation d was not discussed, as it does not influence these results. All the numerical results were generated using COMSOL Multiphysics, as discussed in Section 4.1.2.

The next section discusses this parameter and shows that scaling should rather be done using Mason theory. Hereafter, the model describing the liquid droplet is compared with models used by other authors, which also preferred employing ellipsoids to describe the cones of electrospraying, with their results being supported by other theoretical models and experimental studies. Finally, all these results are combined to introduce the corona field thresholds, which are compared with experimental results of other researchers. The analytical model is also compared with the numerical model obtained from dimensional analysis [70]. Also, the average relative percentage errors are 14.6 and 14.3% for the numerical and analytical models respectively, compared to experimental studies of other researchers (see Section 5.1.4) [10, 24, 40].

5.1.1 Droplet dielectric theory

The analytical model introduced in the theoretical section was compared with numerical results (see Figure 5.1 for the comparisons). The model simplifies to (3.3.4) and (3.3.7), and only depends on the applied potential V, the transformed separation d (also referred to as the conformal length), and the relative permittivity ϵ of the liquid. The model is given as

$$\mathbf{E}^{\perp}_{\mathbf{below}} = \frac{3V}{d^2(2\epsilon+1)} \quad \text{and} \quad \mathbf{E}^{\perp}_{\mathbf{above}} = \epsilon \mathbf{E}^{\perp}_{\mathbf{below}}. \tag{5.1.1}$$

For a thorough description on how this model was obtained, see Section 3.3 of the theoretical chapter. Only the perpendicular electric fields are of interest, as the parallel fields are not influenced by polarization (3.1.12).

The method of determining the conformal length d will be discussed in the next subsection. Given that all of these results are being normalised, the values used for it are arbitrarily chosen. When comparing the theoretical model with the numerical results, these trends are clearly similar, but it is also seen that the denominator ϵ-coefficient of the theoretical model is noticeably larger. By means of fitting the numerical outside electric fields using the function $f(x) = (a \cdot x)/(b \cdot x + 1)$, many conclusions were drawn. The magnitude of a is not of importance due to the normalisation, while b is the denominator ϵ-coefficient of these results. These normalised, numerical outside electric fields, are capillary radius dependent, as shown in Figure 5.2, imposing radius dependence on the denominator coefficients (being constant for the analytical model ($b = 2$)). These normalisations were done to understand the specific field characteristics.

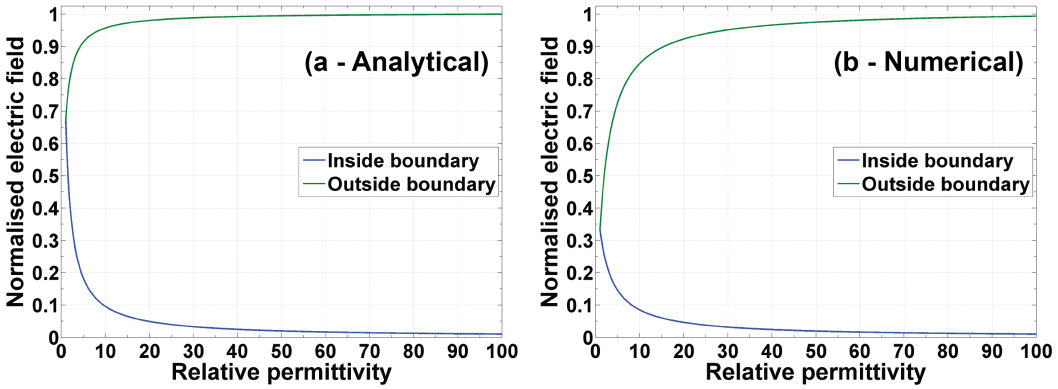

Figure 5.1: Normalised electric fields for the theoretical model inside the dielectric (3.3.4), and outside the dielectric (3.3.7), are shown in frame (a). These results are compared to the same fields when simulating this geometry numerically, such as shown in frame (b). These characteristics are clearly of a similar nature.

From the numerical results (see Figure 5.2) it appears as if the theoretical model is an upper-limit, as to what is obtainable numerically. By determining the denominator coefficients by means of fittings for a range of radii, it can be shown that there is a linear relationship, which can be accurately described by the function $b(R) = p1 \cdot R + p2$, where $p1 = 11229$ m^{-1} and $p2 = 0.1092$. The effect of changing the separation distance L does not influence the normalised electric fields. This is as expected, as changing the separation distance does not change the volume of the polarized liquid droplet [51]. Because, referring to the original depolarization factor for this geometry (3.3.2), it only depends on the parameters defining the curvature and geometry of the droplet.

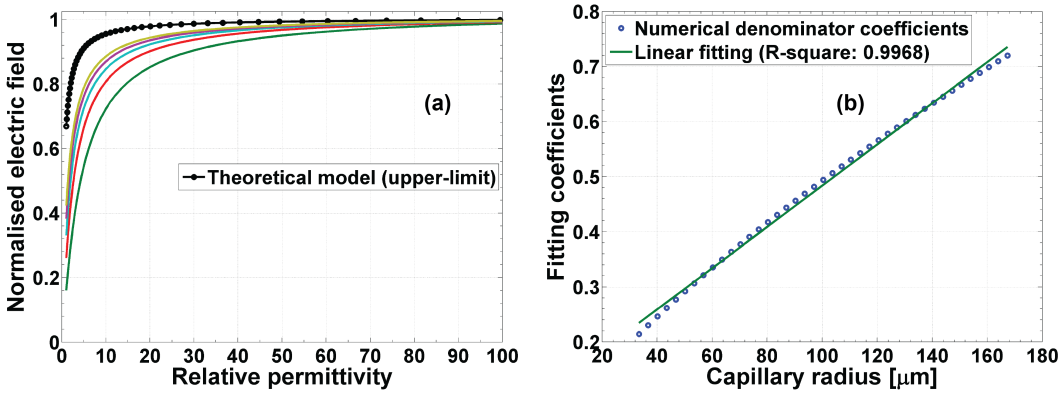

Figure 5.2: Normalised electric fields for the analytical model outside the dielectric, compared to electric fields calculated numerically for different radii, are shown here in frame (a). There is a linear relationship for these numerical denominator coefficients, such as shown in frame (b), as determined from these fittings. An adapted model is proposed in the next subsection to correct this disagreement.

The relative percentage errors for when using the function $b(R)$ to specify these denominator coefficients, compared to using the constant value of $b = 2$, are compared in Figure 5.3. The result of using an expression with a constant depolarization factor introduces a larger error when compared to numerical results, but such a model is analytical, which is based on certain assumptions. Introducing the numeric function to specify the depolarization factor reduces the error, but it also requires the extrapolation of a function derived from finite element results. Unless otherwise mentioned, the original analytical function with the constant denominator coefficient $(b = 2)$ will be applied. The use of an analytical expression is more tidy than that of introducing a numerically fitted function, as it is then possible to make general quantitative statements regarding the behaviour of such a model. On the next page, the ϵ-coefficient fitting is discussed, though it should be noted that it is generally not possible to correlate the numerical results, and an analytical model using a linear fitting.

The outside electric fields presented in Figure 5.1, are given separately in Figure 5.3 for easier comparison. The relative errors for the inside and outside fields were similar. When calculating these errors, the numerical results were assumed correct. Good agreement with the numerical results is seen. It is very fortunate that these trends are accurately describable with a linear fitting, as generally such correlations are non-linear and difficult, if not impossible, to fit.

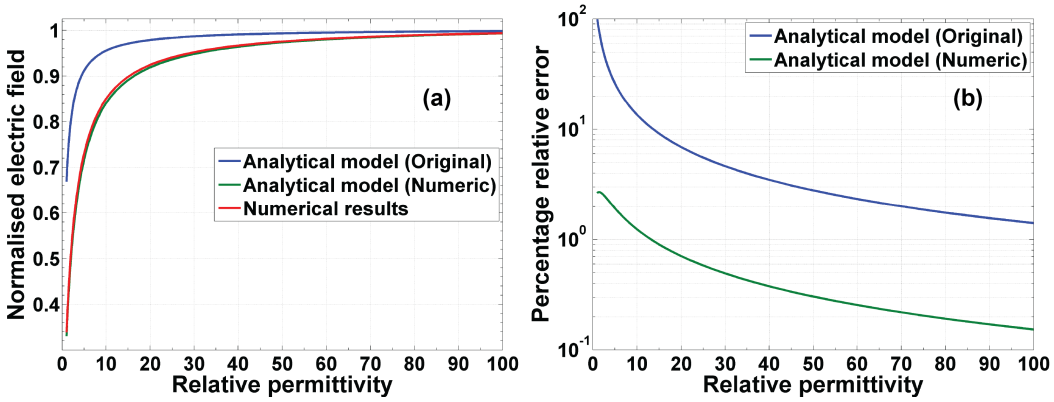

Figure 5.3: Normalised electric fields for these analytical models, compared to the numerical electric fields, outside the dielectric. The relative errors for these fields are the same. Also shown, frame (*b*) compares the errors of the original and corrected analytical models (using a logarithmic scale relative to the numerical results).

5.1.2 Adapted theoretical model

In (3.2.10), the transformed separation d was derived using Taylor expansions. Even though the proposed model produces the correct field characteristics, the magnitudes thereof are larger than the upper-limit enforced by the Mason equation from (3.1.4). An adapted model employing these characteristics is proposed. The asymptotic outside electric field

$$E_\infty = \lim_{\epsilon\to\infty} \frac{3V\epsilon}{d^2(2\epsilon+1)} = \frac{3V}{2d^2}, \tag{5.1.2}$$

is used here for normalising (5.1.1). Hereafter, scaling is accomplished by using the Mason equation E_τ (which is known to be the upper-limit)

$$E_M = \left(\frac{\mathbf{E}^{\perp}_{\mathbf{above}}}{E_\infty}\right) E_\tau = \left(\frac{2\epsilon}{2\epsilon+1}\right) E_\tau. \tag{5.1.3}$$

Employing the previously used assumption that the maximum fields E_M are given by the addition of the polarization E_P and the known Mason term , the polarization electric field is obtained by solving and substitution as [70]

$$E_M = E_P + E_\tau \;\Rightarrow\; E_P = \frac{-E_\tau}{2\epsilon+1}. \tag{5.1.4}$$

The maximum field E_M is an analogue to the field at the outside boundary $\mathbf{E}^{\perp}_{\mathbf{above}}$ in (3.3.7). Likewise, the Mason field E_τ is the analogue of the applied uniform field in (3.3.3). Note, given that the applied Mason field is inhomogeneous, the depolarization factors of these two models are not comparable. To calculate the depolarization field E_{DP}, it is required to use the effective field $E = E_M/\epsilon$, therefore obtaining that

$$E = E_{DP} + E_\tau \;\Rightarrow\; E_{DP} = \left(\frac{1-2\epsilon}{2\epsilon+1}\right) E_\tau. \tag{5.1.5}$$

Equation (5.1.4) is compared to the numerical results shown in Figure 5.4. Also shown are the results of using the numeric denominator coefficient. The proposed model is more accurate for the larger radii, suggesting that for larger droplets, the error associated with not taking the tip radius into consideration decreases accordingly. Thus, by including the radius in the depolarization factor decreases errors by more than an order of magnitude. The model proposed is also compared to the previously obtained numerical model [70] in Figure 5.4. The results show that these two models produce very similar polarization fields.

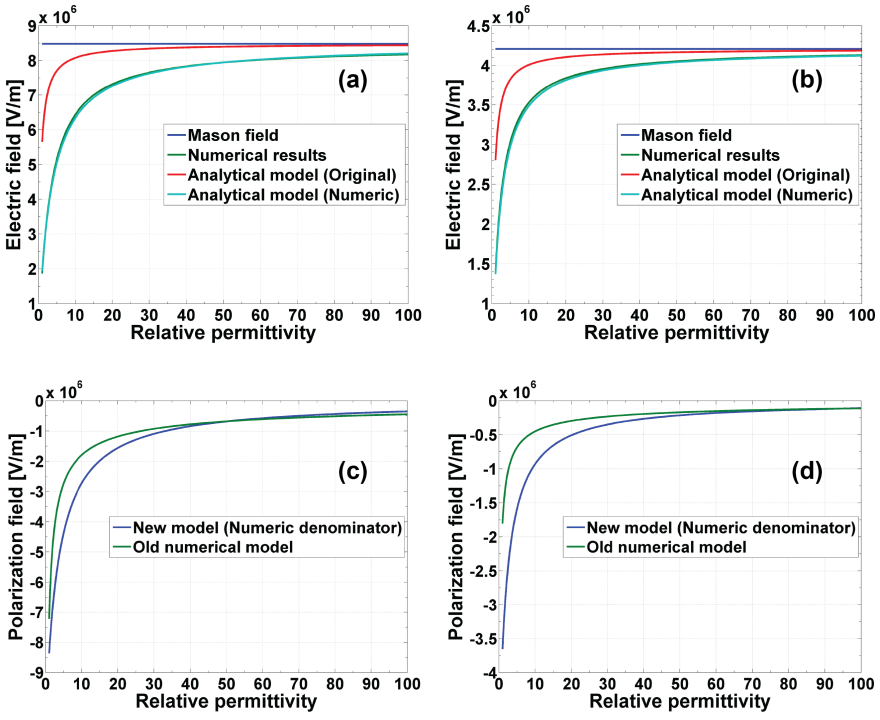

Figure 5.4: The electric fields obtained numerically, constant field from the Mason equation, originally proposed model, and the adapted numeric model, are compared in frames (a) and (b). Frames (c) and (d) show the polarization fields of the previous and the proposed model. Radius and separation distances of 50 μm and 500 μm, and 100 μm and 1000 μm, have been used for frames (a, c) and (b, d) respectively.

5.1.3 Liquid droplet description

The geometry used to describe the electrospraying process should be chosen wisely, as it will influence the maximum electrical fields considerably. However, it is also desired to use a geometry that is simple and well-studied by others, because known results should be comparable to any newly proposed models. Given that the hyperbolic point-to-plane geometry introduced by Mason (see Section 3.1.1) is well established and frequently used by the electrostatics community, it was decided to also use it in this research. The geometry of Mason was extended with the inclusion of a liquid volume at the capillary tip.

From electrospraying electrohydrodynamics, it is known that the rounded meniscus of a liquid drop at the tip of a capillary, deforms into a conical shape when the electric field is of a sufficient strength. The fundamental assumption made was that the liquid drop is static in this conical shape, as this is the shape of maximum field divergence, and what is experimentally observed just before the formation of the cone-jet. This assumption was suggested, as the maximum obtainable electric fields for a given geometry is of interest here. Such a conical shape can be described using hyperbolic functions (see Section 3.1.3), similar to those used in Mason electrostatic theory. Using such a geometry enforces a half-angle of $45\,^\circ$ with the cone-axis, in contrast with the $49.3\,^\circ$ angle defined by Taylor [86]. Several authors used this approach, as it is axisymmetric [25, 29]. Under this static assumption, zero applied hydrostatic pressure is implied, and the hysteresis phenomena associated with dynamically changing liquid surfaces due to changing electric fields is not applicable. This description, however, does not account for the effect of the liquid conductivity on the cone shape.

Such a geometry also rounds the tip of the cone, which, although it reduces the electric fields, it prevents mesh discontinuities when solving these problems numerically. See Figure 5.8 for example on how such a configuration relates the radius of curvature, with the tip of these hyperbolic functions. Several authors used ellipsoids to describe the cones of electrospraying, with their results being supported by other theoretical models and experimental studies [3, 24, 30, 40].

The results presented in this subsection, is based on the analytically derivations of Section 3.2.1. There a conformal mapping was used to incorporate the liquid droplet to account for the polarization. In order to verify whether these mappings are appropiate to study this problem, the electric field calculated by means of the transformed geometry, is compared to that of the known Mason equation in Figure 3.17. Those curves indicate that the characteristics of these two geometries are the same. The fact that these characteristics are the same is invaluable, as the transformed geometry was then studied analytically, and then at a later stage, these results were applied to the original geometry.

Although this conformal mapping employed a parabolic geometry, scaling at a later stage was accomplished with the Mason equation, which is based on a hyperbolic geometry. Therefore, as the field characteristics of these geometries are the same, it is in order to employ an asymptotic analysis as in Section 5.1.2.

5.1.4 Corona threshold model

By employing the Rousse model [34], as discussed in Section 2.2.1, the corona thresholds are calculated, taking the particular geometry and relative permittivities into consideration. This specific model was chosen, as it is consistent with both theoretical and experimental data. Assuming that the Rousse model produces the onset field of an empty capillary, the corona thresholds are given, when using (5.1.5) in the current context, by

$$E_C = E_O(R) - E_P(V, L, R, \varepsilon) + \chi(p, \phi, T), \tag{5.1.6}$$

where E_O is the corona onset threshold of metal for the given geometry, and E_P the polarization field. The function χ is introduced to account for environmental factors (pressure p, humidity ϕ and temperature T), which should be determined empirically, otherwise it should be taken as zero, leading to

$$E_C = \left(\frac{2\epsilon + 1}{2\epsilon}\right) E_O. \tag{5.1.7}$$

The proposed model suggests that the corona thresholds occur at different electric fields for similar geometries. Therefore, the electric fields E_C measured are indeed lower with an increase in permittivity, but the field at which onset actually occurs, stays constant for the given geometry. The effective onset fields for all the geometries correspond to that of metals. As the permittivity increases, so does the secondary field which is created due to the polarization of the given liquid. When corona discharge occurs, the effective field at the liquid surface is the same as that of metals using the Rousse model.

The field the liquid experiences is, however, lower, because a lower applied potential results in a lower applied field at the capillary tip. The field required to initiate the liquid surface instability is still as predicted by (2.1.2). The proposed model suggests that liquid electrospraying is mainly limited by radius, relative permittivities, and the liquid surface tension. Previously, the surface tension was regarded as the primary limitation [10, 24], but it just so happened that the relative permittivity of water is also as large as its surface tension, compared to other liquids. However, there is generally no specific relationship between the relative permittivities and surface tensions of liquids.

The corona threshold electric fields according to (5.1.7) for various radii and relative permittivities are shown in Figure 5.5, using a separation-radius ratio of $\alpha = 10$ for the Rousse model, and the two proposed models. In the same figure, the influences the proposed model have on which liquids can be electrosprayed are shown. The solid lines indicate the critical electric fields required for electrospraying according to (2.1.2). The points that correspond to the individual colours of the critical fields are the corona thresholds of various liquids of different relative permittivities.

From this figure it can then be seen that a decrease in capillary radius will enable more liquids to be electrosprayed. This is the result of the rate at which the thresholds increase, to be greater than the radii pre-factor (see (5.1.8)). For capillaries of smaller radii, it will therefore be possible to electrospray a larger variety of liquids. The maximum surface tension of liquids to be electrosprayed can be determined analytically, by using the capillary pressure equal to electric traction

$$\gamma_C = \frac{R\varepsilon_0}{4} E_C^2, \quad \text{suggesting} \quad \gamma_C \sim R^{-0.5}. \tag{5.1.8}$$

When Borra *et al.* [40] defined the electric dripping mode, it was found that smaller capillary radii enables a more stable electrospraying. This observation is thus in agreement with the above proportionality relation. From Figure 5.6 it can be seen that most of the experimental data points at which these onsets occurred, are higher than predicted with the proposed models. This suggests that these models will experimentally ensure electrospraying stability. Further, these models agree accurately with experimental data of three research groups, although it only uses an elementary corona point-to-plane model as basis.

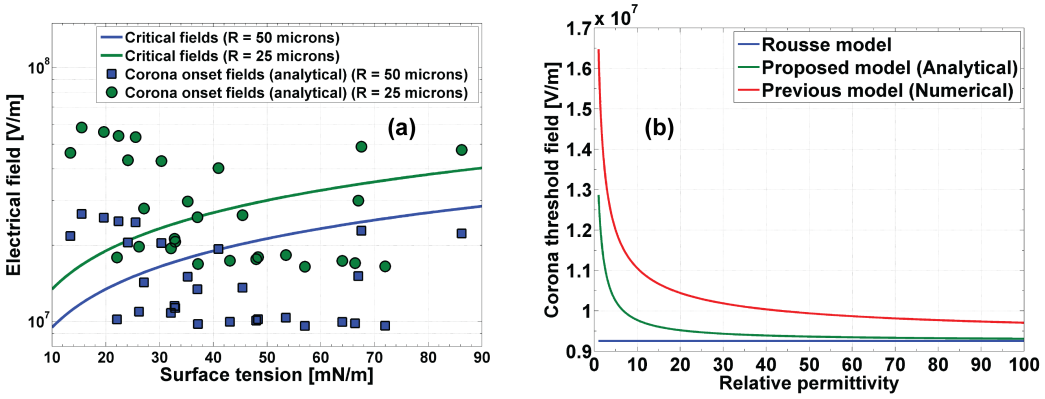

Figure 5.5: In frame (*a*), the critical electric fields (2.1.3) required for electrospraying (solid curves) are compared to the corona thresholds of various liquids (circular and rectangular markers) with different relative permittivities. Note, from this frame it can then be seen that a decrease in capillary radius will enable more liquids to be electrosprayed. The corona discharge thresholds for the proposed model, compared with the previously derived numerical model [70], are shown here in frame (*b*). These curves are for the radius and separation distances of 50 μm and 500 μm respectively. It can be seen that these two models compare well with each other in a certain sense. Also shown here is the constant, polarization independent, Rousse thresholds E_0.

These two models, the numerical and analytical derived corona thresholds, are compared to the experimental results of three different papers [10, 24, 40]. In the experimental configuration of Smith, a stainless steel needle was used, which was both ground down and polished flat [10]. This needle was positioned 25 mm above the grounded electrode, with an outer radius of 275 μm. Here, only the ethylene glycol measurement was used, as this is the only measurement of which it is certain that a discharge occurred, and of which all of the properties are known. Buraev and Vereshchagin used a capillary with a radius of 450 μm, which was positioned 39 mm from the grounded plane [24]. Their paper contains both the electric field values at which the discharges occurred, as well as the relative permittivities of the liquids, as they measured it during the experiments. Borra *et al.* used five different nozzle diameters (1.1, 0.9, 0.8, 0.6, 0.5 mm) for their experiments [40]. From the data tabulated, the capillary radius is not mentioned, although it is mentioned that it was positioned 40 mm above the grounded plane. The electric fields at which the discharges occurred for their work, a capillary radius of 400 μm was assumed (average of the radii). The voltages where discharges occurred are tabulated, from which the electric fields at the tip were calculated using the known geometrical parameters.

See Figures 5.6 and 5.7 for a comparison of the models, both the numerical and analytical derived corona thresholds, to the experimental results. Table 5.1 contains the details regarding the values calculated and the associated errors.

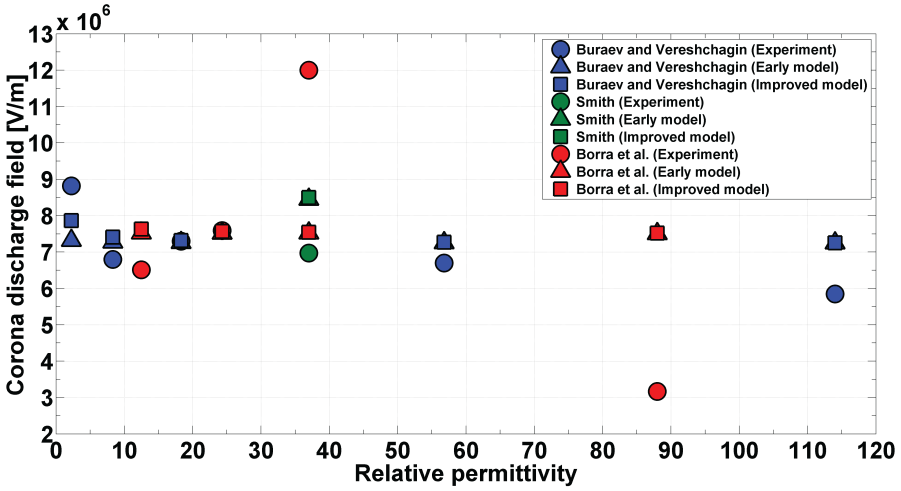

Figure 5.6: The corona onset thresholds of various researchers, compared to those thresholds obtained by using the currently proposed polarization field model together with the Rousse corona onset model. When required, the electrospraying equations were used to calculate these thresholds from given data. Also shown, are the results of when using the old model derived from numerical results and dimensional analysis. *Improved model* refers here to the analytical derivation, as per (5.1.7), whereas *early model* refers to the model introduced in the numerical section, as per (5.2.4).

The average relative percentage errors are 14.6 and 14.3 % for the numerical and analytical models respectively. For these calculations, the water entry of Borra *et al.* was considered to be an outlier (the only error that is larger than approximately 40%), and the experimental results were assumed correct.

Table 5.1: The percentage relative errors of each of the two models, where Error1 and Error2 represent the numerical and analytical models respectively. Further, only for the water entry of Borra *et al.* the error is larger than approximately 40%.

Liquid	**Relative permittivity**	**Error1 (%)**	**Error2 (%)**
Buraev and Vereshchagin (1972)			
Toluene	2.25	17.1	0.36
Dibutyl Phthalate	8.3	9.58	12.9
Isopropyl alcohol	18.3	0.55	1.93
Ethylene glycol	56.8	8.22	9.05
Water	114	23.9	24.3
Smith (1982)			
Ethylene glycol	37	21.1	22.5
Borra *et al.* (1998)			
Hexane	12.5	15.5	19.8
Ethanol	24.3	0.99	0.85
Ethylene glycol	37	37.3	36.7
Water	88	136.7	137.9

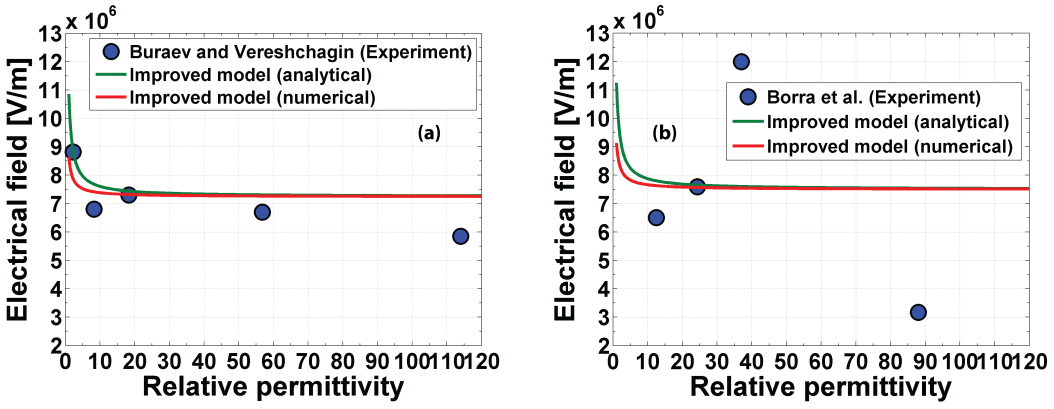

Figure 5.7: The corona onset threshold curves of Buraev and Vereshchagin, shown in frame (*a*), and Borra *et al.*, shown here in frame (*b*), compared their experimental measurements. *Improved model (analytical)* refers here to the analytical derivation, as per (5.1.7), whereas *improved model (numerical)* refers to the same model, but with the numerical correction *b*. These are sub-figures of Figure 5.6, which compares the data of all of the researchers. For large values, these models are closely related.

5.2 Numerical analysis

All numerical results were generated with COMSOL Multiphysics [60], using MATLAB for the dimensional analysis (source code given in the appendixes). For previous work [70], the geometry was similar to the description in (4.1.4) of this thesis. That paper further focused on the theory associated with corona discharges and the application of those models derived. This section uses large parts of that paper exactly, although the required permissions were obtained from the IEEE for reuse [70]. The last section discusses qualitative results that where obtained using nondimensional basis variables defined in Section 4.2.

5.2.1 Previous dimensional analysis

Electrospraying geometries were studied numerically using finite element analysis (FEA) by using COMSOL Multiphysics [60]. The capillary was modelled using a revolving hyperbola with a parametrization as described by (4.1.4) of this thesis. The parameters investigated were the radius, separation distance, parametric bounds, and the mesh quality statistics. The maximum electric fields were calculated using domain node points. These results were compared to the numerical results of another group. It compared well and showed the same characteristics as work by Velásquez-García [15].

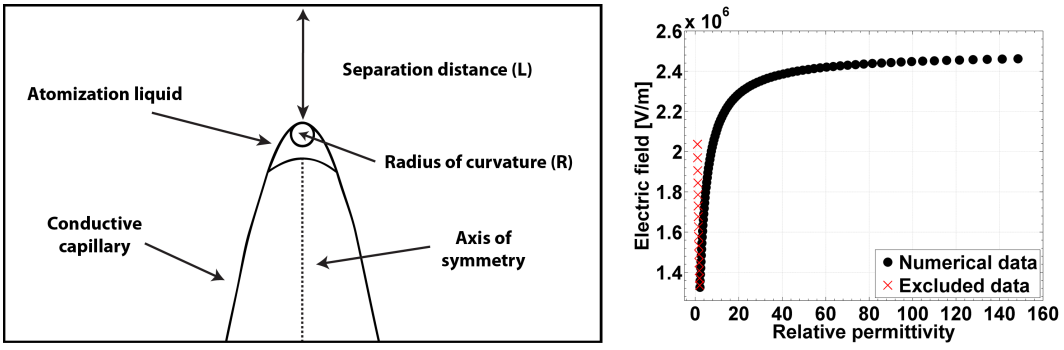

Figure 5.8: The cut-off geometry as used during the finite element analysis (FEA) simulations and an example of the results obtained. This figure shows the electric fields versus relative permittivities. The red crossed points were excluded, as they do not form part of a power trend, being dependent on the hyperbolic eccentricity.

The FEA geometry was adapted to include the liquids to be electrosprayed, hence being able to study how polarization affects the electric fields observed at the tip. All liquids being used for electrospraying will get polarized due to the applied electric field, as all of them are dielectrics. For these simulations, uniform equidistant α-ratios ($\alpha = L/R$) between 10 and 100 (step-size of 1) were studied, ranging over the relative permittivities, using the function

$$\varepsilon_i \in \{\exp(i \cdot 0.05) \,|\, i = 0, 1, \ldots, 100\}. \tag{5.2.1}$$

The main goal was to predict these polarization affected fields analytically. It is clear that for $\varepsilon = \infty$ the maximum electric fields are equal to that of a conductive ($\varepsilon = 1$) capillary. This eases the curve fitting process, as a power function can be fitted given that the intercepts are already known. For fitting purposes, certain points were excluded, as they do not form part of the power function. These points are mainly dependent on the geometrical hyperbolic eccentricity used. It is assumed that the global maximum electric field E_M is given by the sum of a polarization E_P and the known Mason term E_τ (3.1.4)

$$E_M = E_P + E_\tau. \tag{5.2.2}$$

Given that both the maximum and Mason fields are known, from numerical results and the analytical equation respectively, it is possible to determine the electric polarization field by means of dimensional analysis as

$$E_P = E_M - E_\tau \Rightarrow E_T = E_P \left(\alpha^A R^B V^{-1}\right). \tag{5.2.3}$$

The transformation term (E_T) is used to analyse the data, being reverted back to the given polarization term by means of an inverse transformation. These parameters (A, B) were chosen due to their appearance in the Mason equation. The exponent of the potential V was easily determined due its linear nature. Iterating over the remaining exponents, it was found that $A = 1$ and $B = 2$ delivered the most accurate results, with $A = 0$ and $B = 4$ presenting reasonable results in the upper α-ratio limit (large separation-radius ratio).

From the numerical results and the Mason equation, it can be seen that with similar separation-radius α-ratios, but different radii, the effective electric field will not be comparable. Therefore, five different radii were used to produce similar α-ratios and then transforming the polarization terms. These results indicated that the change in consecutive fields is inversely proportional to their radius, prompting the calculation of an average of these fields and then fitting a power function to it (see Figure 5.9(a)). Comparison with the numerical results were done to find the optimal exponents, with optimization around $\varepsilon = 5$, as statistics showed the mode of relative permittivities of common materials to be given there (see Figure 5.9(b)). Using these optimization exponents ($A = 1$, $B = 2$), the polarization electric fields can be calculated using

$$E_P\left(V, L, R, \varepsilon\right) = \frac{V E_T}{LR} = \frac{V}{LR}\ \beta_1 \varepsilon^{\beta_2}, \tag{5.2.4}$$

where $\beta_1 = -1.8047 \times 10^{-4}$ m and $\beta_2 = -\frac{625}{1037}$ are empirical fitting constants, the other parameters already being defined. However, it is required for E_T to have a dimension of length in a parameter other than those currently defined geometrically. It is also possible to have a dimension of volume for $A = 0$ and $B = 4$, as it seems plausible that such a parameter could relate to the liquid volume when consulting polarization theory, but it is beyond the current scope to solve this analytically [59].

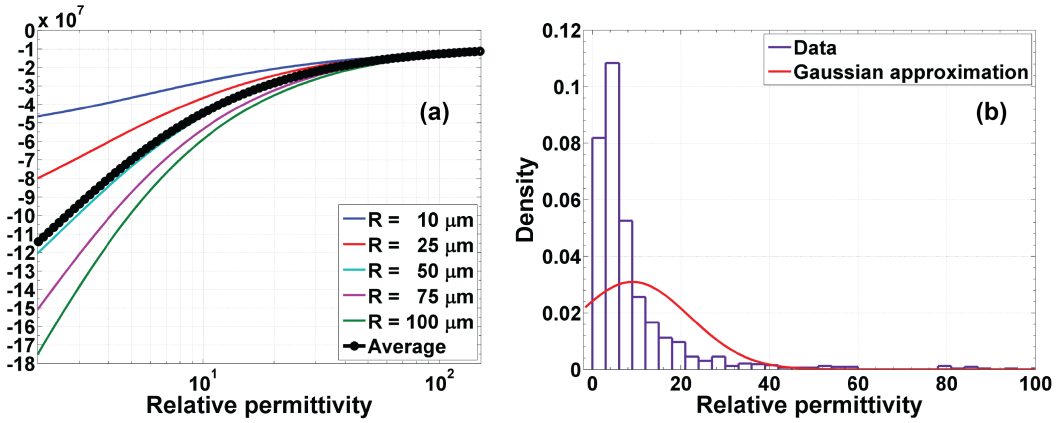

Figure 5.9: The transformed polarization fields of dimensional analysis for different radii ($A = 1$, $B = 2$), and the average fitted function are shown in frame (a). Frame (b) shows relative permittivity statistics for common organic liquids ($n = 1104$) [87]. Statistics of these liquids showed the mode of relative permittivities of common materials to be given at approximately $\varepsilon = 5$, which was used for optimization. Note that this is the average of these liquids, and that it is not representative of all liquids, and that there are surely outliers, such as for example formamide and water.

For small radii this equation has accuracies of 73 and 5.2% in the lower and upper α-ratio limits respectively, and for medium radii 3.1 and 12% in these same limits. Note that for all radii the α-ratio limits, a larger separation-radius ratio, delivered reasonable results. Figure 5.10 compares the proposed model with the numerical results, while also showing the relative percentage error.

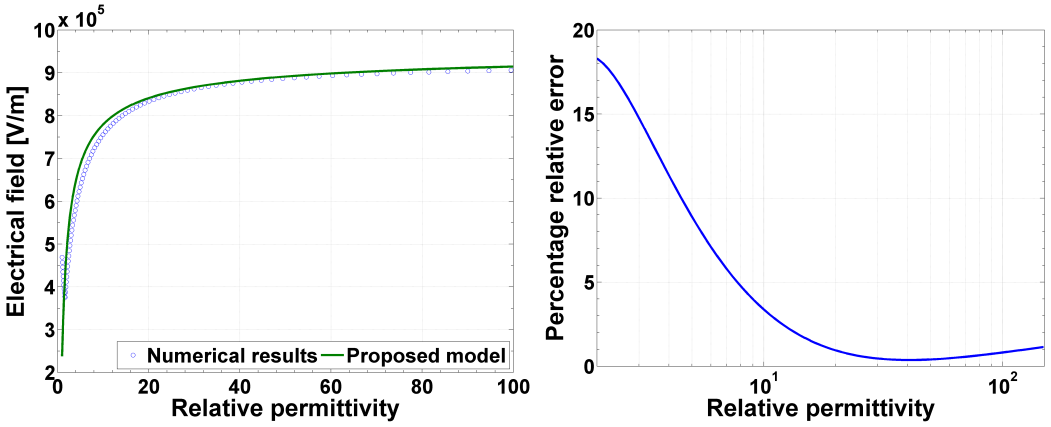

Figure 5.10: Percentage relative errors for the upper α-ratios (around $\alpha = 100$), showing good agreement between these results and the proposed model. For these calculations, the numerical results were assumed correct, relative to (5.2.4).

5.2.2 Nondimensional basis variables

The nondimensional basis variables generated by using (4.2.4) are qualitatively discussed in this section, in order to support results from the preceding section. For this purpose, two datasets were generated using COMSOL Multiphysics. The first was for using a constant capillary radius ($\sim 100\ \mu$m), while changing the capillary to electrode separation distance L. The second set used a dynamic separation distance ($L = 10R$), while changing the capillary radius.

These two geometrical parameters, the capillary radius and the separation distance, were chosen as they are the only two directly dependant parameters of the problem. By changing them, the liquid droplet length S_1, the liquid droplet surface area S_2, and the liquid droplet volume S_3, will change accordingly, as these quantities are directly dependant on the capillary radius.

Some of the nondimensional basis variables proved not to be as useful when plotting, see for example frames (a, b) given in Figure 5.11. These two are the graphs of the liquid droplet surface area Π_5 and the liquid droplet volume Π_6 variables, for different radii and a constant separation distance. For all of the nondimensional variables the relative permittivity was the dependant variable.

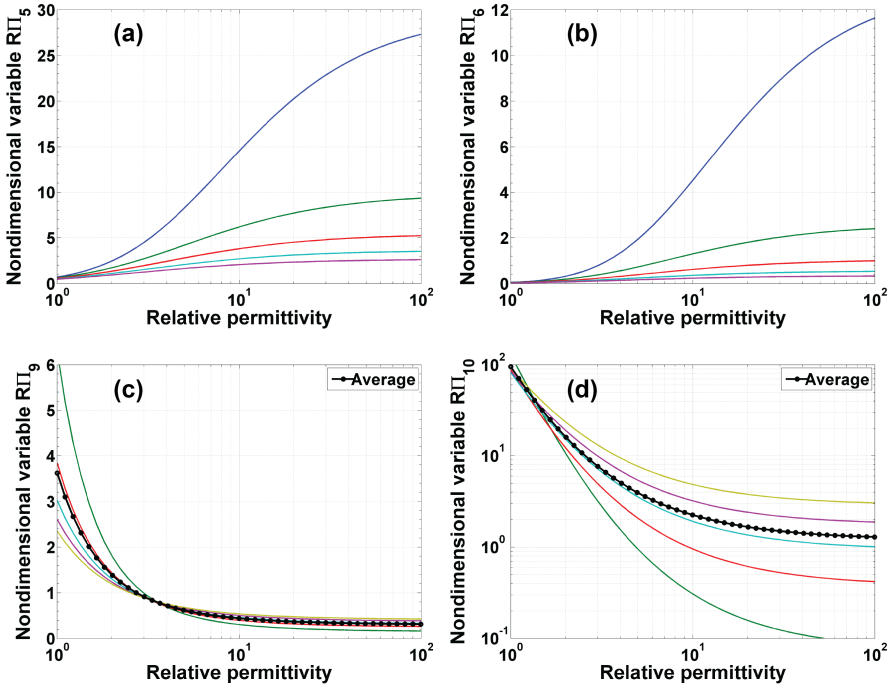

Figure 5.11: Less useful nondimensional basis variables, the liquid droplet surface area Π_5, and the liquid droplet volume Π_6 variables, shown in frames (a) and (b) respectively, for different radii and a constant separation distance. Frames (c) and (d) are nondimensional variables constructed from the original basis. Frame (c) is the initial and final field dependences $\Pi_9 = \Pi_7 \cdot \Pi_8$, and the volume dependences $\Pi_{10} = \Pi_8/\Pi_6$ variable are being shown in frame (d).

The case for keeping the capillary radius constant, while changing the separation distance delivers results that supports the previously made statement that the depolarization factors are only dependant on capillary radii. From the nondimensional separation variable $L\Pi_2$, see Figure 5.12(a), it can be seen that for different separation distances, the field characteristics are similar. These variables also increase with separation distance, which is in agreement with Mason, who observed that the average electric field $E_{av} = V/L$ decreases with an increase in separation [51], as they are just the inverse of one another.

$$\therefore \Pi_2 = EL/V = E/E_{av}. \tag{5.2.5}$$

The two most interesting variables are the initial $L\Pi_7$ and final $L\Pi_8$ field dependence variables, shown here in Figure 5.12(c) and (d) respectively. These variables indicate when nondimensionalising using only the relative permittivity dependant electric field E, with the initial E_0 and final E_F of that field, these variables are exactly the same for different separation distances. This is a very clear observation that the depolarization factors are not dependant on these separation distances, because these nondimensional variables are exactly the same (compared for example to the case of $L\Pi_2$).

Further, the results obtainable for dynamic separation distances were also studied (thus constant in ratio relative to the different capillary radii). From the nondimensional separation variable $R\Pi_3$, Figure 5.12(b), it can be seen that for different radii the field characteristics are similar and closely overlapping, such as shown by the average function for these curves. This is also in agreement with Mason, who observed that the average field E_{av} does not strongly depend on the capillary radius [51].

As for the case of a constant radius while changing the separation length, the initial $R\Pi_7$ and final $R\Pi_8$ field dependence variables, given in Figure 5.12(e) and (f) respectively, also contain invaluable information. For this initial field dependence variable $R\Pi_7$, a close agreement between these curves are seen at low relative permittivities, and for the final field dependence variable, a close agreement is seen at high relative permittivities.

Taking the product of these two variables $\Pi_9 = \Pi_7 \cdot \Pi_8$, see Figure 5.11($c$), results in curves of similar characteristics and overlapping. Though expected, this shows that the initial and final fields enforces agreement where they have the strongest influences. More importantly, this is an indicator of the direct dependence of the depolarization factors on capillary radii. The product Π_9 shows that when these two finals are known, it is possible to predict the intermediate fields. The final field is known from the Mason equation, but there is no simple way of determining the initial field. Further, see Appendix A.1 for the MATLAB code used to analyse the raw COMSOL Multiphysics data.

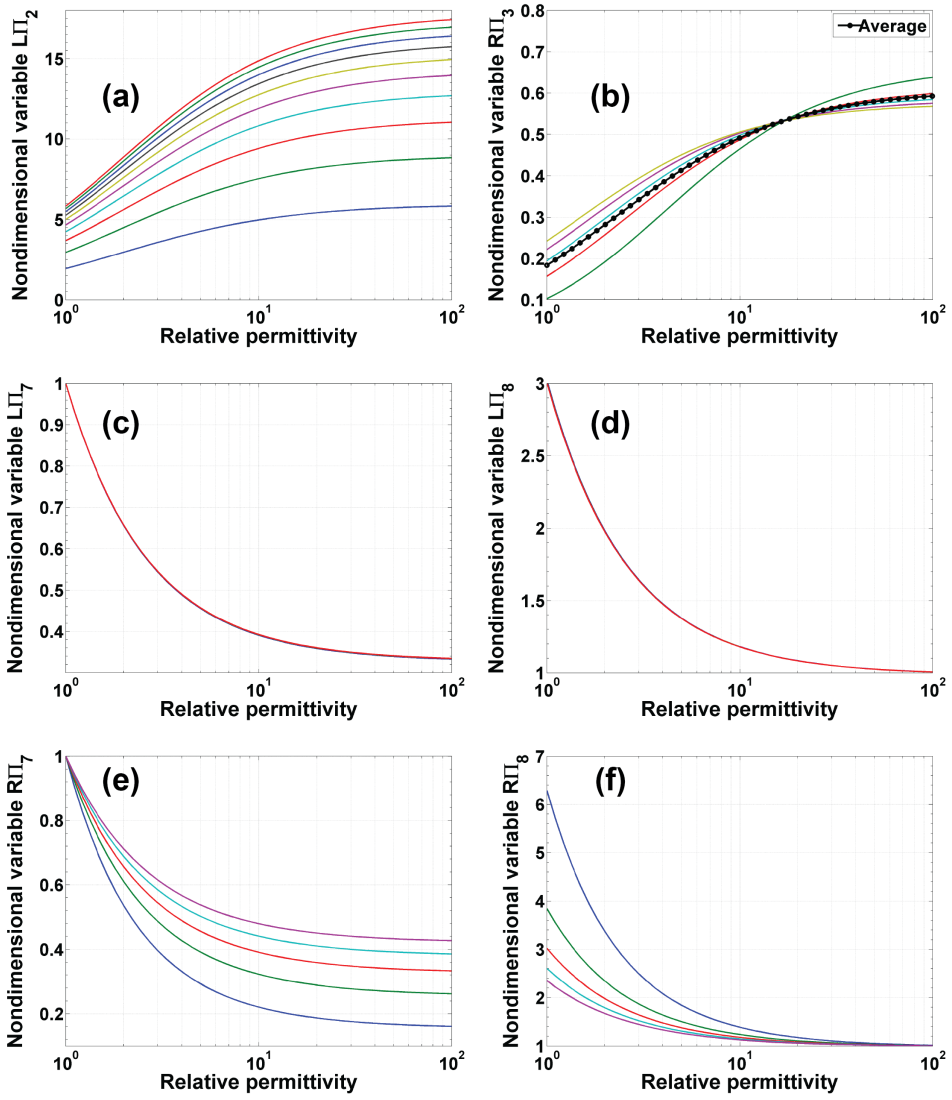

Figure 5.12: Frames (a) and (b) are the nondimensional separation and radius variables, keeping the radius constant and separation distance dynamic respectively. Each of these graphs agree with observations made by Mason [51], as these variables are proportional to the average electric fields of such point-to-plane geometries. The initial Π_7 and final Π_8 field dependence variables, shown in frames (c) and (d), are for the case of constant radius. These figures show the dependence of the depolarization factors on the capillary radii, and that they are not affected by the separation distances. In contrast, frames (e) and (f), are for dynamic separation distances.

5.3 Experimental work

The experimental components only made a motivational contribution to this thesis. These experiments were only carried out in order to obtain qualitative results regarding the corona discharges associated with electrospraying of high surface tension liquids. The experience obtained herewithin, will be employed to design the newly proposed surface tension measurement method.

5.3.1 Setup and procedure

An aluminium housing was mounted on a motorised stage to keep the borosilicate capillaries in place during the experiments. Two different sets of capillaries of 1 and 4 μm inner diameters were used, being manufactured by Proxeon (ES380) and Waters (ZLC-NFBS) respectively [55]. An Ortec 456 HV Power Supply was used to provide stable voltage. A Kyowa 2D-2P Stereo Optical Microscope was used to analyse the precipitations directly after each deposition. Stainless steel plates were used as collecting counter-electrodes.

The potassium chloride solutions were prepared according to the published work of Yamada *et al* [88]. For all the experiments a 5% weight concentration of potassium chloride was dissolved in distilled water, with the electrode being separated 1 mm from the capillary tip. The voltage was set constant at 1000 V for most of the measurements. The charged ion currents were measured using an HP 4140B Picoammeter interfaced to a computer. Imaging of precipitations and the analysis of these phase compositions were achieved using a Zeiss EVO MA15 scanning electron microscope (SEM). Depositions were identified with secondary electron images, and quantified using EDS analysis using an Oxford Instruments X-Max 20 mm^2 detector.

5.3.2 Results and discussion

As mentioned previously, this experiment was performed to obtain qualitative results regarding electrospraying and the corona discharges associated with high surface tension liquids. Given that most authors use the results of Smith as a rule of thumb for the surface tension upper-limit [10], it was decided to perform a series of measurements for higher surface tension liquids and analyse the results. For all the experiments a 5% weight concentration of potassium chloride was dissolved in distilled water, in order to obtain a solution of both very high surface tension ($\sim$ 73 mN/m) and high conductivity ($\sim$ 7.2 S/m)[88].

The depositions using the Proxeon capillaries were performed under atmospheric conditions, with applied voltages between 1200 and 2200 V. As no current measurements were made, it is not possible to make any statements regarding these results. It is speculated that electric-dripping is responsible for these depositions, as significant amounts of potassium chloride was detected.

Although subsequent experiments involved also measuring the charged ion currents, there is still insufficient information to make substantial statements regarding the electrospraying modes. The results of using a Waters capillary, with a similar configuration as to the Proxeon experiments, are given in Figure 5.13. To make confident statements, it would be required to image the tip online, while also measuring the particle size distributions.

It is challenging to compare the obtained results with those found in the literature, because generally average current-voltage characteristics are given, and not current-time characteristics as here[30, 40]. Qualitatively, these results are still compared to those from Borra *et al.* of 1999 and 2004. If this is indeed the electric-dripping mode that was observed here, it is comparable to those results of Borra *et al.* for capillaries of much larger radii [30]. They reported on average currents between 1 and 1.8 μA. It is believed that the spikes observed in the presented results are due to impulse currents from gas ionization, although the very low impulse frequency thereof is not understood.

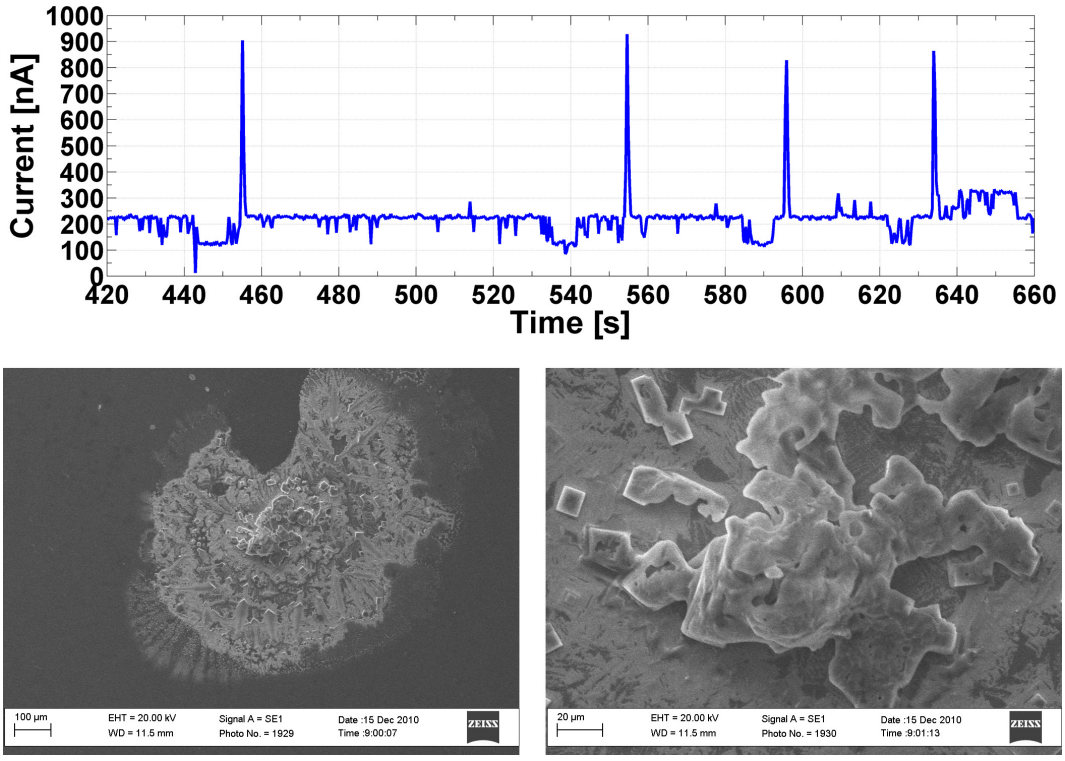

Figure 5.13: The current versus time characteristics (above), with the depositions generated using a Waters ZLC-NFBS capillary on a stainless-steel electrode (below). These SEM images also have accompanying EDS results given in Table 5.2.

The energy-dispersive X-ray spectroscopy (EDS) results given in Table 5.2 also indicate that these depositions are potassium chloride. Also, the enlarged scanning electron microscope (SEM) images indicate the crystalline structure of potassium chloride, with no visible damage due to electric discharges.

Table 5.2: Weight percentages (totalling 100) for each of the capillary depositions. These quantifications were done using SEM-EDS analysis, with a Oxford Instruments X-Max 20 mm^2 detector and the Oxford INCA software.

Proxeon capillaries										
	C	O	Na	Si	Cl	K	Cr	Mn	Fe	Ni
Surface	1.0	0.0	0.0	0.7	0.0	0.0	15.3	0.7	73.3	9.0
Precipitations	4.9	0.3	2.8	0.6	0.4	0.2	14.3	0.4	67.6	8.5
Solid crystals	8.2	1.4	3.6	0.6	0.4	0.2	13.1	0.5	64.1	7.8
Waters capillaries										
Precipitations	0.0	0.0	0.0	0.0	37.5	33.2	3.4	0.0	23.7	2.2

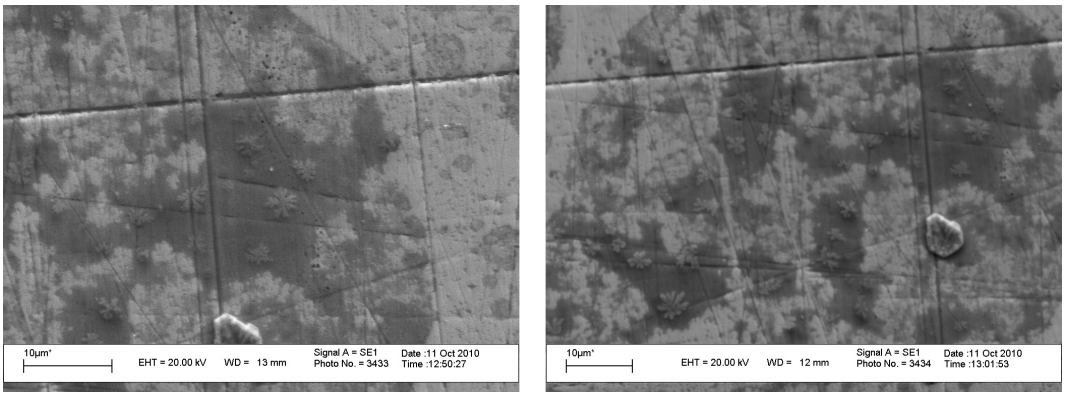

Figure 5.14: The patterns generated using a Proxeon ES380 capillary on a stainless-steel collecting ground electrode. These scanning electron microscope (SEM) images also have accompanying energy-dispersive X-ray spectroscopy (EDS) results given in Table 5.2. These depositions are non-uniform, but they have been circularly formed. Note also the larger, embossed solid crystals in this region.

The images in Figure 5.15 are given only for interest sake. Frames (*a*) and (*b*) indicate the potassium chloride crystals before being dissolved in the water, compared to the deposition on the collecting electrode. Frames (*c*) and (*d*) indicate the physical damage to the electrode by a complete discharge, after depositioning occurred. These EDS results confirmed that the crystalline structures are indeed potassium chloride. The bottom row of images indicate the physical damage of an electric discharge when no depositioning occurred.

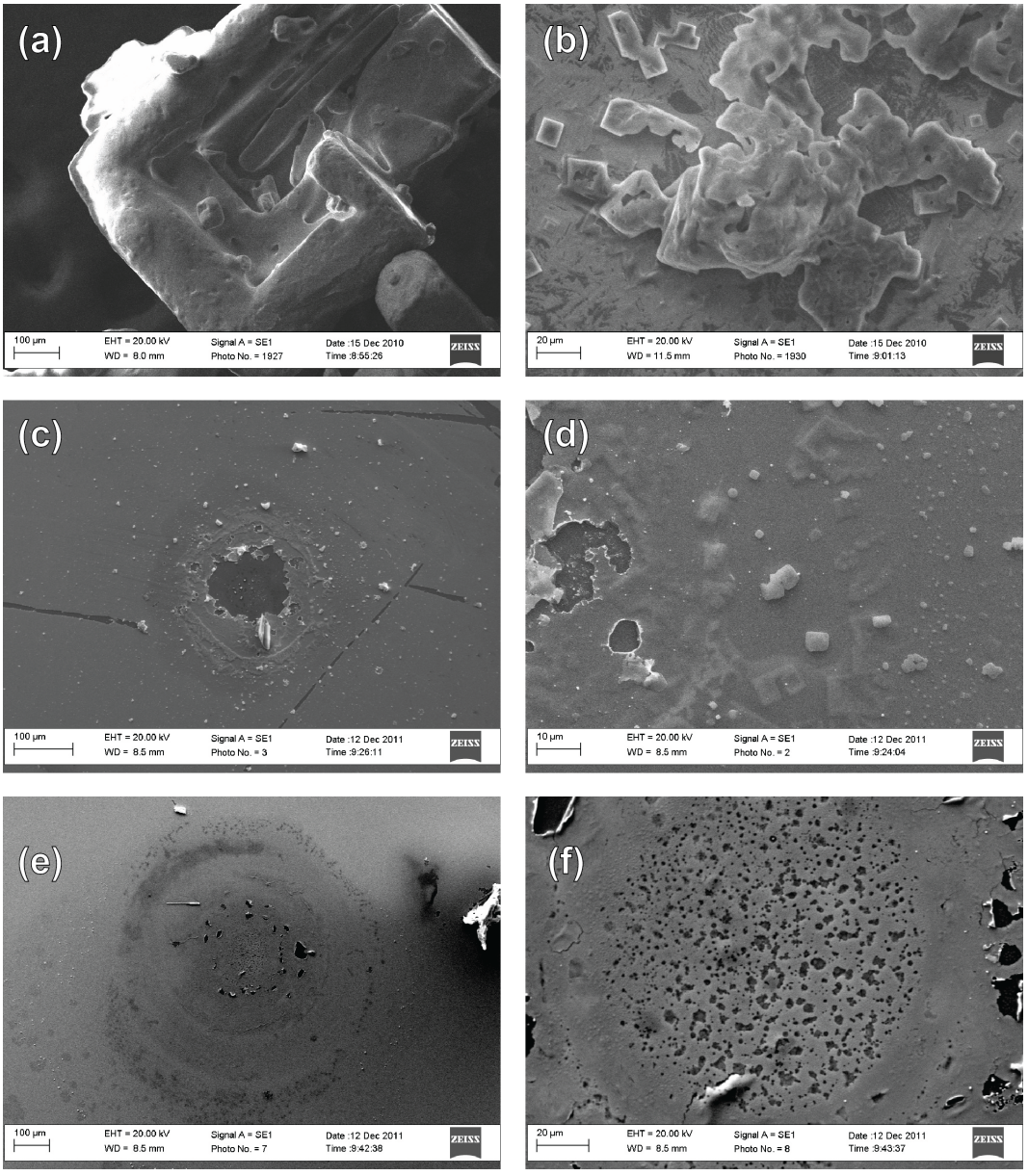

Figure 5.15: Crystalline structure of potassium chloride before and after depositioning, and the physical damage due to electric discharges.

5.4 Applications and chapter summary

This chapter is concluded by summarising the applications mentioned throughout this thesis, mentioning how such applications were realised by the presented research. Following that, these results are also individually summarised, mentioning the shortcomings thereof and potential improvements.

5.4.1 Summary of the applications

A new method to determine surface tension by employing electrospraying is described theoretically. Unlike the most other methods, which are restricted to certain liquids, it is possible to use this proposed method for the majority of liquids. The unique feature of this method is its ability to do measurements at arbitrary temperatures. It should be emphasised, this is a theoretical proposal to measure the surface tension. Multiple additional challenges will arise when an experimental prototype is built. One of these, which most experimentalists might consider as a fundamental weakness, is the fact that the reproducibility of Taylor-cone formation at the conditions as predicted by (2.1.2) is difficult. A solution to this problem is suggested by the fact that the cone formation times are understood from this research. By being able to determine these times, it is possible to in a statistical manner determine these onset voltages correctly, by repeating the measurement a large number of times. In an attempt to improve the reproducibility of these cones, an approach might be to utilise a sheath of nebulizing gas to aid in the droplet formation and stabilize the electrospraying process (see [89] for results on using this concept for high-frequency alternating electrospraying). Furthermore, to improve the accuracy even further, Bayesian statistics can be applied when the number of measurements are limited [90].

In addition to this technique for measuring surface tension, the calculation of these corona discharge thresholds have various applications. For example, the dynamics of electrostatic ion thrusters are much better described, the fine powder production by means of electrospraying can be optimised, and pattern generation using pulsed electrospraying cone-jets can also be optimised.

Each of the above applications described have been done so theoretically. This will concern experimentalists, which in some sense could be regarded as a valid concern indeed. However, nevertheless, these are still novel approaches described here for the first time. Vast amounts of follow-up research could be conducted, but the most important aspect, is that of calculating these corona discharge thresholds more modernly. As known from Section 5.1.4, even when using the relatively classical Rousse model, in conjunction with the proposed polarization models, the results are still accurate. These were the first models proposed in the literature for the calculation of point-to-plane electrospraying corona thresholds, and should serve as a starting point and or basis of future work, for the intimacy of electrospraying discharges and polarization effects.

5.4.2 Chapter summary and contributions

In the theoretical subsection of this chapter, one of the primary contributions is the analysis of the transformed separation d. It was shown that by using the domain uniformisation approach, the polarization affected electric fields are of the correct characteristics, but that the asymptotic field behaviour thereof is not correct. This problem was corrected by first normalising, and then scaling these results using the known Mason equation. Another improvement to this analytically derived model was the addition of a numerical fitted function $b(R)$ to describe the denominator ϵ-coefficient of these results. It is very fortunate that these trends are accurately describable with a linear fitting.

Another fundamental contribution to the theoretical component was the description of a corona threshold field model. By assuming that the maximum electric fields are affected by the polarization of the liquids to be electrosprayed, a simple polarization dependent corona threshold model is proposed. Both the analytical model to calculate these polarization fields, and a previous numerical model, were studied. The average relative percentage errors are 14.6 and 14.3% for the numerical and analytical models respectively, compared to experimental studies of other researchers.

In the numerical subsection of this chapter, various supporting results were obtained using nondimensional analysis. The most important result from this subsection, is that for different separation distances, the field characteristics are the same. This agrees with similar observations that Mason made theoretically and experimentally. This result further supports the theoretical model derived in this work, as that model also contained no separation dependent variables. Another important result from this analysis, was the very strong dependence of the depolarization factors on the capillary radius, something that was also noted by Mason, and seen in the theoretical results of this thesis.

The majority of the above contributions are based on the observation that the fields at which corona discharges occur for electrospraying, is not the same for all liquids. As mentioned in the literature review, Buraev and Vereshchagin calculated 49 mN/m to be the maximum surface tension for their geometry, which ended up being quoted in subsequent papers to be the maximum for all geometries. Even though Cloupeau suggested the Rousse model to be used for calculating the corona thresholds, another important point he made was that even the corona thresholds for cylinders and wires are debated, meaning that for electrospraying geometries exact results cannot be expected.

Summary

The electrodynamics of arbitrary, point-to-plane electrospraying geometries, were investigated in this research both analytically and numerically. The main outcomes and outlook are summarised below:

Droplet dielectric theory Elementary dielectric electrostatics was used to describe the electrostatics of the inhomogeneous electric fields generated by point-to-plane electrospraying geometries. Conformal mappings were used to understand the qualitative behaviour of the liquid droplets found at these capillary tips, which were modelled using parabolic functions, that could be mapped into a linear geometry. The models obtained are simple and agree well with finite element analysis results.

Finite element analysis COMSOL Multiphysics was employed to study the dielectric electrostatics of point-to-plane electrospraying geometries by means of finite element analysis. These numerical results were used to derive a polarization model for such geometries, and was later also used as a verification method for the analytically derived models.

Dimensional analysis Numerical results were analysed by using dimensional analysis to derive a polarization model for electrospraying geometries. This model was used to determine the corona discharge thresholds for these geometries, and compared well when compared to experimental investigations of other researchers. Compared to the analytically derived model, these two models also agree well. Also, dimensional analysis was used to qualitatively motivate these analytical assumptions, which agreed with those made by Mason, both theoretically and experimentally.

Corona threshold model A corona discharge threshold model is proposed, using either the numerically, or the analytically derived models for the calculation of polarization fields. When compared with the experimental results of other researchers, both these two models have average relative percentage errors of 15% (assuming the experimental measurements to be correct). These are the first models proposed in the literature for the calculation of point-to-plane electrospraying corona thresholds.

Taylor-cone formation time A new method to determine the Taylor-cone formation times is proposed, which is primarily based on the research of Suvorov and Zubarev for liquid metals in external electric fields. Using this method, it was showed that it is possible to quantise the pulsed cone-jet fulcrum frequency, defined as the maximum cone-formation frequency, at which the generated droplets are not of a uniform nature any more (having applications in pattern generation using pulsed electrospraying).

Surface tension measurement A new method to determine surface tension using electrospray ionization is described theoretically. Unlike most other methods which are restricted to certain liquids, it is possible to use this proposed method with most liquids. The unique feature of this method is its ability to do measurements at arbitrary temperatures.

Outlook Vast amounts of follow-up research could be conducted, but the most important aspect, is that of calculating the corona discharge thresholds. The model proposed employs the Rousse model, which is an adaptation of Peek's Law, to determine the corona thresholds when considering the polarization effects. As it is known from the literature, the fields at which the actual corona onsets occur are much higher than those predicted by point-to-plane geometry solutions. A more accurate model to determine these thresholds, will vastly improve the currently proposed model.

Appendices

Appendix A | MATLAB Code

A.1 Dimensional analysis

```
% Clear the memory and load required data
clear; close all; load RData.mat;

Figure = figure;
Axes = axes('FontWeight','bold','FontSize',20,'XScale','log');
box(Axes,'on'); hold(Axes,'all');

AVolt = 1000; S1 = 102.4*10^-6; AverageNDim = 0;

for i=1:length(Radius)
    EField = RFields(:,i);
    Rad = Radius(i)*10^-6;
    S2 = Surface(i);
    S3 = Volume(i);
    E0 = EField(1);
    EF = EField(end);

    NDim3 = EField*Rad/AVolt;
    NDim4 = EField*S1/AVolt;
    NDim5 = EField.^2*S2/AVolt^2;
    NDim6 = EField.^3*S3/AVolt^3;
    NDim7 = E0./EField;
    NDim8 = EF./EField;
    NDim9 = NDim7.*NDim8;
    NDim10 = NDim8./NDim6;

    AverageNDim = AverageNDim + NDim10;
    plot(Perm,NDim10,'LineWidth',2);
end

AverageNDim = AverageNDim/length(Radius);
plot(Perm,AverageNDim,'LineWidth',3);

xlabel({'Relative permittivity'},'FontSize',24);
ylabel({'Nondimensional variable R\Pi_10'},'FontSize',24);
set(gca,'PlotBoxAspectRatio',[4 3 1]);
xlim([1 100]);
```

A.2 Conformal mappings (visualisation)

```
% Clear the memory and load required data
clear; close all;

% ------------------------------------------------------------
% Geometrical parametors
% ------------------------------------------------------------
Q = 5;                          % Main parametric bound
W = Q/2;                        % Liquid parametric bound
r = 100;                        % Capillary radius
k = 1.05;                       % Liquid thinkness
a = sqrt(r/2);                  % Hyperbolic coeffient (Main)
A = sqrt((k*r)/2);              % Hyperbolic coeffient (Liquid)
t = linspace(-Q,Q,10000);       % Main parametric range
T = linspace(-W,W,10000);       % Liquid parametric range
P = length(t)/2+1;              % Central parametric point
LT = 100;                       % Counter-electrode position

% ------------------------------------------------------------
% Generate original hyperbolas
% ------------------------------------------------------------
x = a^2-t.^2;    y = 2*a*t;       % Main hyperbola
xL = A^2-T.^2; yL = 2*A*T;        % Partial liquid hyperbola
XL = A^2-t.^2; YL = 2*A*t;        % Complete liquid hyperbola

% ------------------------------------------------------------
% Generate transformations
% ------------------------------------------------------------
w =    x + 1i*y;                % Main hyperbola
wL = xL + 1i*yL;                % Partial liquid hyperbola
WL = XL + 1i*YL;                % Complete liquid hyperbola

z  =  (w).^(1/2);  u = real(z);   v = imag(z);
zL = (wL).^(1/2); uL = real(zL); vL = imag(zL);
ZL = (WL).^(1/2); UL = real(ZL); VL = imag(ZL);

% ------------------------------------------------------------
% Generate original boundaries
% ------------------------------------------------------------
h = y(end);    l = x(end);

H = abs(v(1)); h0 = 1;
HFunc = @(h) sqrt(sqrt(h^2+LT^2))*sin(0.5*acos(LT/(sqrt(h^2+LT
    ^2))))-H;
hF = abs(fzero(HFunc,h0));
% hF = h;

xb0 = [LT;LT]; yb0 = [-h;h];
xb1 = [LT;LT]; yb1 = [-hF;hF];
xb2 = [l;l];   yb2 = [-hF;hF];
xb3 = [l;LT];  yb3 = [-hF;-hF];
```

```
xb4 = [l;LT];  yb4 = [hF;hF];

% ------------------------------------------------------------
% Generate boundary transformations
% ------------------------------------------------------------
wb0 = xb0 + 1i*yb0;
wb1 = xb1 + 1i*yb1;
wb2 = xb2 + 1i*yb2;
wb3 = xb3 + 1i*yb3;
wb4 = xb4 + 1i*yb4;

zb0 = (wb0).^(1/2); ub0 = real(zb0); vb0 = imag(zb0);
zb1 = (wb1).^(1/2); ub1 = real(zb1); vb1 = imag(zb1);
zb2 = (wb2).^(1/2); ub2 = real(zb2); vb2 = imag(zb2);
zb3 = (wb3).^(1/2); ub3 = real(zb3); vb3 = imag(zb3);
zb4 = (wb4).^(1/2); ub4 = real(zb4); vb4 = imag(zb4);

HDiff = ub2(1)-u(1);

ub2 = ub2 - HDiff;
ub3 = ub3 - HDiff;
ub4 = ub4 - HDiff;
ub1 = ub0;

DDiff = abs(vb4(1)-vb4(end))/vb4(1);
LDiff = ub1(1)-uL(P);

CXX  = [l;LT];            CYY = [0;0];
CUU = [ub2(1);ub1(end)]; CVV = [0;0];
CUX = [ub2(1);ub1(end)]; CVY = [v(1);vb1(1)];
CUT = [ub2(1);ub1(end)]; CVS = [v(end);vb1(end)];

% ------------------------------------------------------------
% Plot original geometry
% ------------------------------------------------------------
subplot1 = subplot(2,1,1,'XMinorTick','on','YMinorTick','on','
    FontWeight','bold','FontSize',16);
box(subplot1,'on'); grid(subplot1,'on'); hold(subplot1,'all');
xlim(subplot1,[22.5 102.5]); ylim(subplot1,[-130 130]);

% Plot boundaries
plot(xb1,yb1,'LineWidth',3,'Color','Blue');
plot(xb2,yb2,'LineWidth',3,'Color',[0 0.75 0.75]);
plot(xb3,yb3,'LineWidth',3,'Color',[1 0 0]);
plot(xb4,yb4,'LineWidth',3,'Color',[1 0 0]);
% plot(CXX,CYY,'LineWidth',2,'Color',[0 0 0]);

% Plot geometries
plot(x,y,'LineWidth',3,'Color',[0.75 0.75 0.0]);
plot(xL,yL,'LineWidth',3,'Color',[0.0 0.5 0.0]);
% plot(XL,YL,'LineWidth',3,'Color',[0.0 0.5 0.0],'LineStyle
    ','--');
```

```
100
101 plot(xL(P),yL(P),'MarkerEdgeColor',[0 0 0],'MarkerSize',10,'
        Marker','o','LineWidth',2,'LineStyle','none','
        MarkerFaceColor',[0.83 0.82 0.78]);
102 plot(xL(1),yL(1),'MarkerEdgeColor',[0 0 0],'MarkerSize',10,'
        Marker','square','LineWidth',2,'LineStyle','none','
        MarkerFaceColor',[0.83 0.82 0.78]);
103 plot(xL(end),yL(end),'MarkerEdgeColor',[0 0 0],'MarkerSize',10,
        'Marker','square','LineWidth',2,'LineStyle','none','
        MarkerFaceColor',[0.83 0.82 0.78]);
104
105 title('Original','FontWeight','bold','FontSize',24);
106 set(gca,'PlotBoxAspectRatio',[2*16 9 1])
107
108 % ------------------------------------------------------------
109 % Plot transformed geometry
110 % ------------------------------------------------------------
111 subplot2 = subplot(2,1,2,'XMinorTick','on','YMinorTick','on','
        FontWeight','bold','FontSize',16);
112 box(subplot2,'on'); grid(subplot2,'on'); hold(subplot2,'all');
113 xlim(subplot2,[6.9 11.3]); ylim(subplot2,[-8 8]);
114
115 % Plot boundaries
116 plot(ub1,vb1,'LineWidth',3,'Color','Blue');
117 plot(ub2,vb2,'LineWidth',3,'Color',[0 0.75 0.75]);
118 plot(ub3,vb3,'LineWidth',2,'Color',[1 0 0],'LineStyle','--');
119 plot(ub4,vb4,'LineWidth',2,'Color',[1 0 0],'LineStyle','--');
120 % plot(CUU,CVV,'LineWidth',2,'Color',[0 0 0]);
121
122 plot(CUX,CVY,'LineWidth',3,'Color',[1 0 0]);
123 plot(CUT,CVS,'LineWidth',3,'Color',[1 0 0]);
124
125 % Plot geometries
126 plot(u,v,'LineWidth',3,'Color',[0.75 0.75 0.0]);
127 plot(uL,vL,'LineWidth',3,'Color',[0.0 0.5 0.0]);
128 % plot(UL,VL,'Color',[0.0 0.5 0.0],'LineStyle','--');
129
130 % plot([uL(1);ub2(1)],[vL(1);vL(1)],'LineWidth',2,'Color',[0 0
        0]); plot([uL(1);ub2(1)],[vL(end);vL(end)],'LineWidth',2,'
        Color',[0 0 0]);
131 plot(uL(P),vL(P),'MarkerEdgeColor',[0 0 0],'MarkerSize',10,'
        Marker','o','LineWidth',2,'LineStyle','none','
        MarkerFaceColor',[0.83 0.82 0.78]);
132 plot(uL(1),vL(1),'MarkerEdgeColor',[0 0 0],'MarkerSize',10,'
        Marker','square','LineWidth',2,'LineStyle','none','
        MarkerFaceColor',[0.83 0.82 0.78]);
133 plot(uL(end),vL(end),'MarkerEdgeColor',[0 0 0],'MarkerSize',10,
        'Marker','square','LineWidth',2,'LineStyle','none','
        MarkerFaceColor',[0.83 0.82 0.78]);
134
135 title('Transformed','FontWeight','bold','FontSize',24);
136 set(gca,'PlotBoxAspectRatio',[2*16 9 1])
```

A.3 Conformal mappings (equation solution)

```
% Clear the memory and load required data
clear; close all;

% ------------------------------------------------------------
% Geometrical parametors
% ------------------------------------------------------------
Q = sqrt(2);                % Main parametric bound
RLen = 50;                  % Radius upper bounde
t = linspace(-Q,Q,10000);   % Main parametric range

Radius = zeros(1,RLen);     % Array of radii values
SEPDiff0 = zeros(1,RLen);   % Original geometry separations
SEPDiffS = zeros(1,RLen);   % Transformed geometry separations
SEPDiffD = zeros(1,RLen);   % Transformed geometry separations

for i=1:RLen*10
    r = i/10;               % Capillary radius
    Radius(i) = r;          % Capillary radius
    a = sqrt(r/2);          % Hyperbolic coeffient (Main)
    L = 10*a^2;             % Counter-electrode position

    x = a^2-t.^2;           % Hyperbolic x-component
    y = 2*a*t;              % Hyperbolic y-component

    w = x + 1i*y;           % Complex contruction
    z = sqrt(w);            % Conformal mapping

    u = real(z);            % Extract u-component
    v = imag(z);            % Extract v-component

    h = y(end);             % Vertical plane length (original)
    H = abs(v(1));          % Vertical plane length (
       transformed)
    l = x(end);             % Vertical plane position (original
       )

    h0 = 1;                 % Numerical solver starting point
    HFunc = @(h) sqrt(sqrt(L^2+h^2))*sin(0.5*acos(L/(sqrt(h^2+L
       ^2))))-H;
    hF = abs(fzero(HFunc,h0));

    % Coordinates of plane positions
    xb1 = [L;L]; yb1 = [-hF;hF];
    xb2 = [l;l]; yb2 = [-hF;hF];

    % Complex plane contructions
    wb1 = xb1 + 1i*yb1;
    wb2 = xb2 + 1i*yb2;

    % Conformal mappings and component extraxtion
```

```
    zb1 = sqrt(wb1); ub1 = real(zb1); vb1 = imag(zb1);
    zb2 = sqrt(wb2); ub2 = real(zb2); vb2 = imag(zb2);

    % Separation distance between original planes
    SEPDiff0(i) = ub1(1) - ub2(1);

    % Separation distance between translated planes
    SEPDiffS(i) = ub1(1) - u(1);
    SEPDiffD(i) = sqrt(L) - a;
end

Figure = figure;
Axes = axes('Parent',Figure,'XGrid','on','YGrid','on','
   FontWeight','bold','FontSize',16);
box(Axes,'on'); hold(Axes,'all');

plot(Radius,SEPDiff0,'LineWidth',3);
plot(Radius,SEPDiffS,'LineWidth',3);
plot(Radius,SEPDiffD,'LineWidth',3);
legend('Original plane position','Translated plane position','
   Approximation');

xlabel({'Needle radius [microns]'},'FontWeight','bold','
   FontSize',20);
ylabel({'Conformal length [microns]'},'FontWeight','bold','
   FontSize',20);
set(gca,'PlotBoxAspectRatio',[4 3 1])
```

A.4 Conformal mappings (equation solution)

```
% Clear the memory and load required data
clear; close all;

% ------------------------------------------------------------
% Geometrical parametors
% ------------------------------------------------------------
C = 1;                      % Hyperbolic coeffient scaling
Q = sqrt(2);                      % Main parametric bound
RLen = 91;
t = linspace(-Q,Q,10000);   % Main parametric range
r = 20;                   % Capillary radius
Separation = zeros(1,RLen);
SEPDiff0 = zeros(1,RLen);
SEPDiffS = zeros(1,RLen);
SEPDiffD = zeros(1,RLen);   % Transformed geometry separations

for i=1:RLen
    a = sqrt(r/2)*C;                  % Hyperbolic coeffient (
       Main)
```

```
19      LT = (10+i-1)*a^2;                          % Counter-electrode
            position
20      Separation(i) = (10+i-1);
21
22      x = a^2-t.^2;    y = 2*a*t;
23      w = x + 1i*y;
24
25      z  =  (w).^(1/2);  u = real(z);    v = imag(z);
26
27      h = y(end);
28      l = x(end);
29      H = abs(v(1));h0 = 1;
30      HFunc = @(h) sqrt(sqrt(h^2+LT^2))*sin(0.5*acos(LT/(sqrt(h
            ^2+LT^2))))-H;
31      hF = abs(fzero(HFunc,h0));
32
33      xb1 = [LT;LT]; yb1 = [-hF;hF];
34      xb2 = [l;l];   yb2 = [-hF;hF];
35
36      wb1 = xb1 + 1i*yb1;
37      wb2 = xb2 + 1i*yb2;
38
39      zb1 = (wb1).^(1/2); ub1 = real(zb1); vb1 = imag(zb1);
40      zb2 = (wb2).^(1/2); ub2 = real(zb2); vb2 = imag(zb2);
41
42      HDiff = ub2(1)-u(1);
43      ub5 = ub1 - HDiff;
44
45      SEPDiff0(i) = ub5(1)-u(1);
46      SEPDiffS(i) = ub1(1)-u(1);
47      SEPDiffD(i) = sqrt(LT)-a;
48  end
49
50  Figure = figure;
51  Axes = axes('Parent',Figure,'XGrid','on','YGrid','on','
        FontWeight','bold','FontSize',16);
52  box(Axes,'on'); hold(Axes,'all');
53
54  plot(Separation,SEPDiff0,'LineWidth',3);
55  plot(Separation,SEPDiffS,'LineWidth',3);
56  plot(Separation,SEPDiffD,'LineWidth',3);
57  legend('Original plane position','Translated plane position','
        Approximation');
58
59  xlabel({'Separation-radius ratio'},'FontWeight','bold','
        FontSize',20);
60  ylabel({'Conformal length [microns]'},'FontWeight','bold','
        FontSize',20);
61  set(gca,'PlotBoxAspectRatio',[4 3 1])
```

Appendix B | Supporting figures

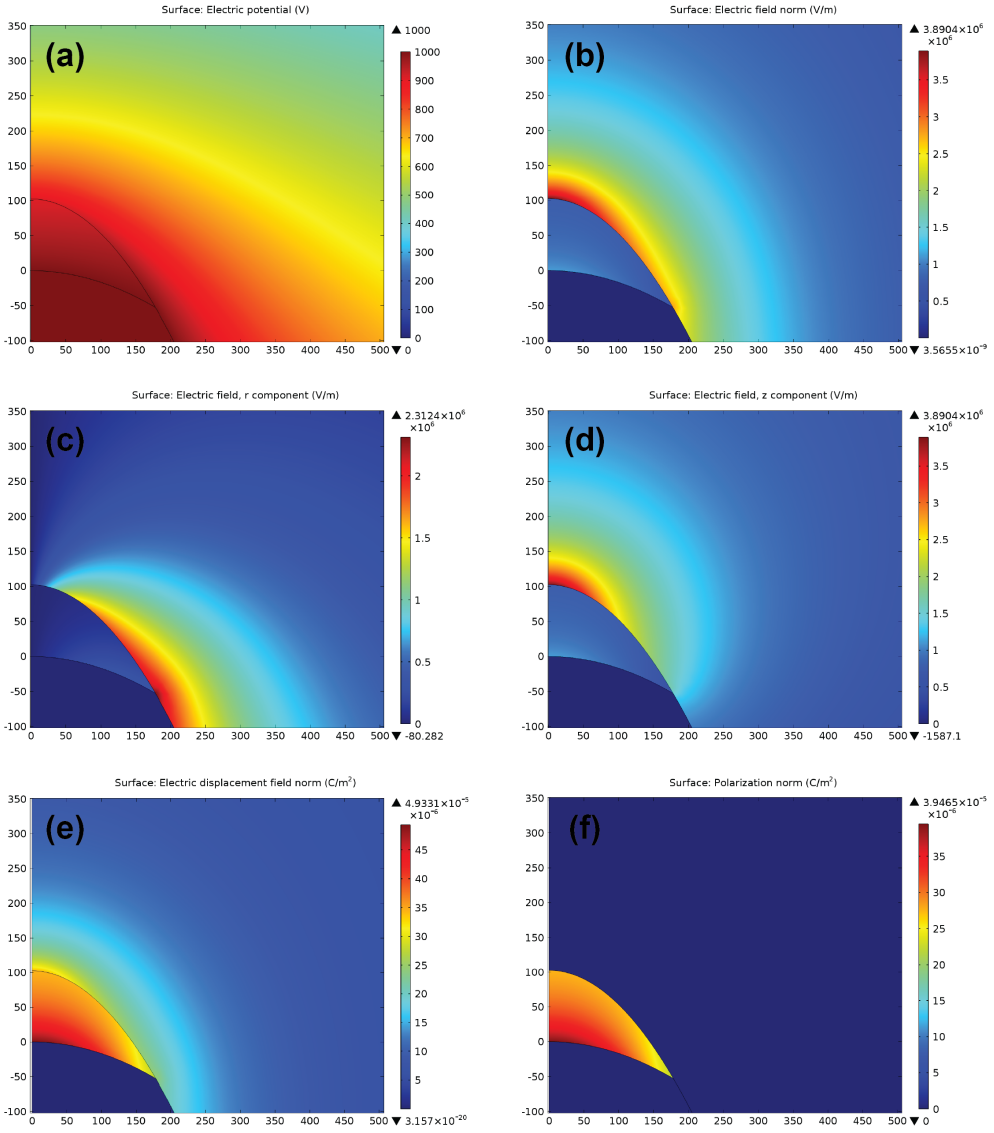

Figure B.1: Numerical solutions to an electrospraying geometry using COMSOL Multiphysics [60]. From left to right, top to bottom: the electric potential (a), field norm (b), electric field r-component (c), electric field z-component (d), displacement field (e), and polarization density (f), using an axisymmetric r-axis.

List of References

[1] Feynman, R.: There's Plenty of Room at the Bottom. *Engineering and Science*, vol. 23, no. 1, pp. 22–36, 1960.

[2] Cloupeau, M. and Prunet-Foch, B.: Electrohydrodynamic spraying functioning modes: a critical review. *Journal of Aerosol Science*, vol. 25, no. 6, pp. 1021–1036, 1994.

[3] Wilm, M.S. and Mann, M.: Electrospray and Taylor-cone theory, Dole's beam of macromolecules at last? *International Journal of Mass Spectrometry and Ion Processes*, vol. 136, no. 2, pp. 167–180, 1994.

[4] De la Mora, J.N.: The Fluid Dynamics of Taylor Cones. *Annual Review of Fluid Mechanics*, vol. 39, no. 1, pp. 217–243, 2007.

[5] Teo, W.E. and Ramakrishna, S.: A review on electrospinning design and nanofibre assemblies. *Nanotechnology*, vol. 17, no. 14, pp. 89–106, 2006.

[6] Jaworek, A. and Sobczyk, A.: Electrospraying route to nanotechnology: An overview. *Journal of Electrostatics*, vol. 66, no. 3, pp. 197–219, 2008.

[7] Jaworek, A.: Micro- and nanoparticle production by electrospraying. *Powder Technology*, vol. 176, no. 1, pp. 18–35, 2007.

[8] Pantano, C., Ganan-Calvo, A. and Barrero, A.: Zeroth-order, electrohydrostatic solution for electrospraying in cone-jet mode. *Journal of Aerosol Science*, vol. 25, no. 6, pp. 1065–1077, 1994.

[9] Meesters, G., Vercoulen, P., Marijnissen, J. and Scarlett, B.: Generation of micron-sized droplets from the Taylor cone. *Journal of Aerosol Science*, vol. 23, no. 1, pp. 37–49, 1992.

[10] Smith, D.: The Electrohydrodynamic Atomization of Liquids. *IEEE Transactions on Industry Applications*, vol. 22, no. 3, pp. 527–535, 1986.

[11] Jaworek, A. and Krupa, A.: Jet and drops formation in electrohydrodynamic spraying of liquids. A systematic approach. *Experiments in Fluids*, vol. 27, no. 1, pp. 43–52, 1999.

[12] De la Mora, J.N. and Loscertales, I.G.: The current emitted by highly conducting Taylor cones. *Journal of Fluid Mechanics*, vol. 260, no. 1, pp. 155–184, 1994.

[13] Gamero-Castano, M. and Hruby, V.: Electrospray as a source of nanoparticles for efficient colloid thrusters. *Journal of Propulsion and Power*, vol. 17, no. 5, pp. 977–987, 2001.

[14] Martínez-Sánchez, M.: Aeronautics and astronautics - 16.522 space propulsion. *MIT OpenCourseWare*, vol. 1, no. 23, pp. 1–36, 2004.

[15] Velásquez-García, L.F.: *The Design, Fabrication and Testing of Microfabricated Linear and Planar Colloid Thruster Arrays*. Ph.D. thesis, Department of Aeronautics and Astronautics, Massachusetts Institute of Technology, Cambridge, United States, 2004.

[16] Lozano, P. and Martìnez-Sànchez, M.: Ionic liquid ion sources: suppression of electrochemical reactions using voltage alternation. *Journal of Colloid and Interface Science*, vol. 280, no. 1, pp. 149–154, 2004.

[17] Lozano, P. and Martìnez-Sànchez, M.: Ionic liquid ion sources: characterization of externally wetted emitters. *Journal of Colloid and Interface Science*, vol. 282, no. 2, pp. 415–421, 2005.

[18] Regele, J., Papac, M., Rickard, M. and Dunn-Rankin, D.: Effects of capillary spacing on EHD spraying from an array of cone jets. *Journal of Aerosol Science*, vol. 33, no. 11, pp. 1471–1476, 2002.

[19] Zimlich, W.e.a.: The Development of a Novel Electrohydrodynamic Pulmonary Drug Delivery Device. *Respiratory Drug Delivery VII*, vol. 1, no. 1, pp. 241–246, 2000.

[20] Chen, D., Pui, D. and Kaufman, S.L.: Electrospraying of conducting liquids for monodisperse aerosol generation in the 4 nm to 1.8 um diameter range. *Journal of Aerosol Science*, vol. 26, no. 6, pp. 963–977, 1995.

[21] Lenggoro, I., Okuyama, K., de la Mora, J. and Tohge, N.: Preparation of ZnS nanoparticles by electrospray pyrolysis. *Journal of Aerosol Science*, vol. 31, no. 1, pp. 121–136, 2000.

[22] Lohmann, M., Beyer, H. and Schmidt-Ott, A.: Size and charge distribution of liquid metal electrospray generated particles. *Journal of Aerosol Science*, vol. 28, no. S1, pp. 349–350, 1997.

[23] Dorey, R. and Whatmore, R.: Electroceramic Thick Film Fabrication for MEMS. *Journal of Electroceramics*, vol. 12, no. 1, pp. 19–32, 2004.

[24] Buraev, T.K. and Vereshchagin, I.: Physical processes during electrostatic atomisation of liquids. *Fluid Mechanics–Soviet Research*, vol. 1, no. 2, pp. 56–66, 1972.

[25] Joffre, G. and Cloupeau, M.: Characteristic forms of electrified menisci emitting charges. *Journal of Electrostatics*, vol. 18, no. 2, pp. 147–161, 1986.

[26] Hayati, I., Bailey, A. and Tadros, T.: Investigations into the mechanisms of electrohydrodynamic spraying of liquids: I. Effect of electric field and the environment on pendant drops. *Journal of Colloid and Interface Science*, vol. 117, no. 1, pp. 205–221, 1987.

[27] Cloupeau, M.: Recipes for use of EHD spraying in cone-jet mode and notes on corona discharge effects. *Journal of Aerosol Science*, vol. 25, no. 6, pp. 1143–1157, 1994.

[28] Jaworek, A. and Krupa, A.: Studies of the corona discharge in ehd spraying. *Journal of Electrostatics*, vol. 40, no. 1, pp. 173–178, 1997.

[29] Park, H., Kim, K. and Kim, S.: Effects of a guard plate on the characteristics of an electrospray in the cone-jet mode. *Journal of Aerosol Science*, vol. 35, no. 11, pp. 1295–1312, 2004.

[30] Borra, J., Ehouarn, P. and Boulaud, D.: Electrohydrodynamic atomisation of water stabilised by glow discharge–operating range and droplet properties. *Journal of Aerosol Science*, vol. 35, no. 11, pp. 1313–1332, 2004.

[31] Jaworek, A., Czech, T., Rajch, E. and Lackowski, M.: Spectroscopic studies of electric discharges in electrospraying. *Journal of Electrostatics*, vol. 63, no. 6, pp. 635–641, 2005.

[32] De la Mora, J. and Gomez, A.: Remarks on the paper "Generation of micron-sized droplets from the Taylor cone". *Journal of Aerosol Science*, vol. 24, no. 5, pp. 691–695, 1993.

[33] Peek, F.: *Dielectric Phenomena in High Voltage Engineering.* Watchmaker Publishing, Seaside, 1929.

[34] Rousse, J.: *Emission par Effet Couronne aux Hautes Temperatures et Pressions (Generalisation de la Loi Paschen).* Ph.D. thesis, Universite de Paris, Paris, France, 1947.

[35] Razevig, D.: *Elektrichestvo*, vol. 6, no. 1, 1968.

[36] Lòpez-Herrera, J., Barrero, A., Boucard, A., Loscertales, I.G. and Màrquez, M.: An experimental study of the electrospraying of water in air at atmospheric pressure. *Journal of the American Society for Mass Spectrometry*, vol. 15, no. 2, pp. 253–259, 2004.

[37] Hoburg, J. and Melcher, J.: Current-driven, corona-terminated water jets as sources of charged droplets and audible noise. *IEEE Transactions on Power Apparatus and Systems*, vol. 94, no. 1, pp. 128–136, 1975.

[38] Tang, K. and Gomez, A.: Generation of Monodisperse Water Droplets from Electrosprays in a Corona-Assisted Cone-Jet Mode. *Journal of Colloid and Interface Science*, vol. 175, no. 2, pp. 326–332, 1995.

[39] Meesters, G., Vercoulen, P., Marijnissen, J. and Scarlett, B.: A (sub)micron aerosol generator, using a high electric field. *Journal of Aerosol Science*, vol. 22, no. S1, pp. 11–14, 1991.

[40] Borra, J., Tombette, Y. and Ehouarn, P.: Influence of electric field profile and polarity on the mode of ehda related to electric discharge regimes. *Journal of Aerosol Science*, vol. 30, no. 7, pp. 913–925, 1999.

[41] Hirsh, M. and Oskam, H.: *Gaseous Electronics: Electrical Discharges*. Academic Press, Waltham, Massachusetts, 1978.

[42] Loeb, L.: *Electrical Coronas: Their Basic Physical Mechanisms*. University of California Press, Berkeley, 1965.

[43] Fridman, A., Chirokov, A. and Gutsol, A.: Non-thermal atmospheric pressure discharges. *Journal of Physics D: Applied Physics*, vol. 38, no. 1, pp. R1–R24, 2005.

[44] Bandel, H.: Point-to-Plane Corona in Dry Air. *Physical Review*, vol. 84, no. 1, pp. 92–99, 1951.

[45] Raether, H.: Zum Aufbau von Gasentladungen. *Naturwissenschaften*, vol. 28, no. 47, pp. 749–750, 1940.

[46] Gary, C., Hutzler, B. and Schmidt, J.: Peeks Law generalisation: Application to various field configurations. *IEEE Summer Meeting (Paper C)*, 1972.

[47] Llewellyn-Jones, F. and Williams, G.C.: The Electrical Breakdown of Gases in Non-Uniform Fields at Low Pressure. *Proceedings of the Physical Society (Section B)*, vol. 66, no. 5, pp. 345–361, 1953.

[48] Kip, A.: Positive-Point-to-Plane Discharge in Air at Atmospheric Pressure. *Physical Review*, vol. 54, no. 2, pp. 139–146, 1938.

[49] Mason, J.: The Deterioration and Breakdown of Dielectrics Resulting from Internal Discharges. *Proceedings of the IEE – Part I*, vol. 98, no. 109, pp. 44–59, 1951.

[50] Mason, J.: Breakdown of Insulation by Discharges. *Proceedings of the IEE – Part IIA*, vol. 100, no. 3, pp. 149–158, 1953.

[51] Mason, J.: Breakdown of Solid Dielectrics in Divergent Fields. *Proceedings of the IEE – Part C*, vol. 102, no. 2, pp. 254–263, 1955.

[52] Bamji, S.S., Bulinski, A.T. and Prasad, K.M.: Electric Field Calculations with the Boundary Element Method. *IEEE Transactions on Electrical Insulation*, vol. 28, no. 3, pp. 420–424, 1993.

[53] Chen, G. and Davies, A.: Electric stress computation–a needle-plane electrode system with space charge effects. *International Journal for Computation and Mathematics in Electrical and Electronic Engineering*, vol. 15, no. 1, pp. 40–56, 1996.

[54] Nelson, J. and Fothergill, J.C.: Internal Charge Behaviour of Nanocomposites. *Nanotechnology*, vol. 15, no. 5, pp. 586–595, 2004.

[55] Waters: *Micromass Quattro Premier NanoFlow ElectroSpray*. Waters, Milford, M.A., 2004.

[56] Purcell, E.M.: *Electricity and Magnetism*. 2nd edn. McGraw-Hill Science, New York, 1984.

[57] Kittel, C.: *Introduction to Solid State Physics*. 8th edn. Wiley, New Jersey, 2004.

[58] Osborn, J.A.: Demagnetizing Factors of the General Ellipsoid. *Physical Review*, vol. 67, no. 11, pp. 351–357, 1945.

[59] Jackson, J.: *Classical Electrodynamics*. 3rd edn. Wiley, New Jersey, 1999.

[60] COMSOL Multiphysics [Online]: Available at: `http://www.comsol.com`, 2013.

[61] Zill, D. and Wright, W.: *Advanced Engineering Mathematics*. 4th edn. Jones and Bartlett Publishers, Burlington, 2009.

[62] Kim, J. and Oh, H.: Electrohydrodynamic drop-on-demand patterning in pulsed cone-jet mode at various frequencies. *Journal of Aerosol Science*, vol. 39, no. 2, pp. 819–825, 2008.

[63] Pieterse, C.L.: Comments on: "Electrohydrodynamic drop-on-demand patterning in pulsed cone-jet mode at various frequencies" by Joonghyuk Kim, Hyuncheol Oh and Sang Soo Kim. *Journal of Aerosol Science*, vol. 57, no. 0, pp. 199–202, 2013.

[64] Suvorov, V. and Zubarev, N.: Formation of the Taylor cone on the surface of liquid metal in the presence of an electric field. *Journal of Physics D: Applied Physics*, vol. 37, no. 2, pp. 289–297, 2004.

[65] Ramos, A. and Castellanos, A.: Equilibrium shapes and bifurcation of captive dielectric drops subjected to electric fields. *Journal of Electrostatics*, vol. 33, no. 1, pp. 61–86, 1994.

[66] Stone, H. A., L.J.R. and Brenner, M.P.: Drops with conical ends in electric and magnetic fields. *Proceedings of the Royal Society A*, vol. 44, no. 1981, pp. 329–347, 1999.

[67] Lee, B., R.P. and Chan, E.: New drop weight analysis for surface tension determination of liquids. *Colloids and Surfaces A*, vol. 332, no. 2, pp. 112–120, 2009.

[68] Fainerman, V., Makievski, A. and Miller, R.: The measurement of dynamic surface tensions of highly viscous liquids by the maximum bubble pressure method. *Colloids and Surfaces A*, vol. 75, no. 1, pp. 229–235, 1993.

[69] Watanabe, W.e.: Why inhaling salt water changes what we exhale. *Journal of Colloid and Interface Science*, vol. 307, no. 1, pp. 71–78, 2007.

[70] Pieterse, C.L.: Electrohydrodynamic Atomization Limitations at Atmospheric Conditions Due to Corona Discharge. In: *IEEE Eurocon*, pp. 1897–1903. Zagreb: University of Zagreb, 2013.

[71] Iseg Spezialelektronik GmbH (NHS High Voltage) [Online]: Available at: `http://www.iseg-hv.com/en/products/product-details/product/1624/`, 2014.

[72] Physik Instrumente GmbH. (N-310 NEXACT OEM Miniature Linear Motor/Actuato) [Online]: Available at: `http://www.physikinstrumente.com/en/pdf/N310_Datasheet.pdf`, 2014.

[73] Jasper, J.J.: The Surface Tension of Pure Liquid Compounds. *Journal of Physical and Chemical Reference Data*, vol. 1, no. 4, p. 841, 1972.

[74] Lide, D.: *CRC Handbook of Chemistry and Physics*. 90th edn. CRC Press, Cleveland, 2009.

[75] Celanese (Acetic Acid) [Online]: Available at: `http://www.chemvip.com/proddesc-aceticacid-glacial-en.pdf`, 2014.

[76] Dow (Acetone) [Online]: Available at: `http://www.dow.com/webapps/lit/litorder.asp?filepath=productsafety/pdfs/noreg/115-00648.pdf`, 2014.

[77] Rocha, M. and Simões, J.: A simple impedance method for determining ethanol and regular gasoline mixtures mass contents. *Fuel*, vol. 84, no. 4, pp. 447–452, 2005.

[78] Zienkiewicz, O.C. & Taylor, R.: *The Finite Element Method*. 5th edn. Elsevier Butterworth-Heinemann, Burlington, 2000.

[79] Akin, J.E.: *Finite Element Analysis with Error Estimators*. Elsevier Butterworth-Heinemann, Burlington, 2005.

[80] Rao, S.: *The Finite Element Method in Engineering*. 4th edn. Elsevier Butterworth-Heinemann, Burlington, 2005.

[81] Zienkiewicz, O., Arlett, P. and Bahrani, A.: Solution of three dimensional field problems by finite element method. *The Engineer*, 1967.

[82] Schnepf, A. and Leitner, D.: FEM simulation of below ground processes on a 3D root system geometry using Distmesh and COMSOL Multiphysics. In: *Conference on Scientific Computing*, vol. 18, pp. 321–330. 2009.

[83] Price, J.F.: Dimensional analysis of models and data sets. *American Journal of Physics*, vol. 71, no. 5, pp. 437–447, 2003.

[84] Van Groesen, E. and Molenaar, J.: *Continuum Modeling in the Physical Sciences*. Society for Industrial and Applied Mathematics, Philadelphia, 2007.

[85] Taylor, G.: The Formation of a Blast Wave by a Very Intense Explosion. II. The Atomic Explosion of 1945. In: *Proceedings of the Royal Society A*, vol. 201, pp. 175–186. 1950.

[86] Taylor, G.: Disintegration of Water Droplets in an Electric Field. In: *Proceedings of the Royal Society A*, vol. 280, pp. 383–397. 1964.

[87] Workman, J.: *The Handbook of Organic Compounds*. 1st edn. Academic Press, Waltham, Massachusetts, 2001.

[88] Yamada, M., Fukusako, S., Kawanami, T., Sawada, I. and Horibe, A.: Surface tension of aqueous binary solutions. *International Journal of Thermophysics*, vol. 18, no. 6, pp. 1483–1493, 1997.

[89] Chetwani, N., Cassou, C.A., Go, D.B. and Chang, H.: High-frequency AC electrospray ionization source for mass spectrometry of biomolecules. *Journal of the American Society for Mass Spectrometry*, vol. 21, no. 11, pp. 1852–1856, 2010.

[90] Caldwell, A., Kollar, D. and Kröninger, K.: BAT – The Bayesian Analysis Toolkit. *Computer Physics Communications*, vol. 180, no. 11, pp. 2197–2209, 2009.